

STRUCTURAL AND MAGNETIC STUDIES OF IRON(III)
SAL-R-EN SPIN CROSSOVER COMPLEXES



A Thesis Submitted in Partial Fulfillment of the Requirements for the
Degree of Master of Science in Chemistry
Suranaree University of Technology
Academic Year 2024

การศึกษาโครงสร้าง และสมบัติทางแม่เหล็กของสารประกอบเชิงซ้อน
เหล็ก(III) ซาล-อาร์-เอน สปีนโครสโอเวอร์



วิทยานิพนธ์นี้เป็นส่วนหนึ่งของการศึกษาตามหลักสูตรปริญญาวิทยาศาสตรมหาบัณฑิต

สาขาวิชาเคมี

มหาวิทยาลัยเทคโนโลยีสุรนารี

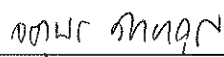
ปีการศึกษา 2567

STRUCTURAL AND MAGNETIC STUDIES OF IRON(III)

SAL-R-EN SPIN CROSSOVER COMPLEXES

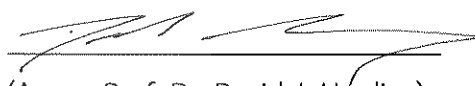
Suranaree University of Technology has approved this thesis submitted in partial fulfillment of the requirements for a Master's degree.

Thesis Examining Committee



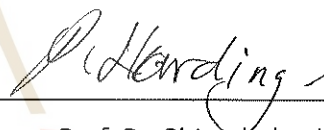
(Prof. Dr. Jatuporn Wittayakun)

Chairperson



(Assoc. Prof. Dr. David J. Harding)

Member (Thesis Advisor)



(Assoc. Prof. Dr. Phimpaka Harding)

Member (Thesis Co-Advisor)



(Assoc. Prof. Dr. Theeranun Siritanon)

Member




(Assoc. Prof. Dr. Thanthapat Bunchuay)

Member



(Assoc. Prof. Dr. Yupaporn Ruksakulpiwat)

Acting Vice-Rector for Academic Affairs
and Quality Assurance



(Prof. Dr. Santi Maensiri)

Dean of the Institute of Science

นาเดีย นาถปุตริ : การศึกษาโครงสร้าง และสมบัติทางแม่เหล็กของสารประกอบเชิงซ้อน
เหล็ก(III) ซาล-อาร์-เอน สปินคrossover (STRUCTURAL AND MAGNETIC STUDIES
OF IRON(III) SAL-R-EN SPIN CROSSOVER COMPLEXES).

อาจารย์ที่ปรึกษา : รองศาสตราจารย์ ดร.เดวิด เจมส์ ฮาร์ดิง, 95 หน้า.

คำสำคัญ : สปินคrossover สารประกอบเชิงซ้อนเหล็ก(III) การเปลี่ยนแปลงสมมาตร การเลี้ยวเบน
รังสีเอกซ์แบบผลึกเดี่ยว การวัดสนามแม่เหล็ก

สารประกอบประเภทสปินคrossover จัดอยู่ในกลุ่มวัสดุเชิงโมเลกุลที่สามารถเปลี่ยนสถานะ
ได้ โดยกระบวนการเปลี่ยนสถานะสปินของอิเล็กตรอนระหว่างสปินต่ำและสปินสูง ในงานวิจัยเรื่องนี้
มุ่งศึกษาสมบัติทางแม่เหล็กและโครงสร้างของสารประกอบเชิงซ้อนเหล็กที่มีหมู่แทนที่ของลิแกนด์
และไอออนลบที่แตกต่างกัน $[\text{Fe}(\text{salRen-5-OMe})_2]\text{A}$ (R = benzyl, A = Cl^- 1, Br^- 2, I^- 3, NO_3^- 4,
 ClO_4^- 5; R = Propyl, A = Cl^- 6, Br^- 7, I^- 8, NO_3^- 9, ClO_4^- 10) สารประกอบเหล่านี้ถูกสังเคราะห์
และพิสูจน์เอกลักษณ์ด้วยเทคนิคอินฟราเรด ยูวีวิสิเบิล นิวเคลียร์แมกเนติกเรโซแนนซ์สเปกโทรสโกปี
การวิเคราะห์ธาตุ แมสสเปกโตรเมตรี การเลี้ยวเบนรังสีเอกซ์แบบผง การเลี้ยวเบนรังสีเอกซ์แบบผลึก
เดี่ยว ไซคลิกโวลแทมเมตรี และการวัดสนามแม่เหล็ก สเปกตรัมยูวีวิสิเบิลของสารประกอบเชิงซ้อน
ทั้งหมดแสดงการดูดกลืนความยาวคลื่นที่แตรอนลิชันแบบ LMCT จำนวน 2 สัญญาณ ซึ่งบ่งถึงการเกิด
สปีซีของทั้งสปินต่ำและสปินสูงในสารละลายที่อุณหภูมิห้องจากการวิเคราะห์โครงสร้างผลึกของ
สารประกอบกลุ่ม salBzen ด้วยเทคนิคการเลี้ยวเบนรังสีเอกซ์แบบผลึกเดี่ยวพบว่าสารประกอบ
เหล่านี้ตกผลึกในโครงสร้างโมโนคลินิก ($\text{P2}_1/\text{n}$ หรือ $\text{P2}_1/\text{c}$ สำหรับ 1 2 4 5) หรือ เตตระโกนอล
(P4_32_12 สำหรับ 3) ที่อุณหภูมิห้องการศึกษาทางโครงสร้างของสารประกอบ 1 2 และ 4 แสดงสมบัติ
แบบสปินสูง ในขณะที่ 3 และ 5 แสดงสมบัติสปินแบบต่ำ นอกจากนี้สารประกอบ 1 ยังแสดง
พฤติกรรมของการเปลี่ยนแปลงสมมาตร ซึ่งเกิดขึ้นแยกจากกระบวนการเกิดสปินคrossover อันตร
กิริยาระหว่างโมเลกุล เช่น $\text{C-H}\cdots\pi$, $\text{C-H}\cdots\text{O}$, $\text{N-H}\cdots\text{O}$, $\text{C-H}\cdots\text{anion}$ และ $\text{N-H}\cdots\text{anion}$ ได้เชื่อมต่อกับ
โครงสร้างเข้าด้วยกันจนเกิดเป็นโครงสร้างซูปราโมเลกุลสามมิติ จากการศึกษาสนามแม่เหล็กพบว่า 1
และ 2 ยังคงอยู่ในสถานะสปินสูงจนถึงอุณหภูมิ 10 เคลวิน ขณะที่ 5 มีการเปลี่ยนสถานะสปินคrossover
โอเวอร์อย่างรวดเร็วพร้อมเกิดฮิสเทอรีซิสเล็กน้อย (6 เคลวิน) โดยเกี่ยวข้องกับการเปลี่ยนสถานะของ
เหล็ก 20% ส่วน 3 และ 4 มีการเปลี่ยนสถานะสปินคrossover แบบค่อยเป็นค่อยไปที่อุณหภูมิสูง
กว่า 350 เคลวิน สำหรับสารประกอบกลุ่ม salPren (6-10) แม้ว่าจะไม่สามารถตกผลึกได้ แต่
การศึกษาด้านแม่เหล็กแสดงให้เห็นการเปลี่ยนสถานะสปินคrossover ที่ค่อยเป็นค่อยไปและไม่
สมบูรณ์ การศึกษาทางเคมีไฟฟ้าของสารประกอบ 1-5 และ 6-10 แสดงให้เห็นว่าโครงสร้างลิแกนด์
และแอนไอออนมีอิทธิพลอย่างมากต่อพฤติกรรมการเกิดปฏิกิริยารีดอกซ์

สารประกอบกลุ่ม salBzen แสดงความแปรปรวนของศักย์ไฟฟ้ารีดอกซ์มากกว่า เนื่องจากมีปฏิสัมพันธ์กับแอนไอออนที่แข็งแรงภายในโครงสร้างที่แข็งแรง ในขณะที่สารประกอบกลุ่ม salPren แสดงศักย์ไฟฟ้าที่คงที่มากกว่า ซึ่งบ่งชี้ถึงความคล่องตัวของแอนไอออนที่สูงขึ้น นอกจากนี้ สารประกอบ salPren ยังแสดงศักย์ไฟฟ้าในการเกิดออกซิเดชันที่สูงกว่าเล็กน้อยและการถ่ายโอนอิเล็กตรอนที่รวดเร็วกว่า แสดงถึงบทบาทของความยืดหยุ่นของลิแกนด์และการประสานงานของแอนไอออนในการควบคุมสมบัติการเกิดปฏิกิริยารีดอกซ์ของสารประกอบเหล็ก (III) ชนิดซีฟฟ์เบส

ผลการวิจัยนี้ชี้ให้เห็นว่าหมู่แทนที่ของลิแกนด์และไอออนลบที่แตกต่างกัน มีบทบาทสำคัญในการปรับเปลี่ยนคุณสมบัติแม่เหล็ก พร้อมทั้งแสดงให้เห็นว่าการควบคุมความสมมาตรและกระบวนการเกิดสปินครอสโอเวอร์ สามารถแยกออกจากกันได้ งานวิจัยนี้เสนอข้อมูลเชิงลึกที่สำคัญสำหรับการออกแบบวัสดุฟังก์ชันขั้นสูงในด้านสปินทรอนิกส์เชิงโมเลกุลและวิทยาศาสตร์วัสดุ



สาขาวิชาเคมี
ปีการศึกษา 2567

ลายมือชื่อนักศึกษา Nardira Natputree

ลายมือชื่ออาจารย์ที่ปรึกษา [Signature]

ลายมือชื่ออาจารย์ที่ปรึกษาร่วม [Signature]

NADIA NATPUTREE : STRUCTURAL AND MAGNETIC STUDIES OF IRON(III) SAL-R-
EN SPIN CROSSOVER COMPLEXES. THESIS ADVISOR : ASSOC. PROF. DAVID J.
HARDING, Ph.D. 95 PP.

Keywords : Fe(III) complexes; Spin crossover; symmetry breaking; X-Ray diffraction;
SQUID magnetometry

Spin crossover (SCO) compounds are a unique class of molecular switchable materials. SCO involves switching between a high spin (HS) and a low spin (LS) state. This study reports a new series of Fe(III) complexes, $[\text{Fe}(\text{salRen-5-OMe})_2]\text{A}$, where the effects of substituent groups on a tridentate ligand platform and the counterions (R = benzyl, A = Cl^- **1**, Br^- **2**, I^- **3**, NO_3^- **4**, ClO_4^- **5**; R = propyl, A = Cl^- **6**, Br^- **7**, I^- **8**, NO_3^- **9**, ClO_4^- **10**) are investigated. The complexes were synthesized and characterized using IR, UV-Vis, and NMR spectroscopy, elemental analysis, mass spectrometry, powder X-ray diffraction, X-ray crystallography, cyclic voltammetry, and SQUID magnetometry. Crystal structures of the salBen series, determined via X-ray diffraction, show that the complexes crystallize in monoclinic ($\text{P2}_1/\text{n}$ or $\text{P2}_1/\text{c}$ for **1**, **2**, **4**, **5**) or tetragonal (P4_32_12 for **3**) phases. The X-ray crystal structures at room temperature reveal HS Fe(III) centers in **1**, **2** and **5**, and LS Fe(III) centers in **3** and **4**. Notably, complex **1** demonstrates symmetry breaking, decoupling the phenomenon from spin crossover. A variety of intermolecular interactions, including $\text{C-H}\cdots\pi$, $\text{C-H}\cdots\text{O}$, $\text{N-H}\cdots\text{O}$, $\text{C-H}\cdots\text{anion}$, and $\text{N-H}\cdots\text{anion}$, are responsible for linking the cations and forming a 3D supramolecular network. SQUID magnetometry revealed that **1** and **2** remain HS down to 10 K, while **5** undergoes abrupt spin crossover with slight hysteresis (6 K), involving 20% Fe switching. In contrast, **3** and **4** display gradual SCO above 350 K. The salPren series **6-10** exhibited gradual, incomplete SCO, although recrystallization was unsuccessful. The electrochemical studies of complexes **1-5** and **6-10** reveal that ligand structure and counteranions significantly influence redox behavior. The salBen complexes show greater redox potential variation due to strong anion interactions within a rigid binding pocket, while the salPren complexes exhibit more consistent potentials, indicating higher anion mobility. Additionally, salPren complexes display slightly higher oxidation

potentials and faster electron transfer, highlighting the role of ligand flexibility and anion coordination in tuning the redox properties of Fe(III) Schiff base complexes.

These findings highlight the crucial role of counterions and ligand platform in tuning magnetic properties and demonstrate independent control of symmetry breaking and spin crossover. This work provides valuable insights for designing advanced functional materials for molecular spintronics and materials science.



School of Chemistry
Academic Year 2024

Student's Signature Nadira Natputree

Advisor's Signature [Signature]

ACKNOWLEDGEMENTS

Completing this thesis has been an incredible milestone in my master's degree journey. This achievement would not have been possible without the guidance and support of several individuals who, in one way or another, contributed significantly to the preparation and completion of this study. It is my sincere pleasure to extend my gratitude to those who made this work possible.

My deepest gratitude goes to my thesis advisor, Assoc. Prof. Dr. David J. Harding, and co-advisor, Assoc. Prof. Dr. Phimpaka Harding, for their unwavering guidance, mentorship, and encouragement throughout my research journey. Their expertise and support have been invaluable in shaping this work and fostering my growth as a researcher.

My sincere thanks also go to Dr. Guillaume Chastanet for giving me the opportunity to join his group as an intern for six months. My time at the Institute of Condensed Matter Chemistry of Bordeaux (ICMCB), France, was both enriching and enjoyable. I especially appreciated working closely with Dr. Elen Duverger-Nédellec and the other staff at ICMCB, whose guidance and collaboration greatly contributed to my development and the progress of this research.

I am truly thankful to all Harding group members, the Molecular Magnetic Materials (M³) lab, and the Institute of Science, School of Chemistry at Suranaree University, for their insightful suggestions and for providing access to various instruments that greatly facilitated this research.

I am deeply grateful to the Development and Promotion of Science and Technology Talents Project (DPST) scholarship for granting me the opportunity to conduct this research.

Lastly, my heartfelt gratitude goes to my family for their unyielding support and belief in me. Their unconditional love has been the foundation of my strength and the key to achieving this milestone.

Nadia Natputree

CONTENTS

	Page
ABSTRACT IN THAI	I
ABSTRACT IN ENGLISH	III
ACKNOWLEDGEMENTS.....	V
CONTENTS	VI
LIST OF TABLES.....	IX
LIST OF FIGURES	X
LIST OF ABBREVIATIONS.....	XIII
 CHAPTER	
I INTRODUCTION.....	1
1.1 Background.....	1
1.2 Research objectives	2
1.3 Scope and limitation of the study	2
1.4 References.....	3
II LITERATURE REVIEW	4
2.1 The spin crossover phenomenon.....	4
2.2 Measurement techniques.....	5
2.2.1 X-ray crystallography	5
2.2.1.1 Metal-ligand bond length.....	5
2.2.1.2 Distortion in octahedral coordination complexes.....	5
2.2.2 SQUID magnetometry	7
2.3 Supramolecular Interactions.....	8
2.3.1 Hydrogen bonding	8
2.3.2 Halogen bonding.....	9
2.3.3 π - π and C-H $\cdots\pi$ interaction.....	10
2.4 Spin crossover iron(III)-ethylsalicylaldiminate complexes	12

CONTENTS (Continued)

		Page
	2.4.1 SalRen ligands.....	12
	2.4.2 Anion effects.....	13
	2.4.3 Solvent effects	17
2.5	References.....	19
III	MATERIALS AND METHODS.....	24
3.1	Experimental.....	24
	3.1.1 Chemicals	24
	3.1.2 Physical measurements.....	24
	3.1.3 X-ray Crystallography	24
	3.1.4 Hirshfeld surface analysis.....	25
	3.1.5 Magnetic susceptibility	25
	3.1.6 Electrochemical measurements.....	25
3.2	Synthesis of Fe(III) complexes	26
	3.2.1 Synthesis of [Fe(salBzen-5-OMe) ₂]A complexes	26
	3.2.1.1 Synthesis of [Fe(salBzen-5-OMe) ₂]Cl 1	26
	3.2.1.2 Synthesis of [Fe(salBzen-5-OMe) ₂]Br 2	27
	3.2.1.3 Synthesis of [Fe(salBzen-5-OMe) ₂]I 3	27
	3.2.1.4 Synthesis of [Fe(salBzen-5-OMe) ₂]NO ₃ 4	27
	3.2.1.5 Synthesis of [Fe(salBzen-5-OMe) ₂]ClO ₄ 5	27
	3.2.2 Synthesis of [Fe(salPren-5-OMe) ₂]A complexes	28
	3.2.2.1 Synthesis of [Fe(salPren-5-OMe) ₂]Cl 6	28
	3.2.2.2 Synthesis of [Fe(salPren-5-OMe) ₂]Br 7	28
	3.2.2.3 Synthesis of [Fe(salPren-5-OMe) ₂]I 8	29
	3.2.2.4 Synthesis of [Fe(salPren-5-OMe) ₂]NO ₃ 9	29
	3.2.2.5 Synthesis of [Fe(salPren-5-OMe) ₂]ClO ₄ 10	29
3.3	References.....	30

CONTENTS (Continued)

	Page
IV RESULTS AND DISCUSSION.....	31
4.1 Synthesis and basic characterization of Fe(III) Schiff base complexes.....	31
4.1.1 Spectroscopic study of [Fe(salRen-5-OMe) ₂]A.....	31
4.2 Structural studies of Fe(III) Schiff base complexes.....	37
4.3 Hirshfeld surface data analysis of Fe(III) Schiff base complexes.....	53
4.4 Magnetic studies of Fe(III) Schiff base complexes	56
4.5 Magnetostructural Relationship of Fe(III) complexes.....	61
4.6 Cyclic voltammetric studies of Fe(III) Schiff base complexes.....	63
4.7 References.....	69
V CONCLUSIONS.....	73
APPENDICES	75
APPENDIX A SUPPORTING INFORMATION.....	76
APPENDIX B PUBLICATION AND PRESENTATIONS.....	94
CURRICULUM VITAE	95

LIST OF TABLES

Table	Page
2.1 The guiding criteria for classifying the strength of hydrogen bonding interactions	9
4.1 IR spectroscopic data of $[\text{Fe}(\text{salRen-5-OMe})_2]\text{A}$ complexes.	34
4.2 UV-vis spectroscopic data of $[\text{Fe}(\text{salRen-5-OMe})_2]\text{A}$ complexes	36
4.3 Selected Fe-N/O bond lengths (Å) and octahedral distortion parameters (°) of 1–3 complexes	42
4.4 Selected Fe-N/O bond lengths (Å) and octahedral distortion parameters (°) of 4 and 5 complexes	43
4.5 Crystallographic data and refinement parameters for 1–3 complexes	44
4.6 Crystallographic data and refinement parameters for 4 and 5 complexes	45
4.7 Key intermolecular interactions for 1–3 complexes.....	47
4.8 Key intermolecular interactions for 4 and 5 complexes	48
4.9 Structural parameters for complexes 1–3	62
4.10 Electrochemical data of $[\text{Fe}(\text{salBzen-5-OMe})_2]\text{A}$	66
4.11 Electrochemical data of $[\text{Fe}(\text{salPren-5-OMe})_2]\text{A}$	68

LIST OF FIGURES

Figure	Page
1.1 Illustration of the spin crossover phenomenon in iron(III) complexes.....	1
2.1 Definitions of the angles use to calculate the distortion indices Σ and Θ in a six-coordinate complex.....	6
2.2 Different types of spin crossover profiles.....	7
2.3 Types of hydrogen bonding.....	9
2.4 A typical scheme for a halogen bond.....	10
2.5 π - π and C-H $\cdots\pi$ arrangements: (a) π - π face-to-face, (b) π - π offset and (c) CH $\cdots\pi$ T-shaped.	11
2.6 Diagrammatic representation of the embraces engaged by $[M(\text{phen})_n]^{x+}$ complexes. The dot is M, and the lines are phen ligand planes	11
2.7 Structure of HsalRen-X (R=ethyl group) ligand	12
2.8 (a) The magnetic profile and (b) Packing in $[\text{Fe}(\text{salEen-4-OMe})_2]\text{NO}_3$ showing the 2D supramolecular network.....	14
2.9 Spacefill packing of $[\text{Fe}(\text{salEen-5-I})_2]\text{halide}$; Cl^- (left), Br^- (center), and I^- (right) viewed along the c-axis in the HS state with the changes in the normalized N-H \cdots anion contacts upon spin crossover.....	15
2.10 Simplified illustration of $[\text{Fe}(\text{salEen-5-I})_2]\text{halide}$ viewed along the c-axis showing the three structural parameters, A-C	15
2.11 Solid-state magnetic susceptibility ($\text{cm}^3 \text{ K mol}^{-1}$) against the temperature (K) of $[\text{Fe}(\text{salEen-5-I})_2]\text{halide}$; Cl^- (1), Br^- (2), and I^- (3).....	16
2.12 Magnetic profiles of $[\text{Fe}(\text{naphBzen})_2]\text{anion}$: (a) $\text{Cl}\cdot 0.5\text{hexane}$ and (b) $\text{Br}\cdot 0.5\text{hexane}$	18
2.13 VSM $\chi_M T$ vs. T plot of $[\text{Fe}(\text{naphBzen})_2]\text{halide}$ where halide = (a) Cl and (b) = Br from 50-350 K.....	18

LIST OF FIGURES (Continued)

Figure	Page
3.1 Synthesis of $[\text{Fe}(\text{salBzen-5-OMe})_2]\text{A}$ complexes.....	26
3.2 Synthesis of $[\text{Fe}(\text{salPren-5-OMe})_2]\text{A}$ complexes.	28
4.1 IR spectra of $[\text{Fe}(\text{salBzen-5-OMe})_2]\text{A}$ complexes.....	32
4.2 IR spectra of $[\text{Fe}(\text{salPen-5-OMe})_2]\text{A}$ complexes.....	32
4.3 IR spectra of HsalPren-5-OMe and HsalBzen-5-OMe ligands	33
4.4 UV-Vis spectra of $[\text{Fe}(\text{salBzen-5-OMe})_2]\text{A}$ complexes.....	35
4.5 UV-Vis spectra of $[\text{Fe}(\text{salPren-5-OMe})_2]\text{A}$ complexes	35
4.6 View of the asymmetric unit of $[\text{Fe}(\text{salBzen-5-OMe})_2]\text{Cl}$ (1) at 150 K (left) and 295 K (right).....	39
4.7 View of the asymmetric unit of $[\text{Fe}(\text{salBzen-5-OMe})_2]\text{Br}$ (2) at 295 K.....	39
4.8 View of the asymmetric unit of $[\text{Fe}(\text{salBzen-5-OMe})_2]\text{I}$ (3) at 150 K (left) and 295 K (right).....	40
4.9 View of the asymmetric unit of $[\text{Fe}(\text{salBzen-5-OMe})_2]\text{NO}_3$ (4) at 150 K (left) and 295 K (right).....	40
4.10 View of the asymmetric unit of $[\text{Fe}(\text{salBzen-5-OMe})_2]\text{ClO}_4$ (5) at 30 K (left), 100 K (middle) and 290 K (right).....	41
4.11 Fe-N/O bond lengths (Å) of $[\text{Fe}(\text{salBzen-5-OMe})_2]\text{ClO}_4$ (5) at 30-300 K.....	41
4.12 Spacefill packing $[\text{Fe}(\text{salBzen-5-OMe})_2]\text{Cl}$ (1) at 295 K (left) and 150 K (right) viewed along the <i>b</i> axis in HS state.....	50
4.13 Spacefill packing $[\text{Fe}(\text{salBzen-5-OMe})_2]\text{Br}$ (2) at 295 K viewed along the <i>b</i> axis in HS state	51
4.14 Spacefill packing of $[\text{Fe}(\text{salBzen-5-OMe})_2]\text{I}$ (3) at 295 K viewed along the <i>c</i> axis with LS state	51
4.15 Packing of $[\text{Fe}(\text{salBzen-5-OMe})_2]\text{NO}_3$ (4) at 295 K viewed along the <i>c</i> axis in LS state.....	52
4.16 Packing of $[\text{Fe}(\text{salBzen-5-OMe})_2]\text{NO}_3$ (5) at 100 K viewed along the <i>c</i> axis in HS state.....	53

LIST OF FIGURES (Continued)

Figure	Page
4.17 Intramolecular interactions (covalent bond) (left) and C–H... π interactions (right) through Hirshfeld surface mapping by d_{norm} function.....	54
4.18 2D fingerprint plots of all contacts: H...C, H...H and H...O for 2 at 295 K.....	55
4.19 Percentage contributions of interactions for complexes 1–5	56
4.20 $\chi_{\text{M}}T$ versus T plots for 1–5 complexes.....	58
4.21 $\chi_{\text{M}}T$ versus T plots for 6–10 complexes	60
4.22 (a) Simplified illustration of 1–2 and (b) 3 viewed showing the three structural parameters, A1, A2, B and C	62
4.23 Cyclic voltammograms of [Fe(salBzen-5-OMe) ₂]A in CH ₂ Cl ₂ solution at a scan rate of 100 mVs ⁻¹	65
4.24 Cyclic voltammograms of [Fe(salBzen-5-OMe) ₂]I in CH ₂ Cl ₂ solution at a scan rate of 100 mVs ⁻¹	65
4.25 Cyclic voltammograms of [Fe(salPren-5-OMe) ₂]A in CH ₂ Cl ₂ solution at a scan rate of 100 mVs ⁻¹	67
4.26 Cyclic voltammograms of [Fe(salPren-5-OMe) ₂]I in CH ₂ Cl ₂ solution at a scan rate of 100 mVs ⁻¹	67

LIST OF ABBREVIATIONS

Symbols and Abbreviations	Full Words/Definitions
...	Non-covalent interaction or non-bonded interatomic separation
Å	Angstrom
λ	Lambda
ν	Wavenumber (cm^{-1})
ϵ	Absorption coefficient
χ_M^T	Magnetic susceptibility as a function of temperature
χ_M	Magnetic susceptibility equal to M/H per mole of the complex
S	Overall spin state of the molecular substance
T	Temperature
P	Paring energy
Δ_{oct}	Ligand field splitting parameter
t_{2g}	triply degenerate orbital level
e_g	Doubly degenerate orbital level
Σ	Sigma/Octahedral distortion parameter
Θ	Theta/ Trigonal twist
O_h	Octahedral
D_{3h}	Trigonal prismatic
ϕ_i	Ligand-metal-ligand angles
θ_i	Pseudo-threefold axis
γ_{HS}	High spin fraction
ca.	Approximately

LIST OF ABBREVIATIONS (Continued)

Symbols and Abbreviations	Full Words/Definitions
Cl^-	Chloride ion
Br^-	Bromide ion
I^-	Iodide ion
NO_3^-	Nitrate ion
ClO_4^-	Perchlorate ion
NO	Nitric oxide
CN	Cyanide
NCS	Thiocyanate
PF_6^-	hexafluorophosphate
Bh_4^-	Tetraphenylborate
FT-IR	Fourier Transform Infrared
UV-Vis	Ultraviolet-Visible
PXRD	Powder X-ray diffraction
SQUID	Superconducting Quantum Interference Device
SCO	Spin crossover
ST	Spin transition
HS	High spin
LS	Low spin
mHS	Mostly high spin
salBzen-5-OMe	2-[[2-(benzylamino)ethylimino]methyl} phenolate
salPren-5-OMe	2-[[2-(propylamino)ethylimino]methyl} phenolate
OMe	Methoxy

LIST OF ABBREVIATIONS (Continued)

Symbols and Abbreviations	Full Words/Definitions
salRen	N-Alkylaminoethylamine and a salicylaldehyde derivative
salEen	2-[[2-(ethylamino)ethylimino]methyl]-4-phenolate
LIESST	light-induced excited spin state trapping
EF	Two edge-to-face
OFF	Offset face-to-face
P4AE	Parallel fourfold aryl embraces
DMF	Dimethylformamide
EtOH	Ethanol
CHCl ₃	Chloroform
CH ₂ Cl ₂	Dichloromethane
Oe	Oersteds
d _{norm}	Distances normalized
E°'	Electrode potential measured at 1 atmosphere pressure
AgCl	Silver chloride
LiCl	Lithium chloride
CaH ₂	Calcium hydride
[Fe(η -C ₅ H ₅) ₂]	Ferrocene
[N- <i>n</i> Bu ₄][PF ₆]	Tetrabutylammonium hexafluorophosphate.
LMCT	Ligand-to-metal charge transfer
et al	et alia, in Latin meaning “and others”

CHAPTER I

INTRODUCTION

1.1 Background

Spin-crossover (SCO) complexes, also known as spin-transition (ST) complexes, represent a fascinating class of switchable molecules. Their switching process can be triggered by external stimuli such as changes in temperature, pressure, magnetic field, or exposure to light (Hauser, 2013) as shown in Figure 1.1. In iron(III) systems with d^5 electron configuration, this transition involves a shift from a high-spin state (6A_1 , $S = 5/2$) to a low spin state (2T_2 , $S = 1/2$), with both states exhibiting paramagnetic behavior (van Koningsbruggen et al., 2004), (Nihei et al., 2007). SCO materials are attractive candidates for molecular magnetic devices and sensors, because switching can occur at or near ambient temperature. Compared to the more commonly studied Fe(II) systems, Fe(III) compounds offer greater air stability, making them promising candidates for future device applications. For practical use, it is also essential that the spin crossover (SCO) occurs sharply and exhibits a hysteresis of at least 40 K. In SCO complexes, hysteresis arises from strong interactions between SCO centers, which facilitate rapid propagation of the transition throughout the material. This connectivity can be achieved via coordination bonds or, more frequently, through supramolecular interactions. Consequently, effective SCO material design relies on the principles of crystal engineering (Harding et al., 2016).

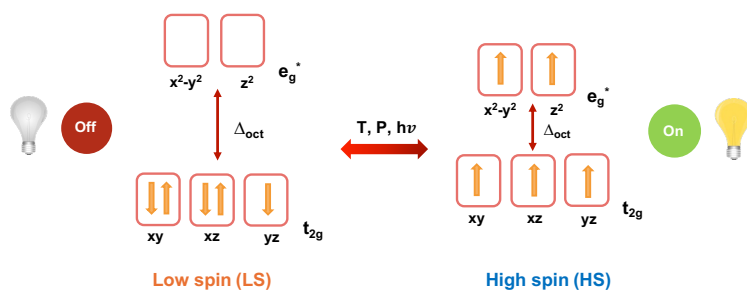


Figure 1.1 Illustration of the spin crossover phenomenon in iron(III) complexes.

1.2 Research objectives

The broad objective of this thesis is to explore the molecular magnetism of simple iron complexes and develop a better understanding of the structure:function relationships that exist in these systems. Specifically, we aim to:

1.2.1 To synthesize new Schiff base ligands with N_2O donor set.

1.2.2 To synthesize and characterize $[Fe(salBzen-5-OMe)_2]A$ and $[Fe(salPren-5-OMe)_2]A$ where $A = Cl^-$, Br^- , I^- , NO_3^- , and ClO_4^- complexes using FT-IR, UV-Vis spectroscopy, elemental analysis, mass spectrometry, and Powder X-ray diffraction.

1.2.3 To study the structures of the iron(III) salRen complexes using single crystal X-ray crystallography.

1.2.4 To investigate the magnetic properties of the iron(III) salRen complexes using SQUID magnetometry.

1.2.5 To explore the electron transfer processes in $[Fe(salBzen-5-OMe)_2]A$ and $[Fe(salPren-5-OMe)_2]A$ complexes with cyclic voltammetry.

1.2.6 To study the impact of the anion and the ligand substituent position on the interaction and magnetic performance as an aid to understanding the structure:function relationships in this novel series of Fe(III) spin crossover systems.

1.3 Scope and limitation of the study

This research aims to synthesize $[Fe(salRen-5-OMe)_2]A$ complexes with different counter ions ($A = Cl^-$, Br^- , I^- , NO_3^- , and ClO_4^-) and substituent groups on the ligands ($R = salBzen-5-OMe$, $salPren-5-OMe$) and characterize both series by infrared (IR), UV-Visible spectroscopy, elemental analysis, mass spectrometry, Powder X-ray diffraction, X-ray crystallography, cyclic voltammetry, and SQUID magnetometry.

1.4 References

- Harding, D. J., Harding, P., and Phonsri, W. (2016). Spin crossover in iron(III) complexes. *Coordination Chemistry Reviews*, 313, 38–61.
doi: <https://doi.org/10.1016/j.ccr.2016.01.006>
- Hauser, A. (2013). Spin-Crossover Materials. Properties and Applications. Edited by Malcolm A. Halcrow. *Angewandte Chemie International Edition*, 52(40), 10419.
doi: <https://doi.org/10.1002/anie.201306160>
- Nihei, M., Shiga, T., Maeda, Y., and Oshio, H. (2007). Spin crossover iron(III) complexes. *Coordination Chemistry Reviews*, 251(21–24), 2606–2621.
doi: 10.1016/j.ccr.2007.08.007
- van Koningsbruggen, P. J., Maeda, Y., and Oshio, H. (2004). Spin Crossover in Transition Metal Compounds I. In Iron(III) Spin Crossover Compounds (Vol. 233, pp. 259–324). Springer-Verlag: Berlin, Heidelberg, New York. doi: 10.1007/b95409



CHAPTER II

LITERATURE REVIEW

2.1 The spin crossover phenomenon

Spin crossover (SCO) is a phenomenon primarily observed in first-row transition metal complexes with a d^4 - d^7 electron configuration and an octahedral coordination. (Hayami et al., 2003; Nihei et al., 2007). The shift between high spin (HS) and low spin (LS) states is determined by the respective splitting energy (Δ_{oct}) and electron pairing energy (P) of the system. In a crystal field diagram, the t_{2g} orbitals (lower level) and e_g orbitals (upper level) represent two distinct energy levels. When $\Delta_{\text{oct}} > P$, the t_{2g} orbitals are filled before populating the e_g orbitals, resulting in lower paramagnetic or diamagnetic properties, commonly referred to as the low spin state. On the other hand, when $\Delta_{\text{oct}} < P$, the electrons preferentially occupy the half-filled t_{2g} orbitals and then populate the e_g orbitals, resulting in a more paramagnetic state known as the high spin state (Martinho et al., 2020). However, in cases where $\Delta_{\text{oct}} \approx P$, both the low spin and high spin states are possible. Application of an external stimuli such as pressure, light, and temperature can induce a spin state change (Tsukiashi et al., 2018). This phenomenon is termed spin crossover.

The spin state transition in Fe(III) SCO occurs between the $S = 5/2$ (6A_1) HS state and $S = 1/2$ (2T_2) LS state and differs from Fe(II) in that both spin states are paramagnetic. This difference has a significant impact on the alteration of the Fe-ligand bond lengths during SCO. Typically, the bond length change upon SCO is around 0.10 – 0.13 Å, whereas Fe(II) systems exhibit approximately 0.20 Å bond length change (Hauser, 2013; Nihei et al., 2007; van Koningsbruggen et al., 2004). In the HS species, the coordination bond lengths are longer compared to the LS species. This discrepancy arises from the presence of unpaired electrons in the anti-bonding e_g orbitals in the HS state, while there are no electrons in the e_g orbitals for the LS species (Nihei et al., 2007). This distinction is crucial because the relatively smaller bond length change

between the two spin states makes light-activated Fe(III) SCO systems exceptionally rare. In these systems, the HS state induced by light quickly relaxes to the LS state.

This effect is known as light-induced excited spin state trapping (LIESST) in SCO complexes (Boonprab et al., 2019).

2.2 Measurement techniques

2.1.1 X-ray crystallography

Single crystal X-ray diffraction is a powerful technique employed to precisely determine the three-dimensional atomic structure of crystalline solids and investigate structural changes in complexes. The properties and functions of materials are significantly influenced by their crystal structures. Moreover, crystal structures provide valuable insights into whether a compound is in a HS or LS state, which can be determined by analyzing the metal-ligand bond lengths. This information reveals details about chemical bonding and any disorder present. Consequently, X-ray diffraction techniques find wide application in materials research.

2.1.1.1 Metal-ligand bond length

Changes in metal-ligand bond lengths are utilized to determine if spin crossover has occurred. In Fe(III) systems, the Fe-O/N bond lengths in the LS and HS states are generally 1.85-1.90 / 1.90-1.96 Å and 1.90-1.95 / 2.01-2.22 Å, respectively. These bond length fluctuations are less than those observed in Fe(II) complexes with Fe-N bond lengths of ca. 1.8-2.0 Å in the LS state and ca. 2.0-2.2 Å in the HS state (Díaz-Torres et al., 2020; Phonsri et al., 2017).

2.1.1.2 Distortion in octahedral coordination complexes

The mean metal-ligand distances within the octahedral coordination sphere are measured by d_{mean} , one of the easiest metrics to trace this change. The parameters Σ and Θ have been introduced and utilized to describe angular and torsional distortions, respectively. Σ denotes general deviations from an ideal octahedral structure of the metal ion complex, whereas Θ denotes a distortion from a perfect octahedral (O_h) to a trigonal prismatic (D_{3h}) geometry (Ketkaew et al., 2021). The mathematical formulations of Σ and Θ parameters are expressed through the following equations 2.1 and 2.2 respectively. Descriptions of the angles used to

calculate the distortion indices Σ and Θ for a six-coordinate complex are shown in Figure 2.1 (Halcrow, 2011).

$$\Theta = \sum_{i=1}^{24} |\theta_i - 60| \quad \text{Equation 2.2}$$

$$\Sigma = \sum_{i=1}^{12} |\phi_i - 90| \quad \text{Equation 2.1}$$



Figure 2.1 Definitions of the angles use to calculate the distortion indices Σ and Θ in a six-coordinate complex.

The parameter Σ is the sum of 12 different *cis* ligand-metal-ligand angles (ϕ_i) that differ from 90 degrees. The parameter Θ quantifies the extent of trigonal distortion in coordination geometry, describing the transition from an octahedral to a trigonal prismatic arrangement. It is calculated as the sum of the deviations of 24 distinct torsional angles (θ_i)—measured between ligand atoms on opposing triangular faces of the octahedron along the pseudo-threefold axis—from the ideal 60°. Nearly two decades ago, Marchivie et al. established the significance of the Θ parameter, demonstrating that variations in Θ between the high-spin (HS) and low-spin (LS) states are correlated with the limiting temperature for photo-inscription, T(LIESST). The values of Σ and Θ for a perfect octahedron are zero in all cases. Recently, Ketkaew *et al.* released OctaDist, a program to calculate these distortion parameters in octahedral complexes (Ketkaew et al., 2021).

2.1.2 SQUID magnetometry

The magnetic profile of a spin crossover (SCO) compound is primarily determined by measuring its magnetic susceptibility ($\chi_M T$) as a function of temperature. The value of $\chi_M T$ is influenced by the temperature-dependent contributions of the high-spin χ_{HS} and low-spin χ_{LS} states. A spin transition occurs when changes in the occupancy of the t_{2g} and e_g orbitals lead to an expansion of the metal-ligand bond length, altering the system's paramagnetic properties. Since the susceptibilities and mole fractions of both spin states can be determined at any given temperature, the spin transition curve can be plotted. Specifically, a graph of the high-spin fraction (χ_{HS}) versus temperature illustrates the progression of the transition (Clarke et al., 2004).

Several characteristic types of spin transition curves exist, as shown in Figure 2.2: (a) abrupt transitions, which exhibit strong cooperativity and are suitable for switching applications; (b) gradual transitions, where cooperative interactions are weak; (c) multi-step transitions, in which a molecule transitions from a binary to a ternary or higher-order switch; (d) abrupt spin crossover with hysteresis, applicable in memory devices; and (e) incomplete transitions. An abrupt spin transition with hysteresis is a key example of bistability, indicating strong cooperative interactions within the material (Clarke et al., 2004; Martinho et al., 2020)

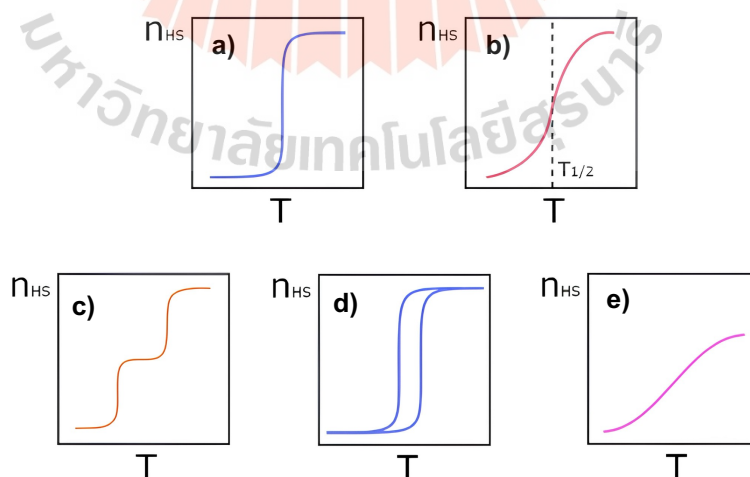


Figure 2.2 Different types of spin crossover profiles.

2.3 Supramolecular Interactions

Components in the lattice, such as solvents, host molecules, and counter ions, play a significant role in controlling the characteristics of the interactions between metal centers and the extent of communication among them. The properties and arrangement of the ligands play a crucial role in enhancing interactions between metal centers. The capacity to form intermolecular interactions is nearly as important as possessing the appropriate ligand-field strength to modulate the balance between Δ_{oct} and P. When the compounds are ionic, the strongest intermolecular interactions will be electrostatic. Hydrogen bonds between ligands and host molecules or solvates can range from the classic, involving the more electronegative elements, to the weak, where C-H is a ubiquitous donor. Specific functional groups may enhance π - π and C-H $\cdots\pi$ interactions (Calhorda et al., 2013), and the presence of halogens can potentially lead to the formation of halogen bonds (G. R. Desiraju et al., 2013). Although some of these interactions may seem quite weak, cooperative effects in the solid state can significantly enhance their importance. For example, the incorporation of a cationic Fe(III) complex into a halogen-bonded supramolecular framework has been shown to influence spin crossover (Jeon et al., 2017).

2.3.1 Hydrogen bonding

The hydrogen bond is the interaction between a hydrogen atom (hydrogen bond donor) commonly attached to N, O, or F and another atom with unshared electrons (hydrogen bond acceptor), denoted as D-H \cdots A. D-H is a proton donor to A in this interaction. A normal hydrogen bond has only one acceptor and is classified as either linear or bent depending on the angle of D-H \cdots A. However, bifurcated, and trifurcated hydrogen bonds are other common types of hydrogen interactions (Figure 2.3). There are two or three donors or acceptors in a bifurcated or trifurcated hydrogen bond.

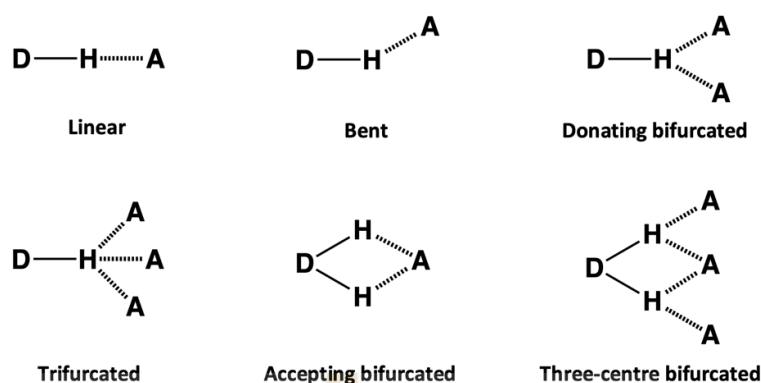


Figure 2.3 Types of hydrogen bonding.

The distance between the donor and acceptor atoms ($H\cdots A$ and $D\cdots A$) as well as the angle ($D-H\cdots A$) can be used to investigate the strength of a hydrogen bond. The distance between $H\cdots A$ should be shorter than the van der Waals radii, and the angle should be near to 180° (G. Desiraju, 2005) as shown in Table 2.1.

Table 2.1 The guiding criteria for classifying the strength of hydrogen bonding interactions.

Interaction	Strong	Moderate	Weak
Interaction type	Strongly covalent	Mainly electrostatic	Electrostatic
Bond energy (kJ mol^{-1})	60-120	16-60	<12
Bond length (\AA)			
$H\cdots A$	1.2-1.5	1.5-2.2	2.2-3.2
$D\cdots A$	2.2-2.5	2.5-3.2	3.2-4.0
Bond angle ($^\circ$)	175-180	130-180	90-150

2.3.2 Halogen bonding

When a halogen atom forms a covalent bond with another element, such as in a carbon-halogen ($C-X$) bond, it develops a distinctive electrostatic potential distribution. This includes a positively charged polar cap, known as a σ -hole, and a negatively charged equatorial belt. The σ -hole serves as an electrophilic site

that can interact with nucleophiles, while the electron-rich equatorial belt can engage with electrophiles from other molecules.

In 2013, the International Union of Pure and Applied Chemistry (IUPAC) defined halogen bonding as “a halogen bond is formed when a halogen atom’s electrophilic region interacts attractively with a nucleophilic region within the same or a different molecular entity” (G. R. Desiraju et al., 2013). Figure 2.4 presents a representative scheme illustrating a halogen bond.

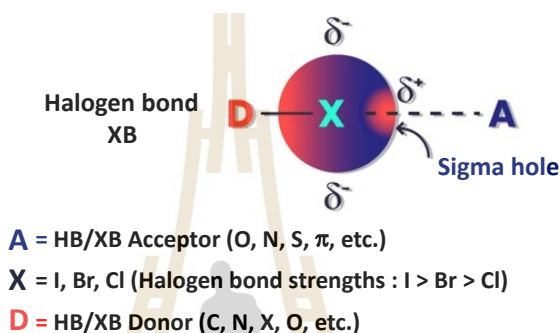


Figure 2.4 A typical scheme for a halogen bond.

2.3.3 π - π and C-H $\cdots\pi$ interactions

Aromatic interactions involving π - π , cation- π , and anion- π interactions are commonly seen in molecular complexes. π - π interactions typically have an interplanar distance in the range of 3.3-3.8 Å. The aromatic rings can be arranged parallel in either face-to-face or an offset arrangement, Figure 2.5(a) and Figure 2.5(b), respectively. However, when the aromatic planes are perpendicular, a C-H $\cdots\pi$ interaction is observed Figure 2.5(c) (Molčanov et al., 2019).

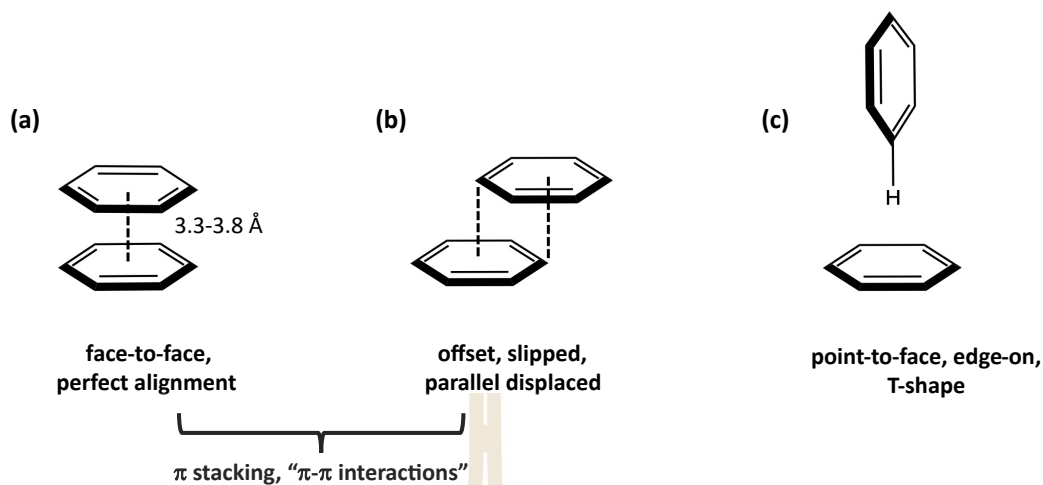


Figure 2.5 π - π and C-H $\cdots\pi$ arrangements: (a) π - π face-to-face, (b) π - π offset and (c) C-H $\cdots\pi$ T-shaped.

Parallel fourfold aryl embraces, or P4AE, are made up of one offset face-to-face (OFF) motif and two edge-to-face (EF) motifs that overlap in multiple areas. Therefore, they must have C-H $\cdots\pi$ and π - π interactions. These are represented diagrammatically in Figure 2.6 (Russell et al., 2001).

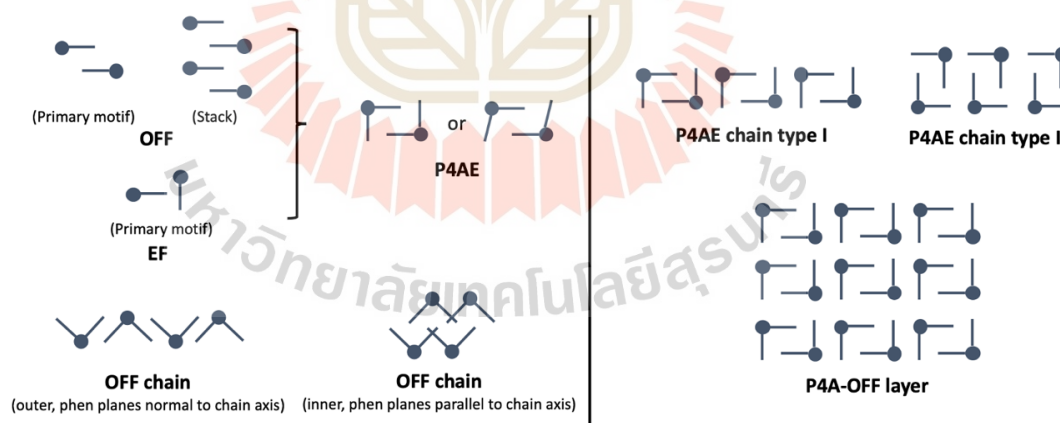


Figure 2.6 Diagrammatic representation of the embraces formed by $[M(\text{phen})_n]^{x+}$ complexes, where the central dot represents the metal center (M), and the lines depict the planes of the phen ligands.

2.4 Spin crossover iron(III)-ethylsalicylaldimine complexes

2.4.1 SalRen ligands

N-Alkylaminoethylamine and a salicylaldehyde derivative are utilized to synthesize the tridentate ligands known as HsalRen. The NH group on the ligand enhances cooperativity by enabling hydrogen bonding. While various alkyl groups have been previously studied, recent publications predominantly feature ligands containing an ethyl group as shown in Figure 2.7 (Al-Azzani et al., 2020; Sheu et al., 2013). The design of this ligand aims to explore the structural and interaction properties of SCO compounds. Additionally, considerable efforts have been devoted to investigating the impact on SCO characteristics (Harding et al., 2016).

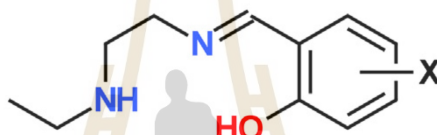


Figure 2.7 Structure of HsalRen-X (R=ethyl group) ligand.

The Hsal-R-en-X ligand family is widely used in SCO research (Dey et al., 2020, 2022, 2023). Compounds containing these ligands exhibit a variety of SCO behaviors, including abrupt SCO in $[\text{Fe}(\text{salEen-3-OMe})_2]\text{PF}_6$ (Haddad et al., 1980, 1981), SCO with an 8 K hysteresis in $[\text{Fe}(\text{salEen-4-OMe})_2]\text{NO}_3$ (Tissot et al., 2014), and near room-temperature SCO in $[\text{Fe}(\text{salEen-3,5-Br}_2)_2]\text{BPh}_4$ (Martinho et al., 2014). Structural contractions associated with SCO have been observed in $[\text{Fe}(\text{salEen-4-Br})_2]\text{ClO}_4$ and $[\text{Fe}(\text{salEen-5-I})_2]\text{ClO}_4$ (Bento et al., 2024; Martins et al., 2018; Vicente et al., 2016), resulting in thermosalient properties. While previous studies have primarily focused on the influence of halide substituents, the effect of the anion on these SCO behaviors remains largely unexamined.

2.4.2 Anion effects

The reaction between the salEen ligand and $\text{Fe}(\text{ClO}_4)_3$ in EtOH resulted in the formation of $[\text{Fe}(\text{salEen})_2]\text{ClO}_4$ and $[\text{Fe}(\text{salEen})_2]\text{ClO}_4 \cdot 0.5\text{H}_2\text{O}$ (Sheu et al., 2013). Both compounds exhibit a gradual SCO behavior, with the non-solvated form displaying a higher $T_{1/2}$ value and a more abrupt SCO transition. Interestingly, the crystal structures of both compounds indicate a slightly greater change in Fe–N/O bond lengths during spin crossover (SCO) for $[\text{Fe}(\text{salEen})_2]\text{ClO}_4 \cdot 0.5\text{H}_2\text{O}$. In both structures, the molecular packing is primarily stabilized by strong N–H...anion interactions, which are characteristic of $[\text{Fe}(\text{salEen})_2]^+$ complexes. The lack of significant supramolecular interactions accounts for the gradual nature of the SCO in both cases.

Likewise, $[\text{Fe}(\text{salEen})_2][\text{Fe}(\text{CN})_5(\text{NO})]$ exhibits a gradual SCO between 100 and 400 K (Faulmann et al., 2013), despite having different anions. The packing in the structure remains largely unchanged compared to $[\text{Fe}(\text{salEen})_2]\text{ClO}_4 \cdot \text{sol}$, resulting in weak connections between the cationic units but strong cation-anion interactions. $[\text{Fe}(\text{salEen-3-OMe})_2]\text{PF}_6$ was synthesized, and magnetic studies indicate a highly abrupt SCO transition at approximately 165 K with a hysteresis of 3 K (Tissot et al., 2011). The structures of the complex at 300 K, 200 K, and 100 K reveal a HS Fe(III) center, HS Fe(III) center, and LS Fe(III) center, respectively. The average change in Fe–N/O bond lengths is around 0.13 Å, which is slightly larger than found in other $[\text{Fe}(\text{salEen})_2]^+$ complexes.

The related complexes, $[\text{Fe}(\text{salEen-4-OMe})_2]\text{Y}$ ($\text{Y} = \text{NO}_3^-$, PF_6^-), when the anion is NO_3^- the SCO is abrupt at approximately 78 K, with a hysteresis of 7.5 K (Tissot et al., 2014). Structural studies confirm the presence of SCO in both compounds. Interestingly, $[\text{Fe}(\text{salEen-4-OMe})_2]\text{PF}_6$ exhibits two independent Fe(III) centers, whereas $[\text{Fe}(\text{salEen-4-OMe})_2]\text{NO}_3$ contains a single Fe(III) center. In $[\text{Fe}(\text{salEen-4-OMe})_2]\text{NO}_3$, a 2D supramolecular network is formed through a combination of N–H...O and C–H...O interactions involving the NO_3 anions (Figure 2.8). Conversely, $[\text{Fe}(\text{salEen-4-OMe})_2]\text{PF}_6$ displays very weak contacts between the cations, resulting in two centers that undergo SCO at identical temperatures, leading to a gradual SCO.

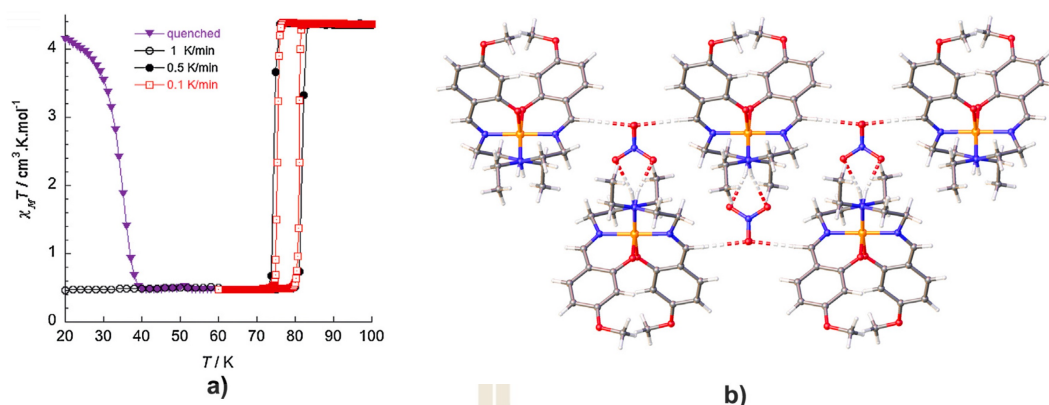


Figure 2.8 (a) The magnetic profile and (b) Packing in $[\text{Fe}(\text{salEen-4-OMe})_2]\text{NO}_3$ showing the 2D supramolecular network (Harding et al., 2016).

Harding et al. recently published a series of three structurally identical Fe(III) complexes, $[\text{Fe}(\text{salEen-5-I})_2]\text{halide}$ (Boonprab et al., 2024) where the absence of lattice solvents enables a direct comparison of their properties. Their findings indicate that larger anions are more likely to stabilize the LS state. Notably, $[\text{Fe}(\text{salEen-5-I})_2]\text{Br}$ exhibits a stepped SCO transition near room temperature around 288 K, while $[\text{Fe}(\text{salEen-5-I})_2]\text{Cl}$ and $[\text{Fe}(\text{salEen-5-I})_2]\text{I}$ display gradual and incomplete SCO transitions over a broad temperature range over 200 K (Figure 2.11). Structural analysis shows that N-H...anion and C-H...anion interactions link the cations into two-dimensional Diamond-shaped sheets (Figure 2.9). By employing structural parameters A–C (Figure 2.10) to characterize nearest and next-nearest neighbor interactions, the abruptness and stepped nature of the SCO transition in $[\text{Fe}(\text{salEen-5-I})_2]\text{Br}$ can be rationalized. Comparisons with related complexes, such as $[\text{Fe}(\text{salEen-5-Br})_2]\text{ClO}_4$ and $[\text{Fe}(\text{salEen-5-I})_2]\text{ClO}_4$ (Martins et al., 2018; Vicente et al., 2016), suggest that this magnetic-structural correlation extends to a wider range within this family of compounds.

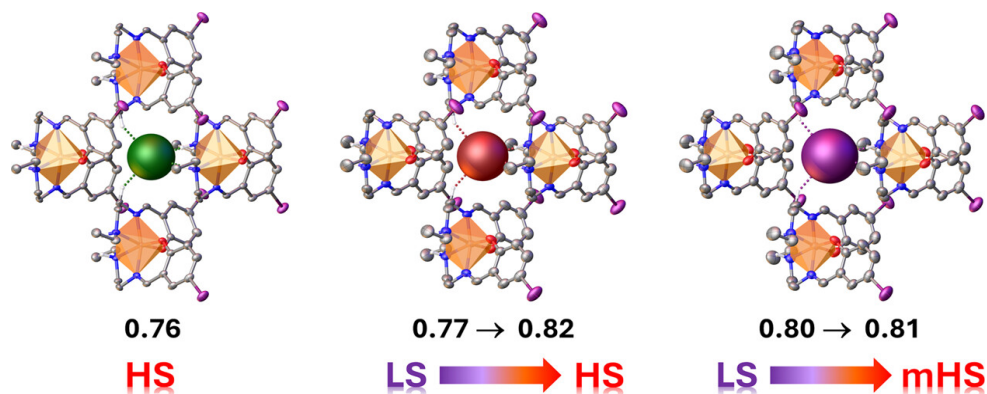


Figure 2.9 Space-filling packing of $[\text{Fe}(\text{salEen-5-I})_2]\text{halide}$; Cl^- (left), Br^- (center), and I^- (right) viewed along the c -axis in the HS state, showing changes in normalized N–H...anion contacts during spin crossover (Boonprab et al., 2024).

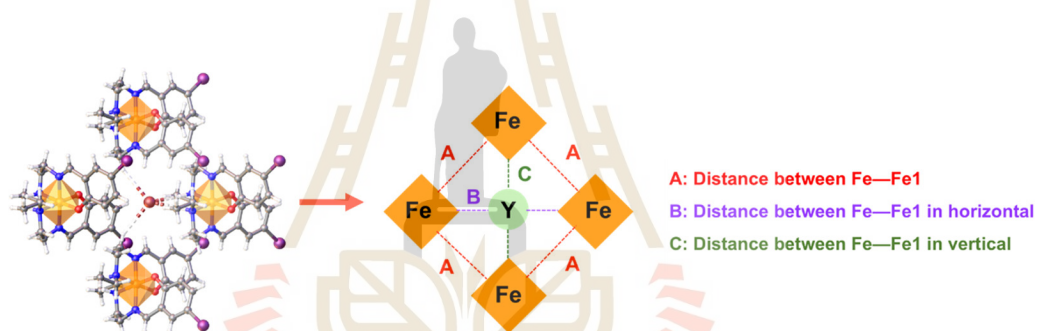


Figure 2.10 A simplified representation of $[\text{Fe}(\text{salEen-5-I})_2]\text{halide}$ viewed along the c -axis, highlights three key structural parameters: A, B, and C (Boonprab et al., 2024).

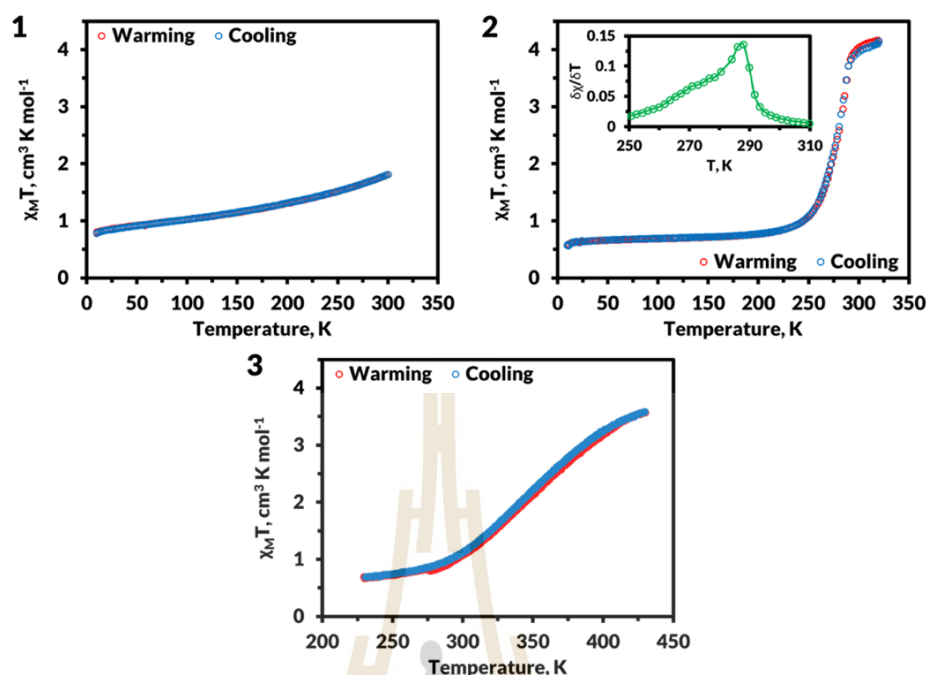


Figure 2.11 Magnetic susceptibility in the solid state ($\text{cm}^3 \text{K mol}^{-1}$) vs. temperature (K) for $[\text{Fe}(\text{salEen-5-I})_2]\text{halide}$; Cl^- (1), Br^- (2), and I^- (3) (Boonprab et al., 2024).

The magnetic behavior of Fe(III) complexes undergoes changes when different anions are present. However, only a limited number of anions have been extensively studied, including NCS , ClO_4 , PF_6 and BPh_4 . Moreover, there are only a few systematic studies focusing on the effects of varying anions. Within the $[\text{Fe}(\text{qsal-5-OMe})_2]\text{Y}$ {qsal = N-(8-quinoly)salicylaldimine} system, LS complexes are produced with small anions, while intermediate sized anions induce SCO behavior (Sertphon et al., 2013). Conversely, in the case of $[\text{Fe}(\text{Him})_2(\text{hapien})]^+$ complexes, HS behavior is observed with small anions, whereas SCO active systems are associated with intermediate to large anions (Koike et al., 2013). These examples highlight that there is no universal rule governing the promotion of SCO by specific anions, as each ligand system exhibits unique characteristics influenced by factors such as the shape, size, and supramolecular preferences of the anions. In most cases, these factors significantly alter the crystal lattice, thereby impacting the SCO behavior. Consequently, the influence of anions on SCO characteristics is less predictable compared to the effects of solvents (Harding et al., 2016).

2.4.3 Solvent effects

In some cases, the selection of solvent is a key factor in influencing SCO properties. For instance, Martinho *et al.* recently investigated the SCO behavior of $[\text{Fe}(\text{3,5-Br}_2\text{-salEen})_2]\text{Y}\cdot\text{sol}$ ($\text{Y} = \text{ClO}_4$, $\text{sol} = \text{EtOH}$; $\text{Y} = \text{BPh}_4$, $\text{sol} = \text{DMF}$) (Martinho *et al.*, 2014). When the anion is BPh_4 , the compound exhibits a very gradual and incomplete SCO, whereas the ClO_4 complex remains in the LS state up to 350 K. The structure of $[\text{Fe}(\text{3,5-Br}_2\text{-salEen})_2]\text{BPh}_4\cdot\text{DMF}$ at 150 K shows that the Fe(III) center is in the LS state, and unlike other $[\text{Fe}(\text{X-salEen})_2]^+$ complexes, there are no anion-N-H interactions. Instead, hydrogen bonding occurs between the NH groups and the DMF carbonyl oxygen atom. This significantly reduces cooperativity as the DMF molecule is no longer involved in any supramolecular interactions, aligning with the gradual SCO behavior observed in this compound.

A related series of $[\text{Fe}(\text{naphBzen})_2]\text{halide}$ complexes, specifically $[\text{Fe}(\text{naphBzen})_2]\text{Cl}$ and $[\text{Fe}(\text{naphBzen})_2]\text{Br}$ (Habarakada *et al.*, 2022), demonstrates that different solvates can be obtained through recrystallization from various solvents. Solvent selection is a key factor in determining the spin state of Fe(III) complexes. For example, the hexane solvates exhibit SCO behavior (Figure 2.12), whereas CHCl_3 solvates and nonsolvated systems remain in a LS state at elevated temperatures (Figure 2.13). This highlights the significant influence of solvent interactions in stabilizing specific spin states. A notable aspect of the structures is the shorter N-H...halide interactions observed in the CHCl_3 and nonsolvated systems. The results suggest a minimum interaction distance of approximately 2.26 Å for Cl^- and 2.43 Å for Br^- below which SCO does not occur. Furthermore, it is evident that an increase in anion size from chloride to iodide leads to a stronger preference for the HS state. Interestingly, SCO behavior is observed exclusively in the hexane solvates, implying that even the weak interactions characteristic of nonpolar solvents can influence SCO properties. Whether this effect is applicable to other SCO systems remains an open question.

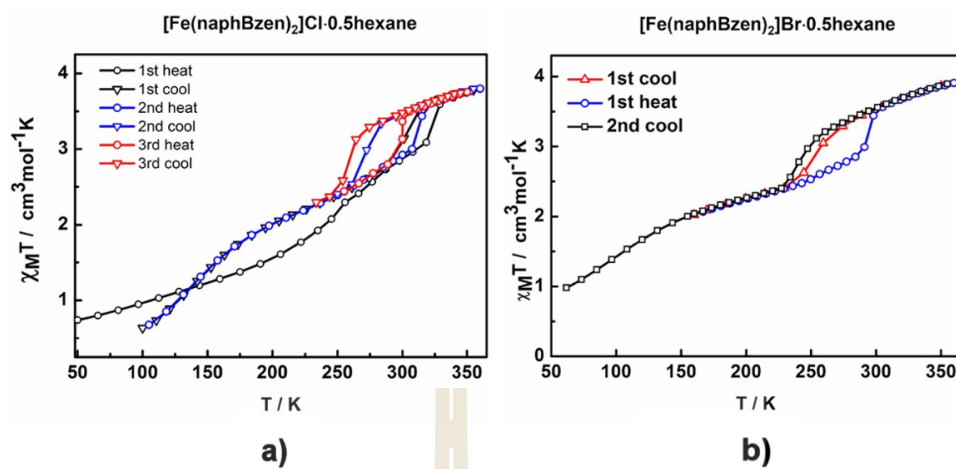


Figure 2.12 Magnetic profiles of [Fe(naphBzen)₂]anion: (a) Cl·0.5hexane and (b) Br·0.5hexane (Habarakada et al., 2022).

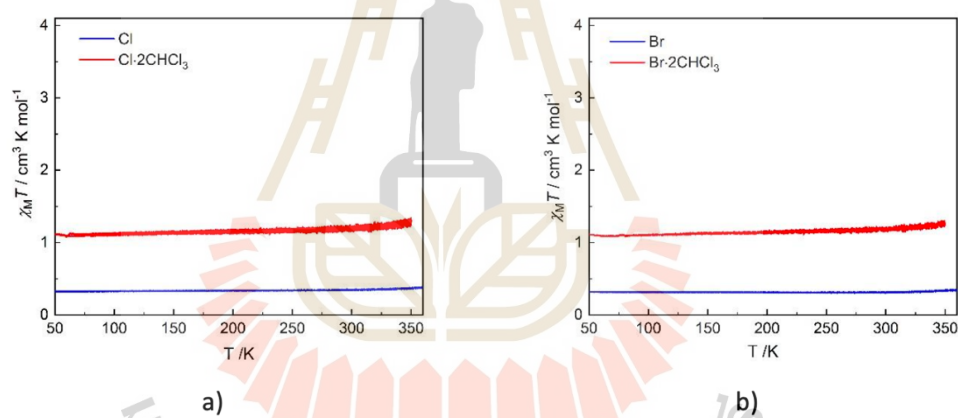


Figure 2.13 VSM $\chi_M T$ vs. T plot of [Fe(naphBzen)₂]halide where halide = (a) Cl and (b) = Br from 50-350 K (Habarakada et al., 2022).

2.5 References

- Al-Azzani, M. A., Al-Mjeni, F., Mitsuhashi, R., Mikuriya, M., Al-Omari, I. A., Robertson, C. C., Bill, E., and Shongwe, M. S. (2020). Unusual Magneto-Structural Features of the Halo-Substituted Materials $[\text{Fe}^{\text{III}}(\text{5-X-salMeen})_2]\text{Y}$: a Cooperative $[\text{HS-HS}] \leftrightarrow [\text{HS-LS}]$ Spin Transition. *Chemistry – A European Journal*, 26(21), 4766–4779. doi: <https://doi.org/10.1002/chem.201904744>
- Bento, M. A., Gomes, T., Martins, F. F., Gil, A., Ferreira, L. P., Barroso, S., Gomes, C. S. B., Garcia, Y., and Martinho, P. N. (2024). The role of intermolecular interactions in $[\text{Fe}(\text{X-salEen})_2]\text{ClO}_4$ spin crossover complexes. *Dalton Trans.*, 53(20), 8791–8802. doi: 10.1039/D4DT00400K
- Boonprab, T., Lee, S. J., Telfer, S. G., Murray, K. S., Phonsri, W., Chastanet, G., Collet, E., Trzop, E., Jameson, G. N. L., Harding, P., and Harding, D. J. (2019). The First Observation of Hidden Hysteresis in an Iron(III) Spin-Crossover Complex. *Angewandte Chemie International Edition*, 58(34), 11811–11815. doi: <https://doi.org/10.1002/anie.201907619>
- Boonprab, T., Thammasangwan, W., Chastanet, G., Gonidec, M., Harding, P., and Harding, D. J. (2024). Halide Anion Effects and Magnetostructural Relationships in Iron(III) Spin Crossover Complexes. *Crystal Growth & Design*, 24, 8145–8152. doi: 10.1021/acs.cgd.4c01068.
- Calhorda, M. J., and Costa, P. (2013). Weak Hydrogen Bonding. *Comprehensive Inorganic Chemistry II (Second Edition): From Elements to Applications*, 9, 341–357. doi: 10.1016/B978-0-08-097774-4.00912-8
- Clarke, J., and Braginski, A. I. (2004). *The SQUID Handbook Vol. I The SQUID Handbook* (Vol. 1). Retrieved from <http://dnb.ddb.de>
- Desiraju, G. (2005). The Supramolecular Synthon in Crystal Engineering. In *Stimulating Concepts in Chemistry* (pp. 293–306). doi: 10.1002/3527605746.ch19
- Desiraju, G. R., Ho, P. S., Kloo, L., Legon, A. C., Marquardt, R., Metrangolo, P., Politzer, P., Resnati, G., and Rissanen, K. (2013). Definition of the halogen bond (IUPAC Recommendations 2013): *Pure and Applied Chemistry*, 85(8), 1711–1713. doi: 10.1351/PAC-REC-12-05-10

- Dey, B., Cirera, J., Mehta, S., Ferreira, L. P., Arumugam, R., Mondal, A., Martinho, P. N., and Chandrasekhar, V. (2023). Steric Effects on Spin States in a Series of Fe(III) Complexes. *Crystal Growth & Design*, 23(9), 6668–6678. doi: 10.1021/acs.cgd.3c00555
- Dey, B., Gupta, A., Kapurwan, S., and Konar, S. (2020). Study of Spin Crossover Property of a Series of X-OMe-SalEen (X=6, 5 and 4) Based Fe(III) Complexes. *ChemistrySelect*, 5(46), 14677–14684. doi: <https://doi.org/10.1002/slct.202003135>
- Dey, B., Mehta, S., Mondal, A., Cirera, J., Colacio, E., and Chandrasekhar, V. (2022). Push and Pull Effect of Methoxy and Nitro Groups Modifies the Spin-State Switching Temperature in Fe(III) Complexes. *ACS Omega*, 7(43), 39268–39279. doi: 10.1021/acsomega.2c05380
- Díaz-Torres, R., Phonsri, W., Murray, K. S., Liu, L., Ahmed, M., Neville, S. M., Harding, P., and Harding, D. J. (2020). Spin Crossover in Iron(III) Quinolylsalicylaldimines: The Curious Case of [Fe(qsal-F)₂](Anion). *Inorganic Chemistry*, 59(18), 13784–13791. doi: 10.1021/acs.inorgchem.0c02201
- Faulmann, C., Chahine, J., Valade, L., Chastanet, G., Létard, J.-F., and de Caro, D. (2013). Photomagnetic Studies of Spin-Crossover and Photochromic-Based Complexes. *European Journal of Inorganic Chemistry*, 2013(5–6), 1058–1067. doi: <https://doi.org/10.1002/ejic.201201328>
- Habarakada, U., Boonprab, T., Harding, P., S. Murray, K., Phonsri, W., M. Neville, S., Ahmed, M., and J. Harding, D. (2022). Solvent Effects on the Structural and Magnetic Properties of Fe(III) Spin-Crossover Complexes. *Crystal Growth & Design*, 22(8), 4895–4905. doi: 10.1021/acs.cgd.2c00390
- Haddad, M. S., Federer, W. D., Lynch, M. W., and Hendrickson, D. N. (1980). An explanation of unusual properties of spin-crossover ferric complexes. *Journal of the American Chemical Society*, 102(4), 1468–1470. doi: 10.1021/ja00524a065
- Haddad, M. S., Federer, W. D., Lynch, M. W., and Hendrickson, D. N. (1981). Spin-crossover ferric complexes: unusual effects of grinding and doping solids. *Inorganic Chemistry*, 20(1), 131–139. doi: 10.1021/ic50215a029
- Halcrow, M. A. (2011). Structure: function relationships in molecular spin-crossover complexes. *Chem. Soc. Rev.*, 40(7), 4119–4142. doi: 10.1039/C1CS15046D

- Harding, D. J., Harding, P., and Phonsri, W. (2016). Spin crossover in iron(III) complexes. *Coordination Chemistry Reviews*, 313, 38–61.
doi: <https://doi.org/10.1016/j.ccr.2016.01.006>
- Hauser, A. (2013). Spin-Crossover Materials. Properties and Applications. Edited by Malcolm A. Halcrow. *Angewandte Chemie International Edition*, 52(40), 10419.
doi: <https://doi.org/10.1002/anie.201306160>
- Hayami, S., Kawahara, T., Juhasz, G., Kawamura, K., Uehashi, K., Sato, O., and Maeda, Y. (2003). Iron(III) spin transition compound with a large thermal hysteresis. *Journal of Radioanalytical and Nuclear Chemistry*, 255. doi: 10.1023/A:1022503609539
- Jeon, I.-R., Jeannin, O., Clérac, R., Rouzières, M., and Fourmigué, M. (2017). Spin-state modulation of molecular FeIII complexes via inclusion in halogen-bonded supramolecular networks. *Chemical Communications*, 53(36), 4989–4992.
doi: 10.1039/C7CC01943B
- Ketkaew, R., Tantirungrotechai, Y., Harding, P., Chastanet, G., Guionneau, P., Marchivie, M., and Harding, D. J. (2021). OctaDist: a tool for calculating distortion parameters in spin crossover and coordination complexes. *Dalton Trans.*, 50(3), 1086–1096.
doi: 10.1039/D0DT03988H
- Koike, M., Murakami, K., Fujinami, T., Nishi, K., Matsumoto, N., and Sunatsuki, Y. (2013). Syntheses, three types of hydrogen-bonded assembly structures, and magnetic properties of [FeIII(Him)₂(happen)]Y·solvent (Him=imidazole, happen=N,N'-bis(2-hydroxyacetophenylidene)ethylenediamine, Y=BPh₄⁻, CF₃SO₃⁻, PF₆⁻, ClO₄⁻, and BF₄⁻). *Inorganica Chimica Acta*, 399, 185–192.
doi: <https://doi.org/10.1016/j.ica.2013.01.021>
- Martinho, P. N., Martins, F. F., Bandeira, N. A. G., and Calhorda, M. J. (2020). *sustainability Spin Crossover in 3D Metal Centers Binding Halide-Containing Ligands: Magnetism, Structure and Computational Studies*.
doi: 10.3390/su12062512
- Martinho, P. N., Vicente, A. I., Realista, S., Saraiva, M. S., Melato, A. I., Brandão, P., Ferreira, L. P., and De Deus Carvalho, M. (2014). Solution and solid state properties of Fe(III) complexes bearing N-ethyl-N-(2-aminoethyl)salicylaldiminate

- ligands. *Journal of Organometallic Chemistry*, 760, 48–54.
doi: <https://doi.org/10.1016/j.jorganchem.2013.12.028>
- Martins, F. F., Joseph, A., Diogo, H. P., Minas da Piedade, M. E., Ferreira, L. P., Carvalho, M. D., Barroso, S., Romão, M. J., Calhorda, M. J., and Martinho, P. N. (2018). Irreversible Magnetic Behaviour Caused by the Thermosalient Phenomenon in an Iron(III) Spin Crossover Complex. *European Journal of Inorganic Chemistry*, 2018(25), 2976–2983. doi: <https://doi.org/10.1002/ejic.201800605>
- Molčanov, K., and Kojić-Prodić, B. (2019). Towards understanding π -stacking interactions between non-aromatic rings. *IUCrJ*, 6(2), 156–166.
doi: 10.1107/S2052252519000186
- Nihei, M., Shiga, T., Maeda, Y., and Oshio, H. (2007). Spin crossover iron(III) complexes. *Coordination Chemistry Reviews*, 251(21–24), 2606–2621.
doi: 10.1016/j.ccr.2007.08.007
- Phonsri, W., Harding, P., Liu, L., Telfer, S. G., Murray, K. S., Moubaraki, B., Ross, T. M., Jameson, G. N. L., and Harding, D. J. (2017). *Solvent modified spin crossover in an iron(III) complex: phase changes and an exceptionally wide hysteresis t*.
doi: 10.1039/c6sc05317c
- Russell, V., Scudder, M., and Dance, I. (2001). The crystal supramolecularity of metal phenanthroline complexes. *J. Chem. Soc., Dalton Trans.*, 6, 789–799.
doi: 10.1039/B008607J
- Sertphon, D., Harding, D. J., Harding, P., Murray, K. S., Moubaraki, B., Cashion, J. D., and Adams, H. (2013). Anionic Tuning of Spin Crossover in Fe^{III}–Quinolylsalicylal diminate Complexes. *European Journal of Inorganic Chemistry*, 2013(5–6), 788–795. doi: 10.1002/ejic.201201066
- Sheu, C.-F., Chen, S.-M., Lee, G.-H., Liu, Y.-H., Wen, Y.-S., Lee, J.-J., Chuang, Y.-C., and Wang, Y. (2013). Structure and Magnetism of the Iron(III) Spin-Crossover Complex [Fe^{III}{N-ethyl-N-(2-aminoethyl)salicylal diminate}₂][ClO₄]. *European Journal of Inorganic Chemistry*, 2013(5–6), 894–901.
doi: <https://doi.org/10.1002/ejic.201201067>
- Tissot, A., Bertoni, R., Collet, E., Toupet, L., and Boillot, M.-L. (2011). The cooperative spin-state transition of an iron(III) compound [Fe^{III}(3-MeO-SalEen)₂][PF₆]: thermal-

- vs. ultra-fast photo-switching. *Journal of Materials Chemistry*, 21(45), 18347–18353. doi: 10.1039/C1JM14163E
- Tissot, A., Fertey, P., Guillot, R., Briois, V., and Boillot, M.-L. (2014). Structural, Magnetic, and Vibrational Investigations of FeIII Spin-Crossover Compounds [Fe(4-MeO–SalEen)₂]X with X = NO₃[–] and PF₆[–]. *European Journal of Inorganic Chemistry*, 2014(1), 101–109. doi: <https://doi.org/10.1002/ejic.201300960>
- Tsukiashi, A., Nakaya, M., Kobayashi, F., Ohtani, R., Nakamura, M., M. Harrowfield, J., Kim, Y., and Hayami, S. (2018). Intermolecular Interaction Tuning of Spin-Crossover Iron(III) Complexes with Aromatic Counteranions. *Inorganic Chemistry*, 57(5), 2834–2842. doi: 10.1021/acs.inorgchem.7b03126
- van Koningsbruggen, P. J., Maeda, Y., and Oshio, H. (2004). Spin Crossover in Transition Metal Compounds I. In *Iron(III) Spin Crossover Compounds* (Vol. 233, pp. 259–324). Springer-Verlag: Berlin, Heidelberg, New York. doi: 10.1007/b95409
- Vicente, A. I., Joseph, A., Ferreira, L. P., de Deus Carvalho, M., Rodrigues, V. H. N., Duttine, M., Diogo, H. P., da Piedade, M. E., Calhorda, M. J., and Martinho, P. N. (2016). Dynamic spin interchange in a tridentate Fe(III) Schiff-base compound. *Chemical Science*, 7(7), 4251–4258. doi: 10.1039/C5SC04577K

CHAPTER III

MATERIALS AND METHODS

3.1 Experimental

3.1.1 Chemicals

All solvents used were of analytical reagent (AR) grade, and all reactions were carried out under ambient atmospheric conditions. The chemicals were purchased from Sigma-Aldrich or TCI Chemicals and were used without further purification.

3.1.2 Physical measurements

Infrared spectra were recorded using ATR on a Bruker Tensor 27 FT-IR spectrometer with OPUS software, covering the range of 400–4000 cm^{-1} . Electronic spectra were recorded in solution for all complexes in CHCl_3 (0.25 mM) at room temperature on PG Instruments T80+ UV/Vis Spectrometer in the range of 250–900 nm. Elemental analyses were performed using a Eurovector EA3000 analyzer, while electrospray ionization mass spectrometry (ESI-MS) was conducted on a Bruker AmaZon X LCMS mass spectrometer.

3.1.3 X-ray Crystallography

Crystallographic data for complexes **1**, **4** and **5** were carried out with $\text{CuK}\alpha$ radiation using a Rigaku SuperNova (HyPix3000 detector) diffractometer. The data were scaled, integrated, and subjected to absorption correction using CrysAlisPro. The structures were determined using SHELXT and refined through full-matrix least-squares minimization on F^2 using SHELXL. Non-hydrogen atoms were refined anisotropically, whereas hydrogen atom positions were determined geometrically and refined using the riding model. All structural illustrations were created with OLEX2. Complexes **2** and **3** were collected using a Bruker D8 VENTURE diffractometer with $\text{MoK}\alpha$ radiation ($\lambda = 0.71073 \text{ \AA}$). Unit cell parameters were determined, and data collection was

performed using APEX4. The structures were solved by intrinsic phasing with SHELXT and refined.

Powder X-ray diffraction data for the precipitates were obtained using a PANalytical X'Pert PRO MPD diffractometer equipped with Bragg-Brentano geometry, Cu-K α 1,2 radiation ($\lambda = 1.54184 \text{ \AA}$), and a graphite backscattering monochromator. Standard Si sample holders were used, and the samples were finely ground before data collection over a $2\theta = 0-50^\circ$. Le Bail and Rietveld refinements were conducted using JANA2020 (Petříček et al., 2023).

3.1.4 Hirshfeld surface analysis

The Hirshfeld surface properties of complexes **1-5** were analyzed using Crystal Explorer 17. The crystal structures were imported from CIF files, and high-resolution Hirshfeld surfaces were generated, mapped with the d_{norm} and shape index functions. Additionally, 2D fingerprint plots were created using the same software (Spackman et al., 2021).

3.1.5 Magnetic susceptibility

Magnetic susceptibility measurements were performed using a Quantum Design MPMS 5 SQUID magnetometer under an applied field of 1–2 T over a temperature range of 10–300 K for samples **1**, **2**, and **5**, and 10–380 K for samples **3** and **4**. Powdered or polycrystalline samples were placed in gel capsules, ensuring sufficient thermal equilibration at each temperature. Samples **6-10** were analyzed using a Quantum Design MPMS 3 SQUID magnetometer, with measurements conducted between 1.8–300 K or 1.8–400 K under an applied field of 1000 Oe. These samples were loaded into plastic caps for measurement.

3.1.6 Electrochemical measurements

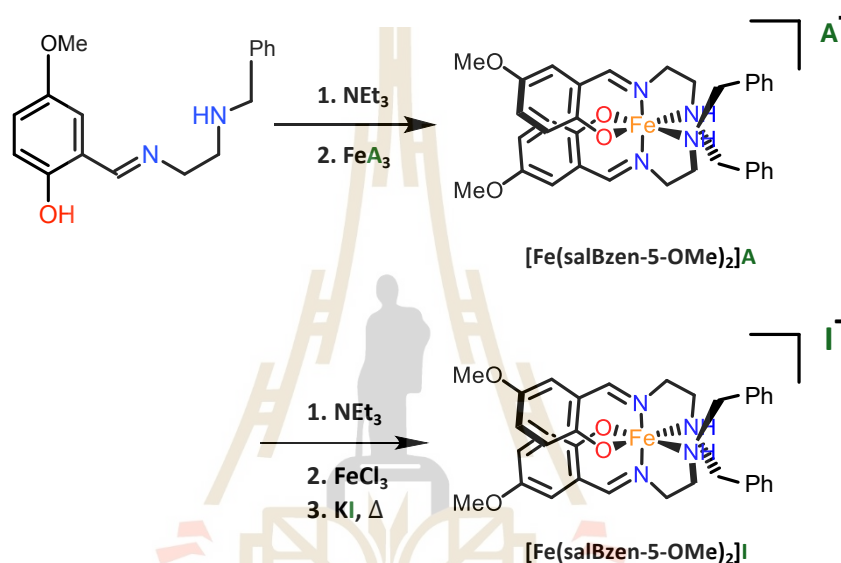
Electrochemical studies were carried out using a PalmSens4 in conjunction with a three-electrode cell consisting of a working electrode (2.0 mm diameter platinum disc), a counter electrode (platinum wire), and a reference electrode ([Ag/AgCl of LiCl 0.01 M in EtOH]). Solutions of the test compound ($5 \times 10^{-4} \text{ mol dm}^{-3}$) were prepared in CH_2Cl_2 , which had been dried over CaH_2 . A supporting electrolyte, $[\text{N-}n\text{Bu}_4][\text{PF}_6]$ (0.1 mol dm^{-3}), was used. Under these conditions, the E°

value for the one-electron oxidation and reduction of $[\text{Fe}(\eta\text{-C}_5\text{H}_5)_2]$, which was added to the test solution for internal calibration, was measured at 0.52 V.

3.2 Synthesis of Fe(III) complexes

3.2.1 Synthesis of $[\text{Fe}(\text{salBzen-5-OMe})_2]\text{A}$ complexes

The synthesis of **1-5** is shown in Scheme 3.1.



Scheme 3.1 Synthesis of $[\text{Fe}(\text{salBzen-5-OMe})_2]\text{A}$ complexes.

3.2.1.1 Synthesis of $[\text{Fe}(\text{salBzen-5-OMe})_2]\text{Cl}$ **1**

Firstly, *HsalBzen-5-OMe* was prepared by dissolving 2-hydroxy-5-methoxybenzaldehyde (0.8 mmol, 0.122 g) in ethanol (5 mL) in the round bottom flask then N-benzylethylenediamine (0.8 mmol, 120.2 μL) was added causing the solution to become a pale yellow. Then triethylamine 111 μL was added for deprotonation. In a separate vial, FeCl₃ (0.0648 g, 0.4 mmol) was dissolved in EtOH (3 mL). The bright orange solution was added dropwise into the *HsalBzen-5-OMe* ligand solution. The deep blue mixture was stirred for 3 hours. The crude was then reduced to approximately 2 mL *in vacuo* and precipitated with water (30 mL). The residue was filtered, washed with water, and dried in air. **1** was collected as black crystals after recrystallization by layering hexane on top of a CH₂Cl₂ solution of the complex (4:1

ratio of CH_2Cl_2 :hexane) (0.124 g, 47%). Elemental analysis: calcd (found) for $\text{C}_{34}\text{H}_{38}\text{FeClN}_4\text{O}_4$: C, 62.06 (61.92); H, 5.82 (5.80); N, 8.51 (8.54).

3.2.1.2 Synthesis of $[\text{Fe}(\text{salBzen-5-OMe})_2]\text{Br}$ **2**

2 was synthesized in a similar method to **1** using FeBr_3 (0.120 g, 0.4 mmol) instead of FeCl_3 . Recrystallization by layering hexane on top of a CH_2Cl_2 solution of the complex (4:1 ratio of CH_2Cl_2 :hexane) yields black crystals of **2** (0.182 g, 64%). Elemental analysis: calcd (found) for $\text{C}_{34}\text{H}_{38}\text{FeBrN}_4\text{O}_4$: C, 58.14 (57.66); H, 5.45 (5.39); N, 7.98 (7.97).

3.2.1.3 Synthesis of $[\text{Fe}(\text{salBzen-5-OMe})_2]\text{I}$ **3**

3 was synthesized via post-complexation anionic exchange from FeCl_3 (0.4 mmol, 0.0646 g) and was dissolved in EtOH (3 mL) to give a bright yellow solution to which the ligand solution was added. The solution immediately turned black and THF (4 mL) was added to improve solubility and a solution of KI (1.2 mmol, 0.1996 mg) in EtOH:H₂O (4 mL:1 mL) was added. The flask was heated at 60 °C overnight. After anionic exchange, the reaction mixture was allowed to cool to room temperature and reduced to approximately 2 mL *in vacuo*. Water (30 mL) was added to precipitate the product. The residue was filtered, washed with water, and dried in air. **3** was collected as black crystals after recrystallization by layering hexane on top of a CH_2Cl_2 solution of the complex (4:1 ratio of CH_2Cl_2 :hexane) (0.177 g, 59%). Elemental analysis: calcd (found) for $\text{C}_{34}\text{H}_{38}\text{FeIN}_4\text{O}_4$: C, 54.49 (54.49); H, 5.11 (5.08); N, 7.48 (7.59).

3.2.1.4 Synthesis of $[\text{Fe}(\text{salBzen-5-OMe})_2]\text{NO}_3$ **4**

4 was synthesized in a similar method to **1** using $\text{Fe}(\text{NO}_3)_3$ (0.162 g, 0.4 mmol) instead of FeCl_3 . Recrystallization by layering hexane on top of a CH_2Cl_2 solution of the complex (4:1 ratio of CH_2Cl_2 :hexane) yields black crystals of **4** (0.155 g, 57%). Elemental analysis: calcd (found) for $\text{C}_{34}\text{H}_{38}\text{FeN}_5\text{O}_7$: C, 59.66 (59.08); H, 5.60 (5.52); N, 10.23 (10.23).

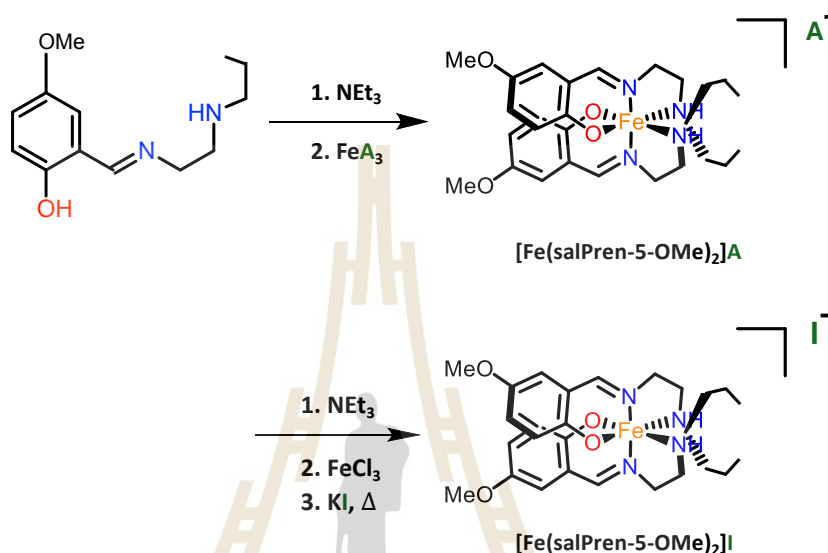
3.2.1.5 Synthesis of $[\text{Fe}(\text{salBzen-5-OMe})_2]\text{ClO}_4$ **5**

5 was synthesized in a similar method to **1** using $\text{Fe}(\text{ClO}_4)_3$ (0.143 g, 0.4 mmol) instead of FeCl_3 . Recrystallization by layering hexane on top of a CH_2Cl_2 solution of the complex (4:1 ratio of CH_2Cl_2 :hexane) yields black crystals of **5**

(0.119 g, 41%). Elemental analysis: calcd (found) for $C_{34}H_{38}FeClN_4O_8$: C, 56.56 (56.48); H, 5.31 (5.26); N, 7.76 (7.81).

3.2.2 Synthesis of $[Fe(salPren-5-OMe)_2]A$ complexes

The synthesis of **6-10** is shown in Scheme 3.2.



Scheme 3.2 Synthesis of $[Fe(salPren-5-OMe)_2]A$ complexes.

3.2.2.1 Synthesis of $[Fe(salPren-5-OMe)_2]Cl$ **6**

Firstly, HsalPren-5-OMe was prepared by dissolving 2-hydroxy-5-methoxybenzaldehyde (0.8 mmol, 0.122 g) in ethanol (5 mL) in the round bottom flask then N-propylethylenediamine (0.8 mmol, 98.6 μ L) was added causing the solution to become a pale orange. Then triethylamine 111 μ L was added for deprotonation. In a separate vial, FeCl₃ (0.0648 g, 0.4 mmol) was dissolved in EtOH (3 mL). The bright orange solution was added dropwise into the HsalPren-5-OMe ligand solution. The deep blue mixture was stirred for 3 hours. The crude was then reduced to approximately 2 mL *in vacuo* and precipitated with water (30 mL). The residue was filtered, washed with water, and dried in air. **6** was collected as black microcrystals after slowly reducing from 1:2 CH₂Cl₂:hexane (0.130 g, 58%). Elemental analysis: calcd (found) for $C_{26}H_{38}FeClN_4O_4$: C, 55.58 (55.22); H, 6.82 (6.84); N, 9.97 (9.91).

3.2.2.2 Synthesis of $[\text{Fe}(\text{salPren-5-OMe})_2]\text{Br}$ **7**

7 was synthesized in a similar method to **6** using FeBr_3 (0.120 g, 0.4 mmol) instead of FeCl_3 . Recrystallization after slowly reducing from 1:2 CH_2Cl_2 :hexane yields black microcrystals of **7** (0.179 g, 73%). Elemental analysis: calcd (found) for $\text{C}_{26}\text{H}_{38}\text{FeBrN}_4\text{O}_4$: C, 51.50 (51.12); H, 6.32 (6.35); N, 9.24 (9.17).

3.2.2.3 Synthesis of $[\text{Fe}(\text{salPren-5-OMe})_2]\text{I}$ **8**

8 was synthesized via post-complexation anionic exchange from FeCl_3 (0.4 mmol, 0.0649 g) and was dissolved in EtOH (3 mL) to give a bright yellow solution to which the ligand solution was added. The solution immediately turned black and THF (4 mL) was added to improve solubility and a solution of KI (1.2 mmol, 0.2012 mg) in EtOH:H₂O (4 mL:1 mL) was added. The flask was heated at 60 °C overnight. After anionic exchange, the reaction mixture was allowed to cool to room temperature and reduced to approximately 2 mL *in vacuo*. Water (30 mL) was added to precipitate the product. The residue was filtered, washed with water, and dried in air. **8** was collected as black microcrystals after slowly reducing from 1:2 CH_2Cl_2 :hexane (0.193 g, 76%). Elemental analysis: calcd (found) for $\text{C}_{26}\text{H}_{38}\text{FeIN}_4\text{O}_4$: C, 47.80 (47.47); H, 5.86 (5.90); N, 8.58 (8.52).

3.2.2.4 Synthesis of $[\text{Fe}(\text{salPren-5-OMe})_2]\text{NO}_3$ **9**

9 was synthesized in a similar method to **6** using $\text{Fe}(\text{NO}_3)_3$ (0.162 g, 0.4 mmol) instead of FeCl_3 . Recrystallization after slowly reducing from 1:2 CH_2Cl_2 :hexane yields black microcrystals of **9** (0.161 g, 68%). Elemental analysis: calcd (found) for $\text{C}_{26}\text{H}_{38}\text{FeN}_5\text{O}_7$: C, 53.07 (52.67); H, 6.51 (6.54); N, 11.90 (11.81).

3.2.2.5 Synthesis of $[\text{Fe}(\text{salPren-5-OMe})_2]\text{ClO}_4$ **10**

10 was synthesized in a similar method to **6** using $\text{Fe}(\text{ClO}_4)_3$ (0.143 g, 0.4 mmol) instead of FeCl_3 . Recrystallization after slowly reducing from 1:2 CH_2Cl_2 :hexane yields black microcrystals of **10** (0.182 g, 69%). Elemental analysis: calcd (found) for $\text{C}_{26}\text{H}_{38}\text{FeN}_5\text{O}_7$: C, 49.89 (49.54); H, 6.12 (6.16); N, 8.95 (8.89).

3.3 References

Petříček, V., Palatinus, L., Plášil, J., and Dušek, M. (2023). Jana2020 – a new version of the crystallographic computing system Jana. *238*(7–8), 271–282.

doi: doi:10.1515/zkri-2023-0005

Spackman, P. R., Turner, M. J., McKinnon, J. J., Wolff, S. K., Grimwood, D. J., Jayatilaka, D., and Spackman, M. A. (2021). CrystalExplorer: a program for Hirshfeld surface analysis, visualization and quantitative analysis of molecular crystals. *Journal of Applied Crystallography*, *54*(3), 1006–1011. doi: 10.1107/S1600576721002910



CHAPTER IV

RESULTS AND DISCUSSION

4.1 Synthesis and basic characterization of Fe(III) Schiff base complexes

4.1.1 Spectroscopic study of $[\text{Fe}(\text{salRen-5-OMe})_2]\text{A}$

The infrared spectra of $[\text{Fe}(\text{salBzen-5-OMe})_2]\text{A}$ and $[\text{Fe}(\text{salPren-5-OMe})_2]\text{A}$ complexes are shown in Figures 4.1 and 4.2, with the corresponding IR spectroscopic data shown in Table 4.1. All complexes in this series exhibit similar spectra with the same key bands. The C=N stretches, corresponding to the imine groups in salBzen-5-OMe and salPren-5-OMe, appear around $1620\text{--}1631\text{ cm}^{-1}$. The C=C stretches of the aromatic ring are observed in the range of $1463\text{--}1544\text{ cm}^{-1}$, while N-H stretches are detected between $3087\text{--}3245\text{ cm}^{-1}$. The benzyl group is more electron-withdrawing than the propyl group. This electron-donating effect of the propyl group reduces the strength of the C=C bonds in the aromatic ring and the C=N bonds in the complex. Consequently, the IR peaks of $[\text{Fe}(\text{salPren-5-OMe})_2]\text{A}$ **6-10** are comparatively lower in wavenumber than those of the $[\text{Fe}(\text{salBzen-5-OMe})_2]\text{A}$ **1-5** complexes. Additionally, the complexes show characteristic anion stretches for NO_3^- and ClO_4^- at $1290\text{--}1382$ and $1085\text{--}1112\text{ cm}^{-1}$, respectively (Díaz-Torres et al., 2020). The IR spectra are fully consistent with the proposed structures. However, complex **6** exhibits a broad band around 3409 cm^{-1} , which is attributed to O-H vibrational stretches, suggesting possible water absorption by the complex.

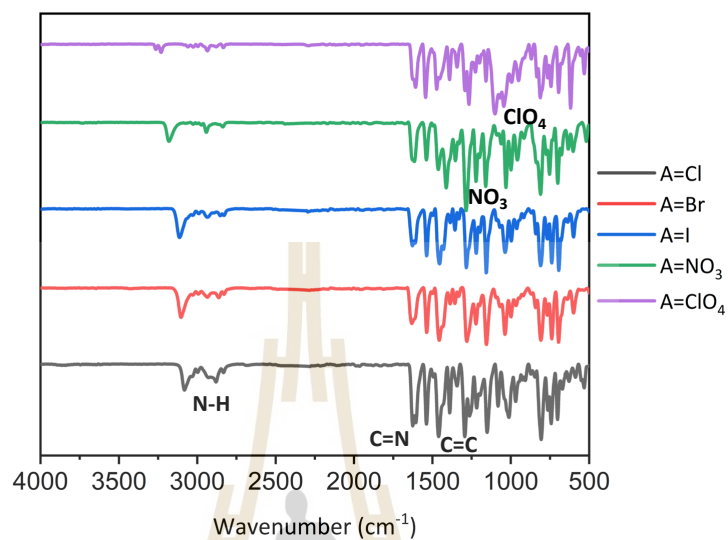


Figure 4.1 IR spectra of $[\text{Fe}(\text{salBzen-5-OMe})_2]\text{A}$ complexes.

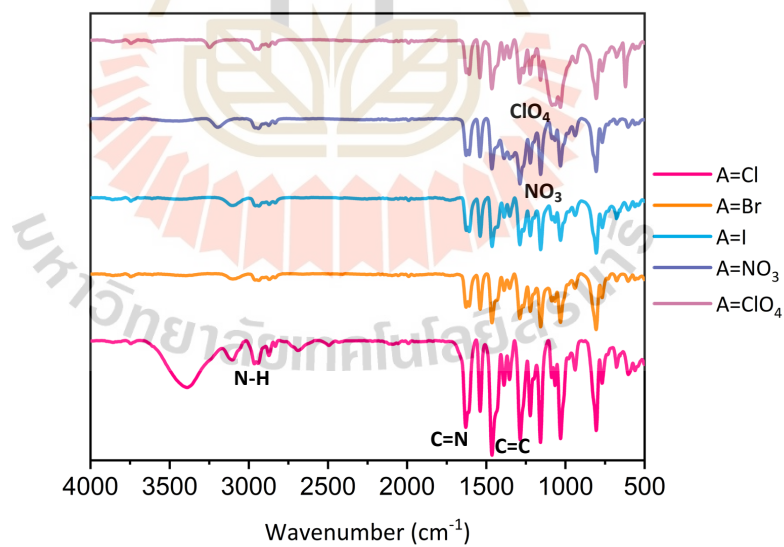


Figure 4.2 IR spectra of $[\text{Fe}(\text{salPen-5-OMe})_2]\text{A}$ complexes.

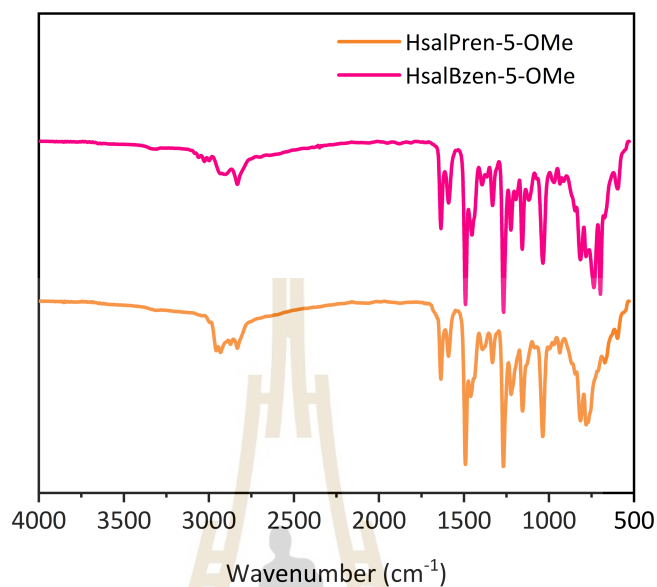


Figure 4.3 IR spectra of HsalPren-5-OMe and HsalBzen-5-OMe ligands.

Additionally, the infrared spectra of HsalPren-5-OMe and HsalBzen-5-OMe ligands exhibit characteristic vibrational bands corresponding to their functional groups (Figure 4.3). Both ligands show a broad absorption band in the region of 3000 cm⁻¹, which can be attributed to C-H stretching vibrations. A strong absorption band near 1500 cm⁻¹ is associated with aromatic C=C stretching, while the C=N stretching vibrations of the imine groups in HsalPren-5-OMe and HsalBzen-5-OMe appear at approximately 1630 cm⁻¹. These spectral differences highlight the structural variations between the two ligands and their electronic effects.

Table 4.1 IR spectroscopic data of [Fe(salRen-5-OMe)₂]A complexes.

Complexes	Wavenumber (cm ⁻¹)			
	$\nu_{\text{N-H}}$	$\nu_{\text{C=N}}$	$\nu_{\text{C=C}}$	ν_{anion}
[Fe(salBzen-5-OMe) ₂]Cl 1	3087	1629	1544	-
[Fe(salBzen-5-OMe) ₂]Br 2	3105	1629	1537	-
[Fe(salBzen-5-OMe) ₂]I 3	3112	1623	1535	-
[Fe(salBzen-5-OMe) ₂]NO ₃ 4	3178	1631	1542	1382
[Fe(salBzen-5-OMe) ₂]ClO ₄ 5	3232	1629	1542	1112
[Fe(salPren-5-OMe) ₂]Cl 6	3107	1627	1463	-
[Fe(salPren-5-OMe) ₂]Br 7	3190	1620	1463	-
[Fe(salPren-5-OMe) ₂]I 8	3097	1620	1463	-
[Fe(salPren-5-OMe) ₂]NO ₃ 9	3190	1620	1463	1290
[Fe(salPren-5-OMe) ₂]ClO ₄ 10	3245	1622	1463	1085

The UV-Vis spectra of [Fe(salBzen-5-OMe)₂]A and [Fe(salPren-5-OMe)₂]A complexes in chloroform are shown in Figures 4.4-4.5. All complexes exhibit a prominent absorption band in the UV region, below 400 nm, is assigned to a charge transfer and intraligand π - π^* transitions arising from the aromatic ring of the salBzen and salPren ligands. In the visible region, two additional peaks are observed around 600 nm and 730 nm, likely corresponding to ligand-to-metal charge transfer (LMCT) bands from a phenolate $p\pi$ orbital to an iron(III) $d\pi$ orbital, as shown in Table 4.2. The λ_{max} positions are consistent with those observed in high spin Fe(III) complexes, such as [Fe(salRen)₂]⁺ (Petty et al., 1978). These spectral values are consistent with those reported for various Fe(III) complexes, including [Fe(salMeen-5-Br)₂]ClO₄, [Fe(salMeen-5-Cl)₂]ClO₄ (Al-Azzani et al., 2020), [Fe(hapMen)₂]ClO₄, [Fe(hapEen)₂]ClO₄ (Shongwe et al., 2012), and [Fe(X-salMeen)₂]PF₆ (Petty et al., 1978). In each case, the lower-energy band is indicative of the low-spin (LS) state, while the higher-energy band is characteristic of the high-spin (HS) state (Tweedle et al., 1976).

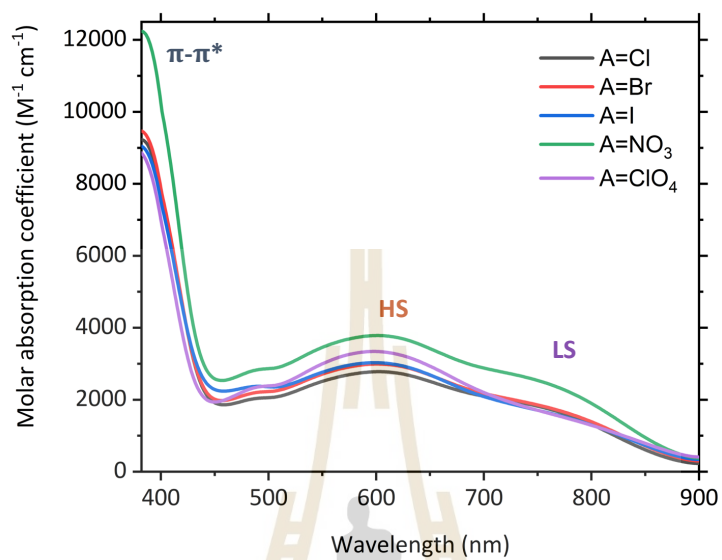


Figure 4.4 UV-Vis spectra of $[\text{Fe}(\text{salBen-5-OMe})_2]\text{A}$ complexes.

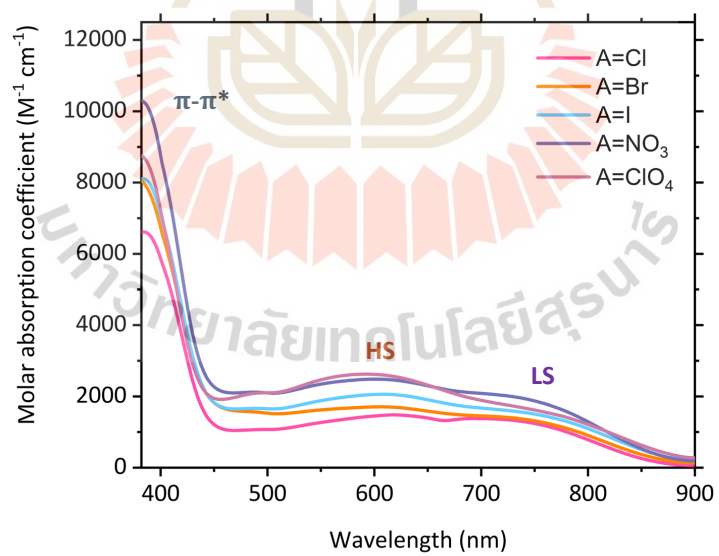


Figure 4.5 UV-Vis spectra of $[\text{Fe}(\text{salPren-5-OMe})_2]\text{A}$ complexes.

Table 4.2 UV-vis spectroscopic data of [Fe(salRen-5-OMe)₂]A complexes.

Complexes	λ_{\max} (nm), ϵ (M ⁻¹ cm ⁻¹)			
	π - π^*	HS-LMCT	LS-LMCT	ϵ Ratio (HS/LS)
[Fe(salBzen-5-OMe) ₂]Cl 1	385(7340)	606(2711)	738(1859)	1.46
[Fe(salBzen-5-OMe) ₂]Br 2	389(7310)	605(2922)	739(1875)	1.56
[Fe(salBzen-5-OMe) ₂]I 3	391(7626)	606(3127)	737(1866)	1.67
[Fe(salBzen-5-OMe) ₂]NO ₃ 4	384(7821)	601(3537)	733(2312)	1.53
[Fe(salBzen-5-OMe) ₂]ClO ₄ 5	380(7763)	604(4156)	732(2324)	1.79
[Fe(salPren-5-OMe) ₂]Cl 6	390(6382)	596(1604)	731(1432)	1.12
[Fe(salPren-5-OMe) ₂]Br 7	387(6856)	597(1693)	729(1357)	1.25
[Fe(salPren-5-OMe) ₂]I 8	390(6977)	599(2051)	727(1601)	1.28
[Fe(salPren-5-OMe) ₂]NO ₃ 9	390(7607)	604(2441)	735(1914)	1.27
[Fe(salPren-5-OMe) ₂]ClO ₄ 10	388(7130)	605(2536)	732(1678)	1.51

The observed differences in the ϵ (HS/LS) ratios between the two series are consistent with variations in ligand field strength. The salPren-5-OMe ligand appears to induce a stronger ligand field, favoring the LS state, while the salBzen-5-OMe ligand supports a weaker ligand field, favoring the HS state. These differences might arise from electronic or steric effects introduced by the structural differences between salBzen and salPren ligands. However, the anion also impacts these ratios with the complexes increasingly LS as the N-H...anion interactions become stronger. The order of the anions is consistent with the Hofmeister series (Kang et al., 2020).

The elemental analysis and mass spectrometry data for complexes **1-10** confirmed their purity, as detailed in the experimental section and supporting information. It was observed that [Fe(salPren-5-OMe)₂]A **6-10** contained 0.25 mol of H₂O, likely due to residual solvent from the synthesis process. Unfortunately, for compound **6**, the mass spectrometry data revealed a discrepancy between the molecular weight of the salPren ligand and the expected molecular weight of the complex. This discrepancy may result

from water absorption by the complex, which was observed as an oil-like sample. Despite extensive efforts to recrystallize the salPren series, no crystals suitable for SC-XRD were obtained. Furthermore, the powder X-ray diffraction (PXRD) data for these samples were broad and nearly amorphous. Although reasonable PXRD patterns were obtained for complexes **6–10** from extremely fresh samples, the difficulty in crystallization persisted, and most samples used for bulk measurements remained amorphous as shown in supporting information. In contrast, the $[\text{Fe}(\text{salBzen-5-OMe})_2]\text{A}$ (**1–5**) series did not contain any solvent. All complexes in this series successfully recrystallized, allowing for more definitive structural analysis. Additionally, the PXRD patterns of each complex in salBzen series align with their corresponding simulated patterns generated using Jana 2020 as shown in supporting information.

4.2 Structural studies of Fe(III) Schiff base complexes

Crystals of $[\text{Fe}(\text{salBzen-5-OMe})_2]\text{Cl}$ (**1**), $[\text{Fe}(\text{salBzen-5-OMe})_2]\text{Br}$ (**2**) and $[\text{Fe}(\text{salBzen-5-OMe})_2]\text{I}$ (**3**) were grown from $\text{CH}_2\text{Cl}_2/\text{hexane}$. While crystals of $[\text{Fe}(\text{salBzen-5-OMe})_2]\text{NO}_3$ (**4**) and $[\text{Fe}(\text{salBzen-5-OMe})_2]\text{ClO}_4$ (**5**) were grown from $\text{CHCl}_3/\text{hexane}$ to give black blocks. They crystallize in monoclinic $P2_1/n$ or $P2_1/c$ (**1**, **4** and **5**), monoclinic $P2_1/n$ (**2**) or tetragonal $P4_32_12$ (**3**) phases. The structures of **1**, **3** and **4** were determined at 150 and 295 K, while **2** was recorded at 295 K only. Efforts to determine the structure of **2** at low temperature were unsuccessful because of crystal cracking. In contrast, The unique magnetic characteristics of **5** (vide infra) motivated us to examine its structures at 30, 100 and 295 K. The Fe-ligand bond lengths and octahedral distortion parameters, calculated using OctaDist (Ketkaew et al., 2021), and the crystallographic data and refinement parameters are provided in Tables 4.3-4.6. In all cases, the Fe(III) center is six-coordinate, bonded to four nitrogen and two oxygen atoms from two meridional salBzen ligands, with the oxygen atoms positioned cis to each other, resulting in an octahedral coordination sphere (Figure 4.6-4.10). The anion is stabilized by N-H...anion interactions, with distances varying between 2.1 and 2.6 Å, varying with the anion size. Interestingly, in **1** symmetry-breaking

is observed, showing one independent HS Fe(III) centre at high temperature (295 K), and two centres (Fe1 and Fe2) at low temperature (150 K) that remain in a [HS-HS] state. The Fe-N/O bond lengths in **1** and **2** are in the ranges 2.161–2.180 Å and 1.902–1.921 Å, respectively, and are comparable to the corresponding distances observed for the HS Fe(III) center in [Fe(naphBzen)₂] found in the [LS-HS] state at 100 K and [HS-HS] state at 120 K (Boonprab et al., 2019). Even at low temperature, **1** exhibits no significant variation in bond distances. While Fe1 is much more distorted than Fe2, this suggests that **1** does not exhibit SCO down to 150 K. In contrast, [Fe(salEen-Br)₂]Cl·0.5H₂O also features two independent centers; however, at 150 K, one adopts the HS state while the other remains in the LS state (Cardoso et al., 2015). This suggests that salBzen-5-OMe displays a weaker ligand field than salEen-Br with the same anion. In contrast, the Fe N/O bond lengths for **3** and **4** are on average between 1.990–2.003 Å and 1.858–1.870 Å respectively, which is characteristic of LS Fe(III) at 150 K and 295 K, nevertheless, at 295 K the value remains slightly lower than anticipated for a fully HS state, suggesting an incomplete and gradual SCO within the examined temperature range. Interestingly, for **5** the Fe-O bond length remains relatively unchanged between 30 K and 100 K, indicating minimal structural rearrangement around the Fe-O coordination sphere in this temperature range. In contrast, the Fe-N bond lengths show a significant increase during this interval, reflecting notable changes in the Fe-N bond lengths (Figure 4.11). This behavior aligns with the complex's predominant HS state, even at 30 K. The elongation of Fe-N bonds corresponds to the HS state, while the stable Fe-O bond length highlights the structural rigidity of the Fe-O coordination. This structural observation supports the magnetic data, confirming the complex's strong preference for the HS state over the examined temperature range.

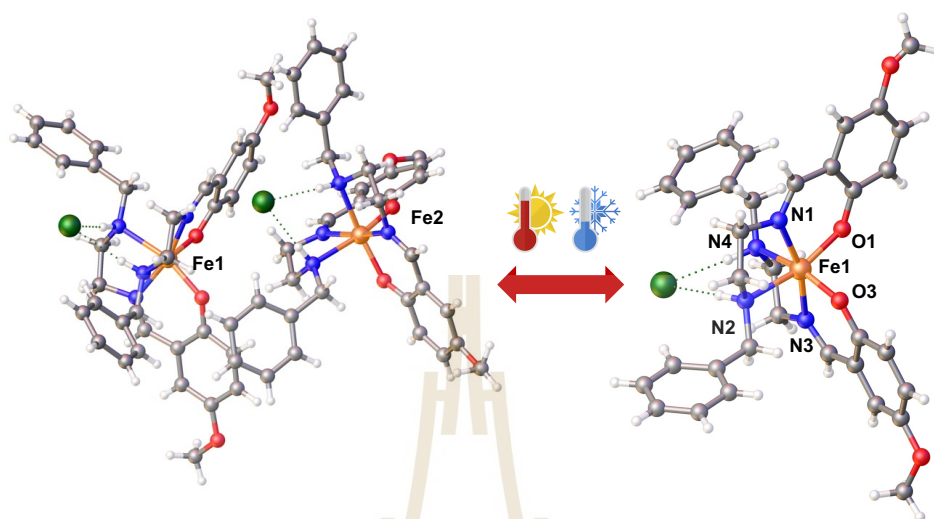


Figure 4.6 View of the asymmetric unit of $[\text{Fe}(\text{salBzen-5-OMe})_2]\text{Cl}$ (**1**) at 150 K (left) and 295 K (right).

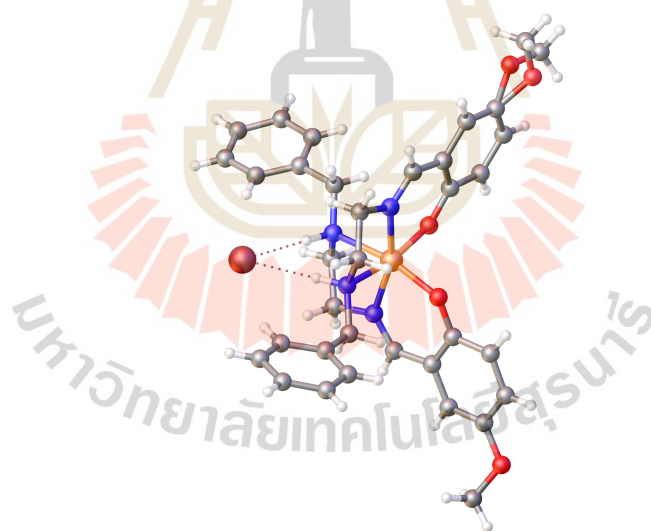


Figure 4.7 View of the asymmetric unit of $[\text{Fe}(\text{salBzen-5-OMe})_2]\text{Br}$ (**2**) at 295 K.

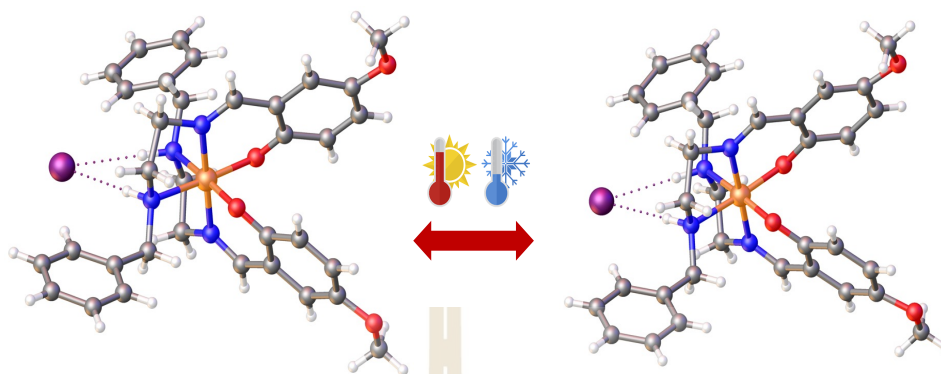


Figure 4.8 View of the asymmetric unit of $[\text{Fe}(\text{salBzen-5-OMe})_2]\text{I}$ (**3**) at 150 K (left) and 295 K (right).

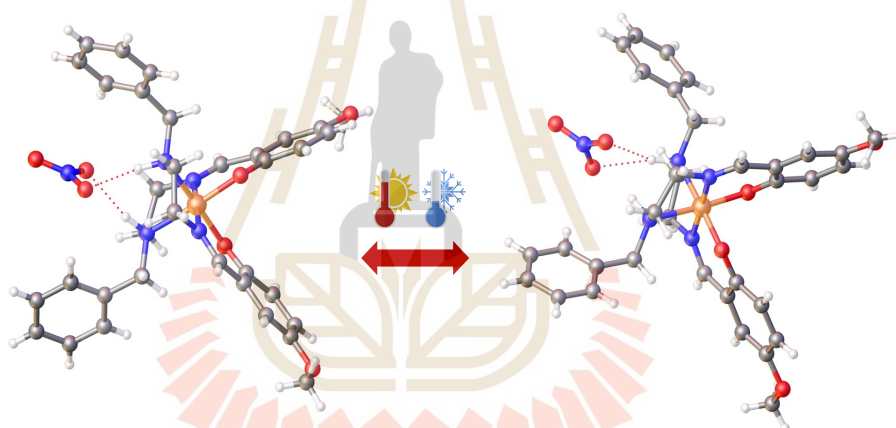


Figure 4.9 View of the asymmetric unit of $[\text{Fe}(\text{salBzen-5-OMe})_2]\text{NO}_3$ (**4**) at 150 K (left) and 295 K (right).

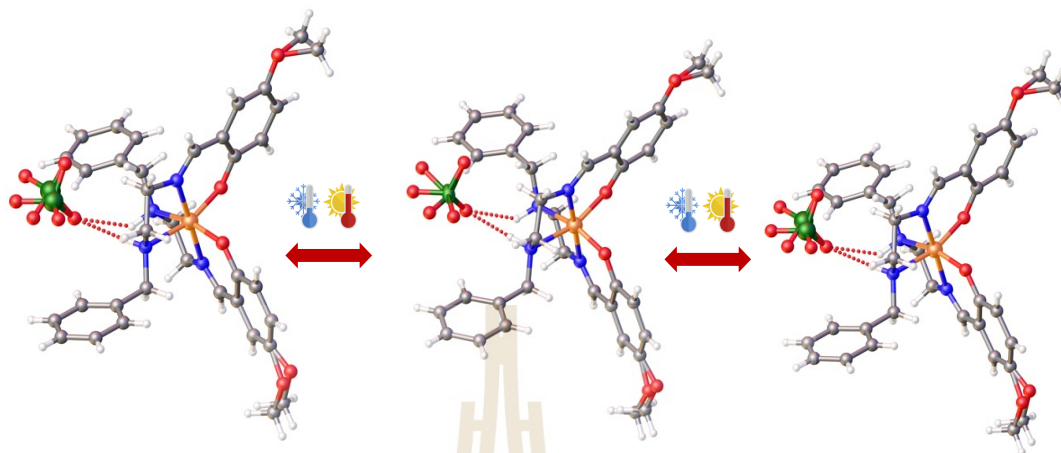


Figure 4.10 View of the asymmetric unit of $[\text{Fe}(\text{salBzen-5-OMe})_2]\text{ClO}_4$ (**5**) at 30 K (left), 100 K (middle) and 290 K (right).

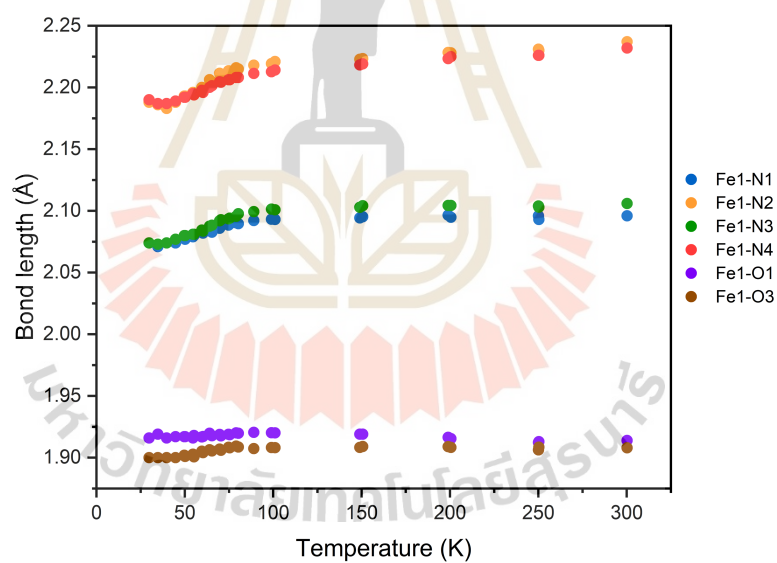


Figure 4.11 Fe-N/O bond lengths (Å) of $[\text{Fe}(\text{salBzen-5-OMe})_2]\text{ClO}_4$ (**5**) at 30-300 K.

Table 4.3 Selected Fe-N/O bond lengths (Å) and octahedral distortion parameters (°) of **1–3** complexes.

Fe-N/O bond distance/Å	1		2		3	
T/K	150	295	295	295	150	295
Fe1-O1	1.914(18)	1.914(2)	1.904(3)	1.864(6)	1.858(6)	1.858(6)
Fe1-O3	1.930(18)	1.915(2)	1.899(3)	1.864(6)	1.858(6)	1.858(6)
Fe1-O _{ave}	1.920(18)	1.914(2)	1.902(3)	1.864(6)	1.858(6)	1.858(6)
Fe1-N1	2.125(2)	2.108(2)	2.087(3)	1.914(7)	1.925(7)	1.925(7)
Fe1-N2	2.217(2)	2.243(2)	2.230(3)	2.065(6)	2.082(7)	2.082(7)
Fe1-N3	2.121(2)	2.109(2)	2.085(3)	1.914(7)	1.925(7)	1.925(7)
Fe1-N4	2.258(2)	2.237(2)	2.240(3)	2.065(6)	2.082(7)	2.082(7)
Fe1-N _{ave}	2.180(2)	2.174(2)	2.161(3)	1.990(7)	2.003(7)	2.003(7)
Fe2-O5	1.918(18)					
Fe2-O7	1.923(18)					
Fe2-O _{ave}	1.921(18)					
Fe2-N5	2.107(2)					
Fe2-N6	2.235(2)					
Fe2-N7	2.108(2)					
Fe2-N8	2.232(2)					
Fe2-N _{ave}	2.171(2)					

Table 4.3 Selected Fe-N/O bond lengths (Å) and octahedral distortion parameters (°) of **1–3** complexes (Continued).

Σ^a Fe1, Fe2	75, 67	68	67	42	41
Θ^b Fe1, Fe2	294, 245	270	272	125	129

Table 4.4 Selected Fe-N/O bond lengths (Å) and octahedral distortion parameters (°) of **4** and **5** complexes.

Fe-N/O bond distance/Å	4		5	
	150	295	30	295
T/K				
Fe1-O1	1.873(2)	1.864(2)	1.916(3)	1.908(2)
Fe1-O3	1.867(2)	1.870(2)	1.900(3)	1.910(2)
Fe1-O _{ave}	1.87(2)	1.86(2)	1.908(3)	1.90(2)
Fe1-N1	1.931(3)	1.931(2)	2.074(3)	2.098(2)
Fe1-N2	2.053(3)	2.070(2)	2.188(3)	2.232(3)
Fe1-N3	1.933(3)	1.932(2)	2.074(3)	2.101(2)
Fe1-N4	2.060(3)	2.056(2)	2.190(3)	2.230(3)
Fe1-N _{ave}	1.99(3)	1.99(2)	2.131(3)	2.16(3)
Σ^a Fe1	44	44	68	76
Θ^b Fe1	128	122	252	270

^a See ref. (Hayami et al., 2000) for a definition. ^b See ref. (McCusker et al., 1996) for a definition

Table 4.5 Crystallographic data and refinement parameters for **1–3** complexes.

	1		2	3
Formula	$C_{34}H_{38}FeClN_4O_4$		$C_{34}H_{38}FeBrN_4O_4$	$C_{34}H_{38}FeIN_4O_4$
T (K)	150	295	295	295
MW	657.99		702.44	749.44
Radiation	CuK α		MoK α	MoK α
λ (Å)	1.54184		1.54184	1.54184
Crystal system	Monoclinic		Monoclinic	Tetragonal
Space group	P2 ₁ /c	P2 ₁ /n	P2 ₁ /n	P4 ₃ 2 ₁ 2
a (Å)	15.2305(1)	10.8769(2)	10.8893(4)	14.4120(3)
b (Å)	26.9521(2)	27.1935(4)	26.6396(9)	14.4120(3)
c (Å)	15.5275(1)	11.0607(2)	11.2389(4)	15.9501(5)
α (°)	90	90	90	90
β (°)	91.909(10)	91.7580(10)	91.901(3)	90
γ (°)	90	90	90	90
Cell volume (Å³)	6370.41(8)	3270.00(10)	3258.5(2)	3312.93(17)
Z	8	4	4	4
μ (mm⁻¹)	4.926	4.796	1.732	1.430
				1.403

Table 4.5 Crystallographic data and refinement parameters for **1–3** complexes (Continued).

Reflections collected	36337	18478	76698	30245	26876
Independent reflections, R_{int}	11650, 0.0646	5975, 0.0415	7549, 0.0431	3369, 0.0471	2966, 0.0451
R -Factor (%), wR_2 (%)	5.08, 14.46	4.86, 14.68	5.60, 13.94	5.49, 17.25	5.39, 17.00

Table 4.6 Crystallographic data and refinement parameters for **4** and **5** complexes.

	4		5	
Formula	$\text{C}_{34}\text{H}_{38}\text{FeN}_5\text{O}_7$		$\text{C}_{34}\text{H}_{38}\text{FeClN}_4\text{O}_8$	
T (K)	150	295	30	295
MW	684.54		721.98	
Radiation	$\text{CuK}\alpha$		$\text{MoK}\alpha$	
λ (Å)	1.54184		1.54184	
Crystal system	Monoclinic		Monoclinic	
Space group	$P2_1/c$		$P2_1/c$	
a (Å)	12.0908(4)	12.2018(2)	24.1980(9)	24.3441(6)
b (Å)	14.2947(4)	24.2085(2)	13.2518(6)	13.3372(2)
c (Å)	18.9379(6)	19.4811(3)	10.5331(5)	10.5371(3)
				10.6821(2)

Table 4.6 Crystallographic data and refinement parameters for **4** and **5** complexes (Continued).

α (°)	90	90	90	90
β (°)	99.609(3)	99.366(2)	98.553(4)	98.702(2)
γ (°)	90	90	90	90
Cell volume (Å ³)	3227.20(18)	3332.40(9)	3340.1(3)	3381.82(14)
Z	4	4	4	4
μ (mm ⁻¹)	4.223	4.090	0.589	1.418
Reflections collected	16041	19107	50157	17483
Independent reflections, R_{int}	5860, 0.0484	6101, 0.0471	8265, 0.0749	6178, 0.0578
R -Factor (%), wR_2 (%)	5.81, 16.76	5.09, 14.79	7.38, 16.26	6.48, 18.19
				5.15, 16.12

Table 4.7 Key intermolecular interactions for **1–3** complexes.

	1		2		3	
	150	295	295	150	295	295
T (K)						
NH...A (Å)	2.330	2.255	2.394	2.590	2.613	
Normalized NH...A ¹	0.801	0.775	0.785	0.794	0.802	
2-D sheets on ab plane						
CH _{imine} ...A (Å)	2.898	2.799	2.895	3.038	3.069	
Normalized CH...A ¹	0.996	0.962	0.950	0.932	0.941	
CH _{ethylene} ...A (Å)	2.742	2.741	2.818	3.059	3.072	
Normalized CH...A ¹	0.942	0.942	0.924	0.938	0.942	
CH _{ethylene} ... π (Å)	2.868	2.850	2.862	-	-	
Between 2-D sheets along c-axis						
CH _{ethyl} ... π (Å)	2.887	2.868	2.887	-	-	
CH _{ethyl} ...O (Å)	2.907	3.090	3.042	2.569	2.658	

[1] Normalized contacts (Hariharan, 2022) were calculated from the ratio of the experimental distances and sum of corresponding van der Waals atomic radii (Mantina et al., 2009) and Pauling ionic radii (Pauling, 1927).

Table 4.8 Key intermolecular interactions for **4** and **5** complexes.

	4			5		
	T (K)	150	295	30	100	295
NH...A (Å)		2.145	2.167	2.601	2.603	2.646
<i>2-D sheets on ab plane</i>						
CH _{imine} ...A (Å)		2.621	2.657	2.583	2.631	2.643
CH _{ethylene} ...A (Å)		2.670	2.669	2.495	2.694	2.645
CH _{ethylene} ... π (Å)		2.855	2.714	2.574	2.694	2.756
<i>Between 2-D sheets along c-axis</i>						
CH _{ethyl} ... π (Å)		-	-	-	-	-
CH _{ethyl} ...O (Å)		2.698	-	2.556	2.718	2.707

A feature that all the structures share is that a combination of N–H...anion and C–H...anion interactions link the cations. Notably, in **1** the N–H...Cl contacts at Fe1 and Fe2 differ by only 0.001 Å at 150 K, indicating minimal change. Even at 295 K, where symmetry breaking reduces the structure to a single Fe center, the N–H...Cl distance changes by just 0.07 Å. This stability suggests that the ligand field remains weak and does not strengthen enough to favor the LS state, even when the symmetry is lowered. Additionally, packing in **1** shows the formation of 1D chains of both Fe1 and Fe2 centers at 150 K, with neighboring chains linked through N–H...Cl and C–H...Cl interactions to form 2D sheets in the *ac* plane (Figure 4.12). This dense network appears to resist the contraction typically associated with the LS state, further stabilizing the HS configuration at LT. The electronic environment surrounding the Fe centers, influenced by hydrogen-bonding interactions with the Cl anions, may further contribute to the HS state stability by maintaining a relatively weak ligand field. Thus, despite symmetry breaking, the compound's rigid framework, stable ligand field, and network of intermolecular interactions effectively inhibit SCO, leading to the unusual retention of the HS state at both low and high temperatures. It is noteworthy that the packing closely resembles that of the related compound [Fe(naphBzen)₂]I which exhibits strongly hysteretic SCO and hidden hysteresis as a result of an extremely rare *reverse-LIESST* process (Boonprab et al., 2019). In comparison to the packing in the structure of complex **2**, we observe a distinct square motif (Figure 4.13) that resembles structural features seen in [Fe(salEen-5-I)₂]halide, particularly [Fe(salEen-5-I)₂]Br (Boonprab et al., 2024), which exhibits stepped SCO transition close to room temperature. However, unlike [Fe(salEen-5-I)₂]Br, complex **2** remains in the HS state even at LT, as evidenced by its magnetic profile (*vide infra*). This persistence of the HS state in **2**, despite structural similarities to SCO-active [Fe(salEen-5-I)₂]Br, suggests a potentially significant influence of the square arrangement within the lattice. Although the square motif is retained, its specific packing and intermolecular interactions appear to prevent SCO, maintaining the HS state at all observed temperatures. In complex **3**, the crystal lattice at both 295 K and 150 K consistently features a square motif, similar to that in [Fe(naphBzen)₂]Cl and [Fe(naphBzen)₂]Br (Habarakada et al., 2022), but uniquely exhibits a helical arrangement where the square motif spirals out of the 2D plane,

forming a three-dimensional structure (Figure 4.14). This distinctive helical configuration, stabilized by specific anion interactions, sets it apart from the diverse but planar packing patterns observed in the $[\text{Fe}(\text{naphBzen})_2]\text{halide}$ family in different solvates. We observe that the benzyl group of the salBzen ligand has a strong tendency to form a square arrangement with halide anions—a structural characteristic that appears to have been previously unrecognized. In our system, the anion plays a dominant role in stabilizing this arrangement. Both compounds **1** and **2** exhibit a clear square motif, while compound **3** also forms a square arrangement, though it differs in its spiral configuration that extends out of the 2D plane. This distinctive, non-planar arrangement in compound **3** underscores the versatility of the salBzen ligand and highlights the influence of specific anion interactions in directing the formation of unique packing motifs.

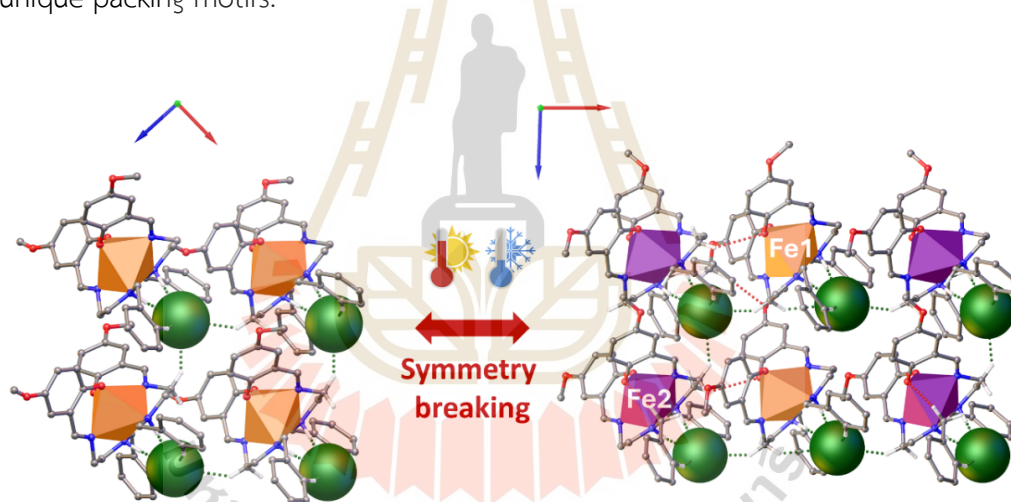


Figure 4.12 Spacefill packing $[\text{Fe}(\text{salBzen-5-OMe})_2]\text{Cl}$ (**1**) at 295 K (left) and 150 K (right) viewed along the b axis in HS state.

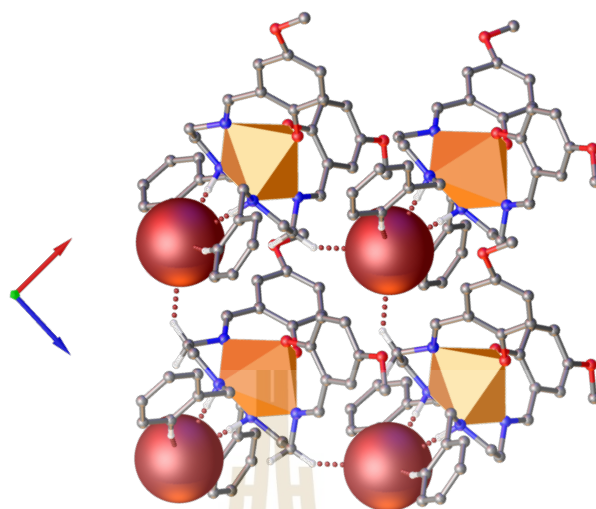


Figure 4.13 Spacefill packing $[\text{Fe}(\text{salBzen-5-OMe})_2]\text{Br}$ (**2**) at 295 K viewed along the *b* axis in HS state.

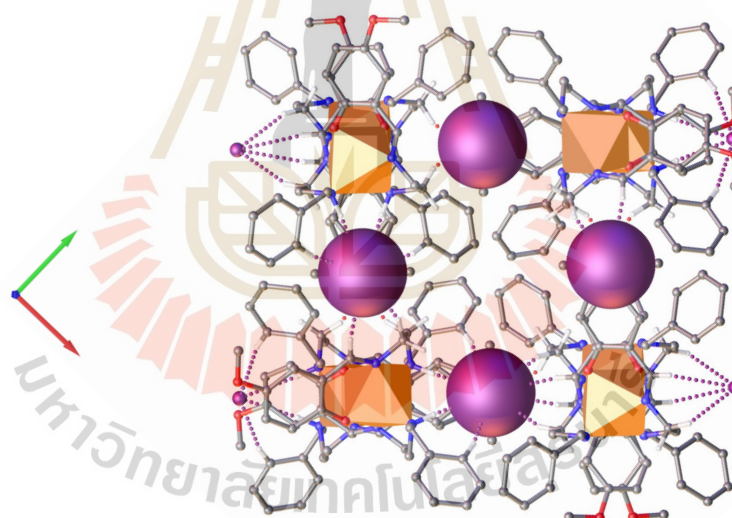


Figure 4.14 Spacefill packing of $[\text{Fe}(\text{salBzen-5-OMe})_2]\text{I}$ (**3**) at 295 K viewed along the *c* axis with LS state.

In complexes **4** and **5**, at 290 K and 30 K respectively, distinct packing patterns emerge compared to the other halide structures. A key feature of these two complexes is the formation of a 3D supramolecular network driven by a combination of C-H \cdots π , C-H \cdots O, N-H \cdots O, C-H \cdots anion, and N-H \cdots anion interactions, all involving the anion. In **4**, the Fe centers exhibit a dimer-like arrangement, forming pairs or clusters of complexes

that stack into a brick-like pattern of parallelograms (Figure 4.15). The NO_3 anions act as bridges or spacers, facilitating the dimerization and shaping the parallelogram-based packing motif. These dimeric interactions, likely stabilized by hydrogen bonding and coordination with NO_3 ions, result in an asymmetric yet efficient packing arrangement. Compared to the square motif observed in compound **3**, the structure of complex **4** is less symmetric, with a more layered and staggered arrangement of complexes. For complex **5**, the Fe centers are organized into layers, forming a repeating pattern where the units shift slightly between layers. The ClO_4 ions function as spacers, stabilizing the structure through weak interactions and ionic forces. The packing pattern is defined by a trapezoidal tessellation (Figure 4.16), representing a slight distortion from a perfect square grid. This distortion introduces a layered and slightly offset arrangement, likely influenced by the size and interaction dynamics of the ClO_4 ions.

The comparison of complexes **4** and **5** highlights the significant role of different anions (ClO_4^- and NO_3^-) in influencing packing and symmetry. These observations underscore how subtle variations in the molecular environment can result in diverse and unique packing motifs.

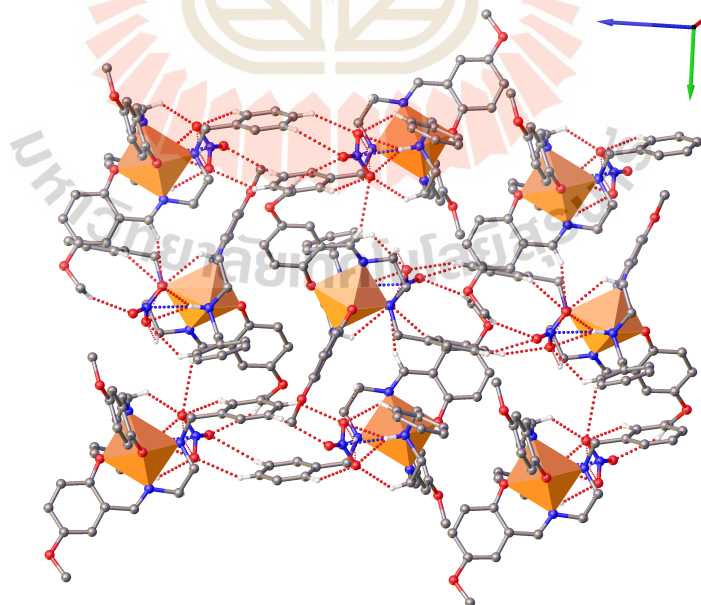


Figure 4.15 Packing of $[\text{Fe}(\text{salBzen-5-OMe})_2]\text{NO}_3$ (**4**) at 295 K viewed along the c axis in LS state.

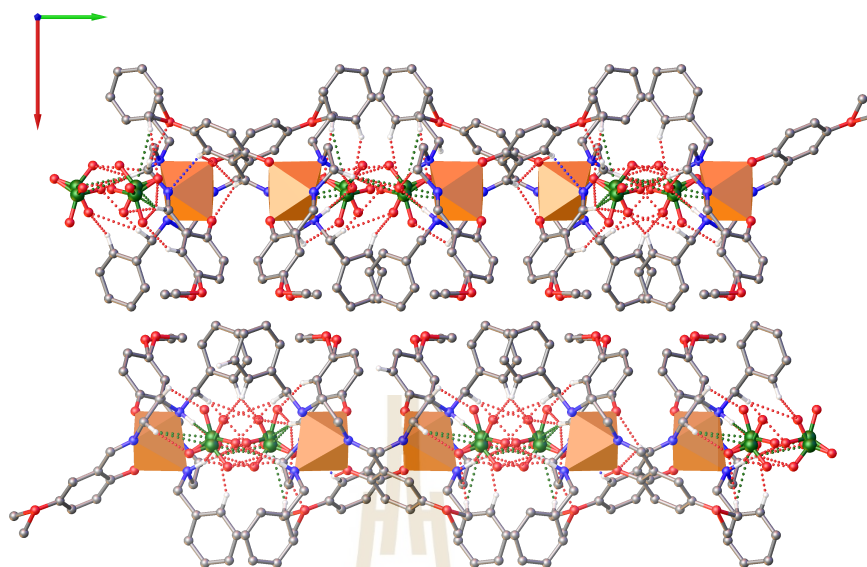


Figure 4.16 Packing of $[\text{Fe}(\text{salBzen-5-OMe})_2]\text{ClO}_4$ (**5**) at 100 K viewed along the c axis in HS state.

4.3 Hirshfeld surface data analysis of Fe(III) Schiff base complexes

Hirshfeld surfaces highlight the role of intermolecular interactions in creating a network of contacts between cations and anions, as well as neighboring cations within the crystal lattice. These interactions arise from functional groups associated with the counterions or cations, including N–H, C–H, aromatic rings, and halides. The red regions on the isosurface indicate significant hydrogen bonding at the $\text{H}\cdots\text{O}$, $\text{H}\cdots\pi$, and $\text{H}\cdots\text{H}$ sites. The positioning of counteranions within the lattice promotes $\text{C-H}\cdots\text{A}$ and $\text{N-H}\cdots\text{A}$ interactions, with darker red spots reflecting stronger interactions, particularly between C–H and N–H groups and counteranions, as shown in Figure 4.17. In contrast, weaker $\text{H}\cdots\text{H}$ interactions within the lattice correspond to lighter red regions, while the strength of $\text{H}\cdots\text{A}$ interactions varies with the electronegativity of the halide.

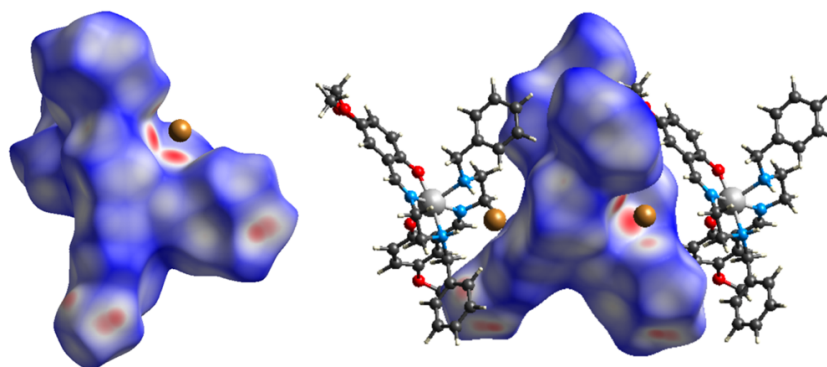


Figure 4.17 Intramolecular interactions (covalent bond) (left) and C–H $\cdots\pi$ interactions (right) through Hirshfeld surface mapping by d_{norm} function.

The Hirshfeld surfaces of compounds **1–5** clearly show that C–H $\cdots\pi$ and H \cdots O interactions significantly contribute to the total interactions, accounting for 19.6–27.6% and 7.1–21.6%, respectively. The H \cdots A interactions, influenced by the halides, contribute 5.2–7.4%. The 2D fingerprint plots in Figures 4.18 and 4.19 further illustrate these contributions. Substituents influence spin crossover behavior by altering these interactions. Complexes with Cl $^-$ and Br $^-$ anions show stronger N–H \cdots halide interactions, stabilizing the HS state and preventing SCO. In contrast, the weaker N–H \cdots halide interactions with the larger, more polarizable I $^-$ anion, stabilizing the LS state and leading to a gradual SCO above 350 K. This trend is consistent with the [Fe(salEen-I) $_2$]halide series (Boonprab et al., 2024), where weaker interactions promote the LS state. However, in the [Fe(salEen-I) $_2$]halide series, the SCO occurs with the Br $^-$ anion, whereas in the [Fe(salBzen-5-OMe) $_2$]halide series, it occurs between Br $^-$ and I $^-$.

Hirshfeld analysis indicates that varying substituents impact the characteristics of the spin crossover. The nature of the counteranion significantly affects the contributions of H \cdots C and H \cdots O interactions. Halide complexes **1–3** exhibited comparable H \cdots C and H \cdots O interactions, reflecting the similar sizes and polarizabilities of the halide ligands. However, complexes containing NO $_3$ **4** and ClO $_4$ **5** demonstrated significantly enhanced H \cdots O interactions due to the presence of oxygen atoms in the anions capable of forming weak hydrogen bonds. The thermal dependence of these interactions also revealed that the H \cdots O contributions increased with temperature in

these complexes, highlighting the interplay between thermal motion and intermolecular forces.

Hirshfeld analysis confirms that substituents significantly influence SCO behavior by modifying intermolecular interactions and lattice packing. Strongly coordinating anions, such as such as Cl **1** and Br **2**, create a more rigid lattice, leading to a narrower SCO transition range. In contrast, ClO_4 **5**, exhibits only a weak SCO, likely due to disorder in the ClO_4 anion between 80 K and 90 K, which appears to drive the observed transition. Meanwhile, NO_3 **4** behaves more similarly to I **3** than to ClO_4 **5**, suggesting intermediate effects on the SCO process.

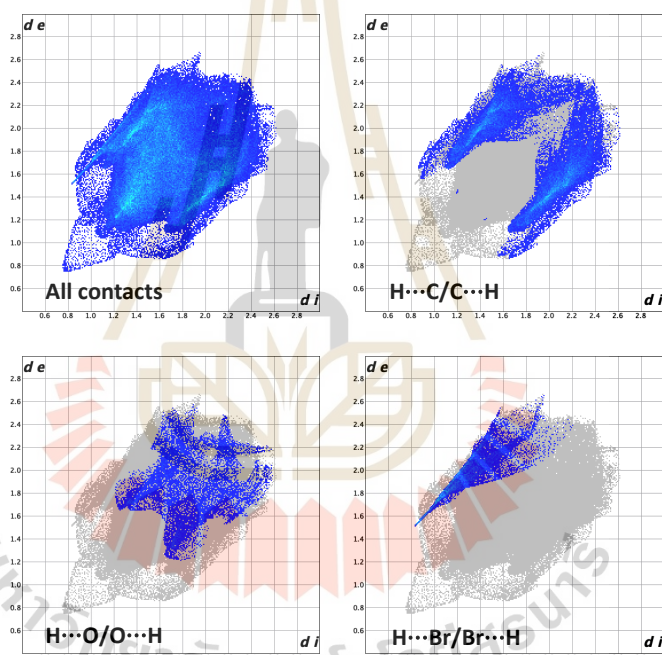


Figure 4.18 2D fingerprint plots of all contacts: $\text{H}\cdots\text{C}$, $\text{H}\cdots\text{H}$ and $\text{H}\cdots\text{O}$ for **2** at 295 K.

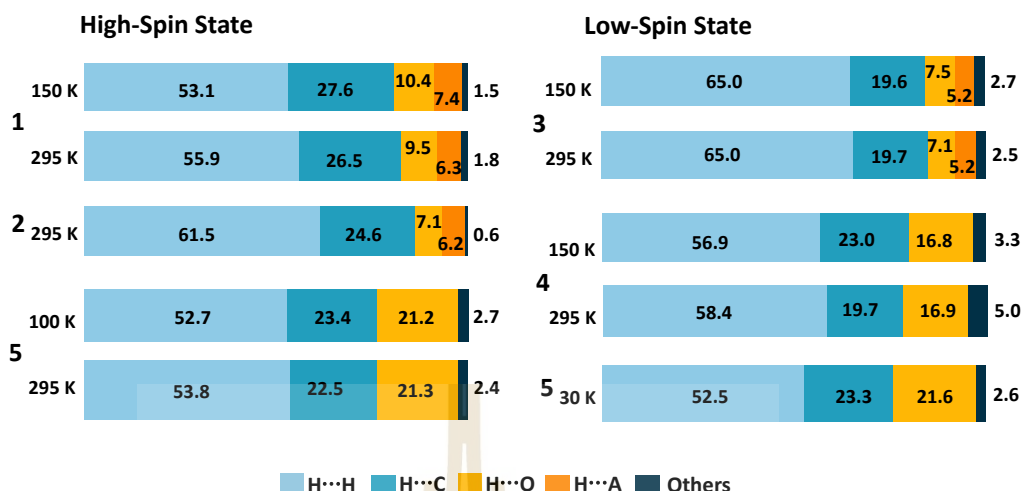


Figure 4.19 Percentage contributions of interactions for complexes 1-5.

4.4 Magnetic studies of Fe(III) Schiff base complexes

The magnetic properties of **1-5** were undertaken using SQUID magnetometry over the 10–380 K range and are presented as $\chi_M T$ vs. T plots in Figure 4.20 (χ_M is defined as the magnetic susceptibility, expressed as M/H per mole of the complex). The $\chi_M T$ values for complexes **1** and **2**, which remain in the range of $4.00\text{--}4.50\text{ cm}^3\text{ K mol}^{-1}$ between 10 and 300 K, and are indicative of HS Fe(III) centers across the entire temperature range, with complex **1** maintaining a $\chi_M T$ value around $4.50\text{ cm}^3\text{ K mol}^{-1}$ at all temperatures, in agreement with X-ray crystallographic analysis, and complex **2** exhibits a similar magnetic profile, with a $\chi_M T$ value of $4.40\text{ cm}^3\text{ K mol}^{-1}$ at 150 K and remaining HS down to 10 K. These values agree well with Fe(III) complexes within the same ligand family (Al-Azzani et al., 2020; Boonprab et al., 2024; Dey et al., 2020; Marques et al., 2023; Shongwe et al., 2012). In contrast, in the $[\text{Fe}(\text{naphBzen})_2]\text{Cl}$ and $[\text{Fe}(\text{naphBzen})_2]\text{Br}$ complexes (Habarakada et al., 2022), different solvates can be obtained through recrystallization from various solvents. Notably, in the CHCl_3 solvates, both complexes remain trapped in the LS state. Magnetic data indicate that SCO occurs only in the hexane solvates, highlighting that even very weak interactions can play a critical role in facilitating SCO behavior. It is evident that the naphBzen complexes tend to exhibit very gradual and minimal transitions, resulting in predominantly mixed HS

and LS states. This telling us the salBzen ligand is substantially more HS than the naphBzen and naphEen ligands.

In contrast, the $\chi_{\text{M}}T$ value of **3** is around $0.52 \text{ cm}^3 \text{ K mol}^{-1}$ at 100 K and aligns with an LS Fe(III) center, supporting agreement with X-ray crystallographic analysis. Upon heating of **3** undergoes a gradual and smooth spin crossover, reaching $\chi_{\text{M}}T$ of $2.09 \text{ cm}^3 \text{ K mol}^{-1}$ at 380 K, this suggests that the spin crossover remains incomplete at this temperature (Boonprab et al., 2018; Marques et al., 2023; Martinho et al., 2014; Vicente et al., 2016). Similarly, complex **4** displays a $\chi_{\text{M}}T$ value of $0.46 \text{ cm}^3 \text{ K mol}^{-1}$ at 100 K, also consistent with a LS Fe(III) centre and agrees well with SCXRD. Upon heating, the $\chi_{\text{M}}T$ value begins to slightly increase, reaching $1.38 \text{ cm}^3 \text{ K mol}^{-1}$ at 380 K, which is slightly lower than that of complex **3**. These profiles suggest that both compounds **3** and **4** exhibit predominantly gradual spin crossover above 350 K. Similar behavior has been reported in in $[\text{Fe}(\text{salEen-5-I})_2]$ (Boonprab et al., 2024), which shows a gradual and incomplete SCO from LS to mHS over the examined temperature range. Notably, the $T_{1/2}$ values recorded for $[\text{Fe}(\text{salEen-5-I})_2]\text{halide}$ (Boonprab et al., 2024) increase as the anionic radii increases, suggesting that bigger anions stabilize the LS state — a trend consistent with our system, $[\text{Fe}(\text{salBzen-5-OMe})_2]\text{A}$, as it moves from chloride to iodide. For complex **5**, the $\chi_{\text{M}}T$ value is around $4.42 \text{ cm}^3 \text{ K mol}^{-1}$ at 300 K indicating that the complex is almost fully HS. Upon cooling down to 100 K, the $\chi_{\text{M}}T$ value remains around $4.35 \text{ cm}^3 \text{ K mol}^{-1}$, confirming that the complex stays in the HS Fe(III) state, consistent with SCXRD results. However, the $\chi_{\text{M}}T$ value drops abruptly below 70 K, reaching about $3.50 \text{ cm}^3 \text{ K mol}^{-1}$, indicating a partial SCO, which aligns with the structural data. Continued cooling causes no significant variation in the $\chi_{\text{M}}T$ value, and upon reheating, the spin crossover resumes abruptly, beginning at 60 K. Consequently, the spin transition occurs with a slight hysteresis of 6 K., corresponding to 20% switching of the Fe(III) centres. Notably, such a spin transition with hysteresis at very low temperatures is highly unusual in spin crossover chemistry, especially for Fe(III). This behavior suggests that the salBzen ligand system, combined with appropriate anions, offer a valuable tool for tuning the temperature at which spin crossover occurs.

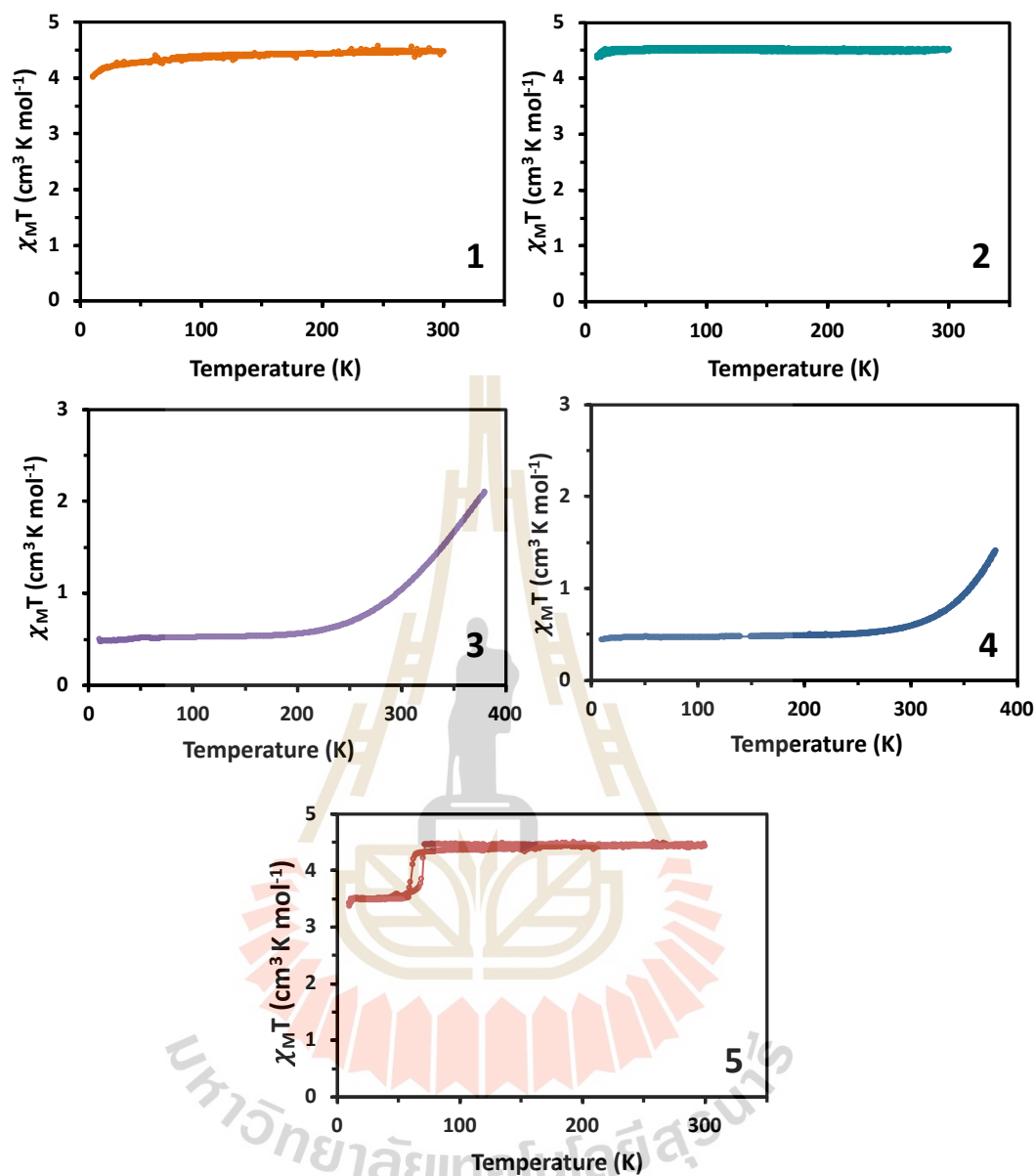


Figure 4.20 $\chi_M T$ versus T plots for 1–5 complexes.

The magnetic properties of complexes **6-10** were investigated using direct current (dc) susceptibility and magnetization measurements. These measurements were conducted on a Quantum Design MPMS 3 SQUID magnetometer over the temperature range of 1.8–300 K or 1.8–400 K. The measurement protocol involved four sequential steps: cooling from 300 to 1.8 K (cooling 1), before measuring to 400 K (heating 1), followed by measurement to 1.8 K (Cooling 2), followed by measurement to 400 K (heating 2). Magnetisation (M) vs field (H) measurements were conducted between 0 and 7 T at 1.8, 4 and 7 K, as shown in Figure 4.21.

The variation of magnetic susceptibility with temperature, $\chi_M T$, was measured during both cooling and heating cycles across the 2–400 K range. The data reveal a gradual increase in $\chi_M T$ with increasing temperature for all complexes, indicating temperature-driven spin-state transitions on the Fe(III) centers. The first magnetic profile is different to the next one suggesting an irreversible change (probably solvent water loss). At high temperatures (above ~300 K), all complexes display $\chi_M T$ values converging toward 3.5–4.0 cm³ K mol⁻¹, consistent with a high-spin state of Fe(III) in a weak-field environment. However, significant differences emerge in the low-temperature region. Complexes **6** and **7** exhibit nearly identical magnetic behavior across the entire temperature range, reflecting the similar crystal field strengths and electronic environments provided by these halide anions. In contrast, complex **8** shows a slightly lower $\chi_M T$ values at low temperatures, potentially due to the larger size of the iodide, which may stabilize a partial low-spin state or promote antiferromagnetic interactions. Complexes **9** and **10** exhibit higher $\chi_M T$ values in the low-temperature region compared to the halide-containing complexes. This behavior is likely due to the weaker intermolecular interactions of NO₃ and ClO₄ anions, which lead to reduced stabilization of the low-spin state. These findings highlight the role of counteranion size and interaction strength in governing the SCO behavior of Fe(III) Schiff base complexes.

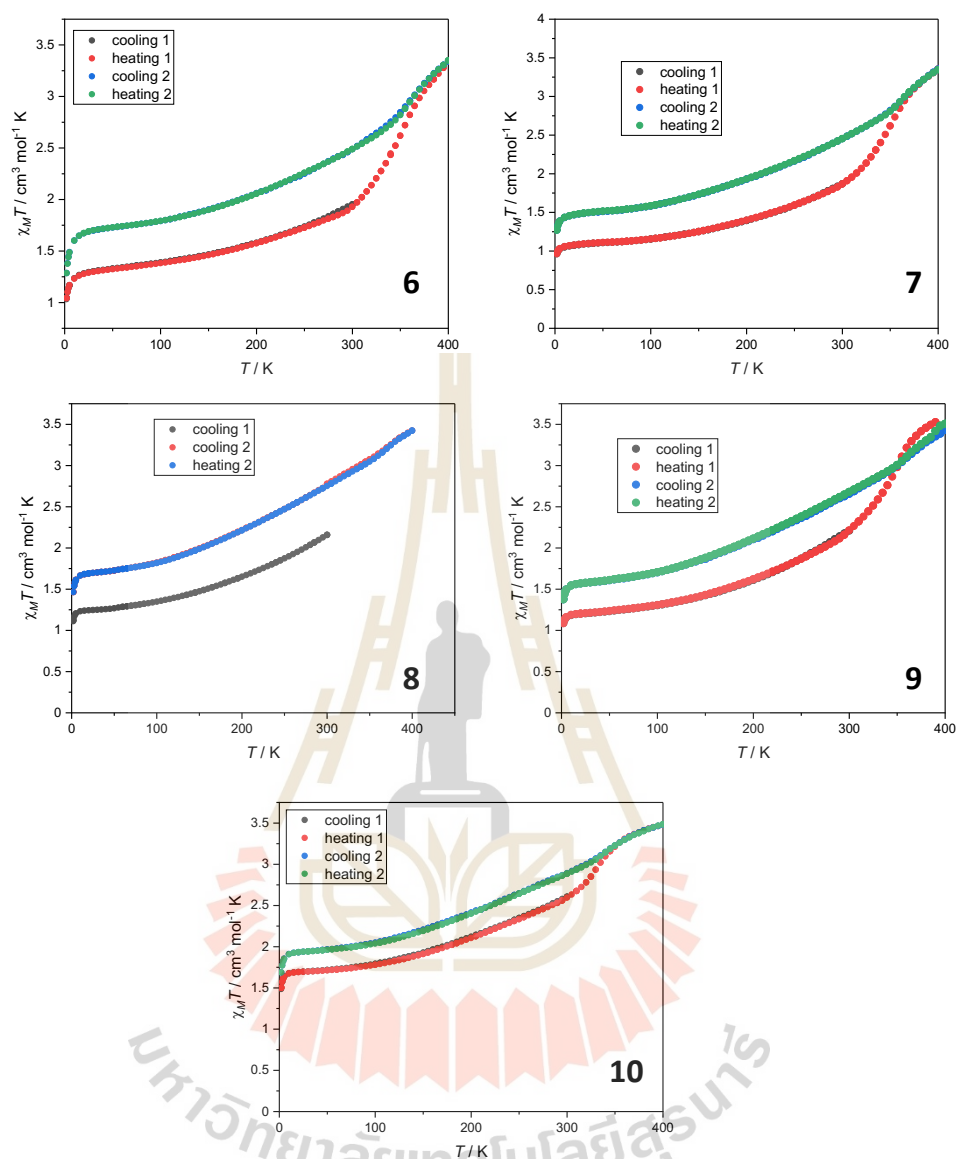


Figure 4.21 $\chi_M T$ versus T plots for 6–10 complexes.

4.5 Magnetostructural Relationship of Fe(III) complexes

To gain deeper insight into the varying SCO profiles of the complexes, the packing arrangements within their structures were analyzed. In complexes **1-3**, the molecular packing is primarily governed by strong N-H...anion and C-H...anion interactions, resulting in the formation of two-dimensional (2D) sheets. The normalized N-H...anion contacts range from 0.77 to 0.80 (Table 4.7), whereas the C-H...anion interactions are comparatively weaker, with normalized contact values close to 1.0. However, these interactions slightly strengthen during the gradual SCO in complex **3**. The helical chain formed by these interactions stack along the c-axis through weak C-H... π and C-H...O interactions, suggesting that the most significant contacts occur within the helical chain themselves.

To analyze structural changes related to magnetic profiles, three characteristics (**A-C**) similar to those we previously defined for [Fe(salEen-I)₂]halide (Boonprab et al., 2024), were created to describe the square configuration of the cationic complexes surrounding the anion within the sheets, as shown in Figure 4.22. These parameters show an increase with the size of the anion, regardless of the spin state, highlighting the lattice space occupied by each anion (Table 4.9). For complexes **1** and **2**, the smaller values of **A-C** suggest a threshold below which SCO cannot occur. In contrast, complex **3** shows an increase in these parameters with temperature, indicating tighter trapping of the anion during SCO. This behavior aligns with the more gradual SCO observed in complex **3**.

In comparison, the previously studied [Fe(salEen-I)₂]halides exhibited a different trend. For these complexes, **A-C** parameters decreased with increasing temperature during SCO, reflecting lattice contraction as the anion became more tightly confined. This trend was particularly pronounced in [Fe(salEen-I)₂]Br, where sharp decreases in parameters **B** and **C** (by 0.31 and 0.15 Å, respectively) between 275 and 280 K corresponded to the initial step in the SCO profile, while a subsequent reduction in **A** (~0.2 Å) correlated with the more abrupt SCO transition. In contrast, [Fe(salEen-I)₂]I displayed only subtle changes in **A-C** (less than 0.1 Å), consistent with its compact packing and gradual SCO (Boonprab et al., 2024). These comparisons highlight that the gradual SCO behavior observed in complex **3** arises from greater lattice flexibility and

enhanced anion-cation interactions. This contrasts with the rigid structural response of $[\text{Fe}(\text{salEen-I})_2]\text{halides}$, where abrupt SCO transitions dominate due to tighter lattice confinement and reduced flexibility.

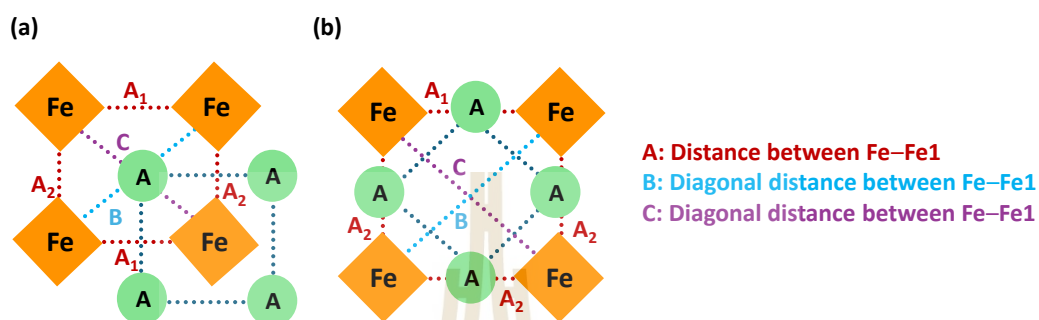


Figure 4.22. (a) Simplified illustration of 1–2 and (b) 3 viewed showing the three structural parameters, A_1 , A_2 , B and C.

Table 4.9 Structural characteristics of complexes 1–3.

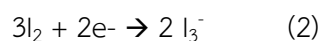
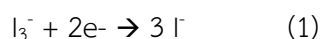
Complexes	Structural characteristic (Å)			
	A_1	A_2	B	C
$[\text{Fe}(\text{salBzen-5-OMe})_2]\text{Cl}$ 1				
150 K	7.329	7.773	10.293	11.061
295 K	7.875	7.637	10.887	11.061
$[\text{Fe}(\text{salBzen-5-OMe})_2]\text{Br}$ 2				
295 K	7.954	7.694	10.889	11.239
$[\text{Fe}(\text{salBzen-5-OMe})_2]\text{I}$ 3				
150 K	11.378	10.530	15.923	14.412
295 K	11.426	10.565	16.001	14.441
	A		B	C
$[\text{Fe}(\text{salEen-5-I})_2]\text{Cl}$				
150 K	7.481		9.85	11.26

Table 4.9 Structural characteristics of complexes **1–3** (Continued).

[Fe(salEen-5-I) ₂]Br			
123 K	7.970	10.75	11.77
275 K	7.985	10.70	11.75
280 K	7.947	10.39	11.60
293 K	7.773	10.37	11.58
305 K	7.776	10.37	11.58
[Fe(salEen-5-I) ₂]I			
293 K	8.273	11.33	12.06
400 K	8.239	11.30	11.99
425 K	8.239	11.30	11.99

4.6 Cyclic voltammetric studies of Fe(III) Schiff base complexes

The electrochemistry of [Fe(salBzen-5-OMe)₂]A, **1–5** in dry CH₂Cl₂ was studied using cyclic voltammetry. The cyclic voltammogram of all the complexes are shown in Figures 4.23 and 4.24. The CV measurements, conducted over the potential range of -1.0 to 1.2 V, exhibit distinct redox features corresponding to both metal-centered and ligand-centered electron transfer processes. All complexes display a quasi-reversible Fe(III)/Fe(II) redox couple, with the reduction of Fe(III) to Fe(II) observed during the cathodic scan between -0.50 to -0.35 V and oxidation during the anodic scan at around 0.9–1.0 V, assigned to the salBzen-5-OMe ligand, specifically oxidation at the oxygen of the phenolate (Harding et al., 2013). The potentials of the Fe(II)/Fe(III) redox couple varies a lot from -0.55 V to -0.39 V with a clear relationship between the strength of the N–H...A interactions and the size of the anion. Moreover, for **3** two extra redox events occur and are attributed to the redox reactions of I[•]/I₃^{•-} and I₂/I₃^{•-}, the redox peaks on the left correspond to Eq. (1), while those on the right correspond to Eq. (2) (Ma et al., 2021).



The reduction potentials for the Fe(II)/Fe(III) redox couple demonstrate how the hydrogen bonding strength of the counteranion affects the stability of the Fe(III) oxidation state. Complex **1**, exhibits the most negative potential (-0.55 V), reflecting the strong stabilizing effect of Cl⁻ on Fe(III). In comparison, **2** (-0.47 V) and **3** (-0.39 V) complexes display less negative potentials, consistent with the weaker hydrogen bonding capability of these larger halides of Br⁻ and I⁻, respectively. Additionally, two distinct trends emerge when comparing halide and non-halide counteranions. Complex **4** (-0.52 V) has a reduction potential close to that of complex **1**, suggesting that multiple N-H...O hydrogen bonds significantly contribute to Fe(III) stabilization. In contrast, complex **5** (-0.42 V) has the least negative potential, showing that the larger anion interacts weakly with the complex. These trends highlight how both the size and hydrogen bonding capability influence the redox properties of these Fe(III) complexes.

The ligand oxidation potentials are mostly unchanged across all complexes, showing that counteranions have little effect on the ligand's electronic properties. Complex **3** has the highest oxidation potential (1.00 V), suggesting the weakest electron-withdrawing influence. Complexes **2** (0.96 V) and **1** (0.91 V) show slightly lower values due to stronger electron-withdrawing effects that stabilize the oxidized ligand. Similarly, **4** (0.92 V) and **5** (0.96 V) have moderate oxidation potentials, confirming their minimal impact. This consistency supports the idea that the anions mainly stabilize the metal center rather than significantly altering the ligand's redox properties.

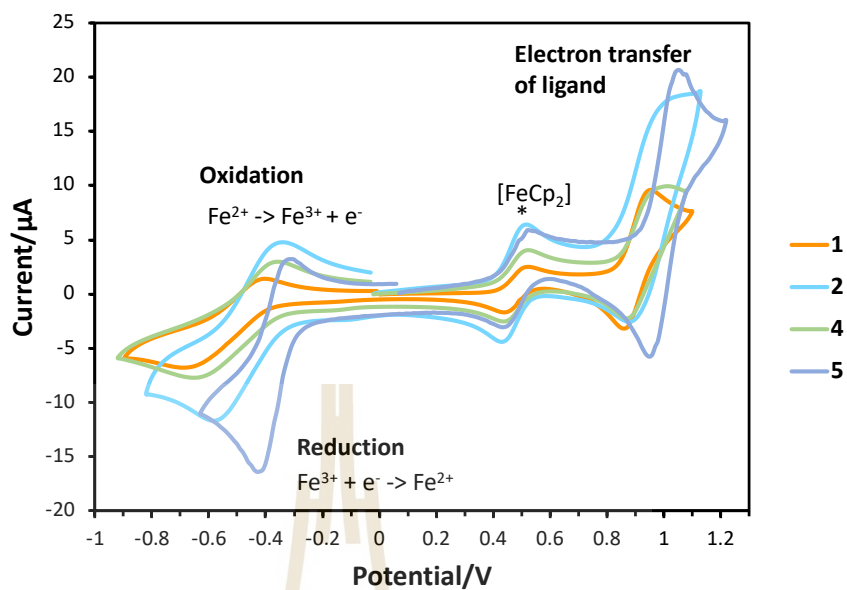


Figure 4.23 Cyclic voltammograms of $[\text{Fe}(\text{salBzen-5-OMe})_2]\text{A}$ in CH_2Cl_2 solution at a scan rate of 100 mVs^{-1} .

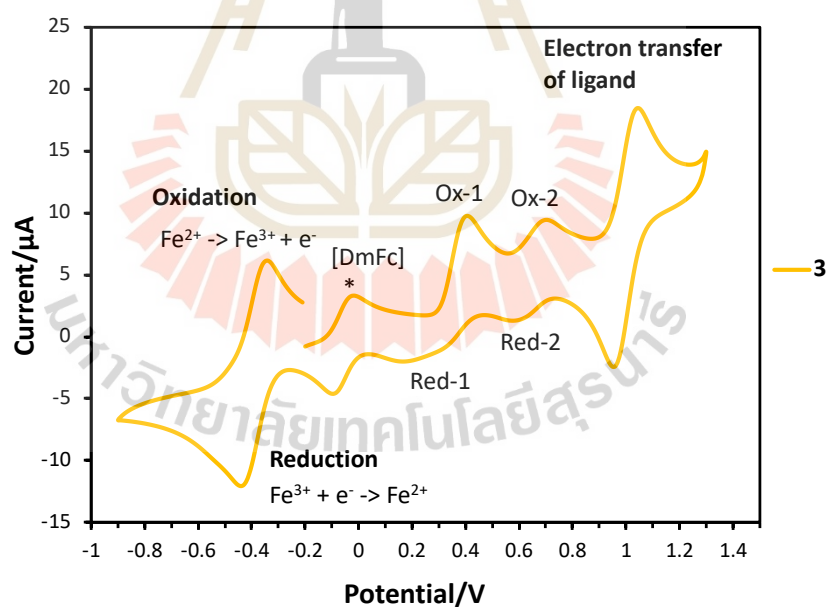


Figure 4.24 Cyclic voltammogram of $[\text{Fe}(\text{salBzen-5-OMe})_2]\text{I}$ in CH_2Cl_2 solution at a scan rate of 100 mVs^{-1} .

Table 4.10 Electrochemical data of $[\text{Fe}(\text{salBzen-5-OMe})_2]\text{A}$ in CH_2Cl_2 solution at 298 K.

Complex ^a	$E^{\circ'}$ [V] ($\text{Fe}^{2+/3+}$)	$E^{\circ'}$ [V] (ligand)
1	-0.55 ^b	0.91 ^c
2	-0.47	0.96
3	-0.39	1.00
4	-0.52	0.92
5	-0.42	0.96

^a All measurements were conducted at 298 K in dried and degassed CH_2Cl_2 0.1 M $[\text{NBu}_4][\text{PF}_6]$ solution; scan rate 100 mVs^{-1} .

^b This corresponds to the peak potential.

^c The first reduction peak potential is used to determine $E^{\circ'}$.

The electrochemistry of $[\text{Fe}(\text{salPren-5-OMe})_2]\text{A}$, **6-10** in dry CH_2Cl_2 was studied by using cyclic voltammetry. The cyclic voltammogram of all the complexes is given in Figures 4.25 and 4.26 which also revealed distinct redox behavior influenced by the counteranion. Moreover, for **8** there are exhibit two pairs of oxidation-reduction peaks, which are attributed to the redox reactions of I^-/I_3^- and I_2/I_3^- , the redox peaks on the left correspond to Eq. (1), while those on the right correspond to Eq. (2) (Ma et al., 2021). The reduction potentials for the Fe(II)/Fe(III) redox couple are relatively consistent across the complexes, ranging from -0.49 V to -0.46 V. Complex **6** shows a slightly more negative potential at -0.47 V, indicating a slightly stronger stabilizing effect on Fe(III) compared to Br^- **7**, I^- **8**, and ClO_4^- **10**. The ligand oxidation potentials occur around 0.9 V, corresponding to oxidation within the Schiff base ligand's aromatic system. The second peak, appearing at higher potentials around 1.3 V, likely involves a subsequent ligand oxidation. The first oxidation process occurs in a narrow range between 0.91 V (**10**) and 0.95 V (**6** and **7**). The similarity across this redox process suggests limited influence of the counteranions on the first oxidation state of the ligand. However, in the second oxidation process, variations are more pronounced. The Cl^- complex **6** exhibits the highest potential (1.38 V), followed closely by Br^- **7** (1.37 V),

NO_3^- **9** (1.34 V), ClO_4^- **10** (1.32 V), and I^- **8** (1.30 V). The reasons for this difference are unclear.

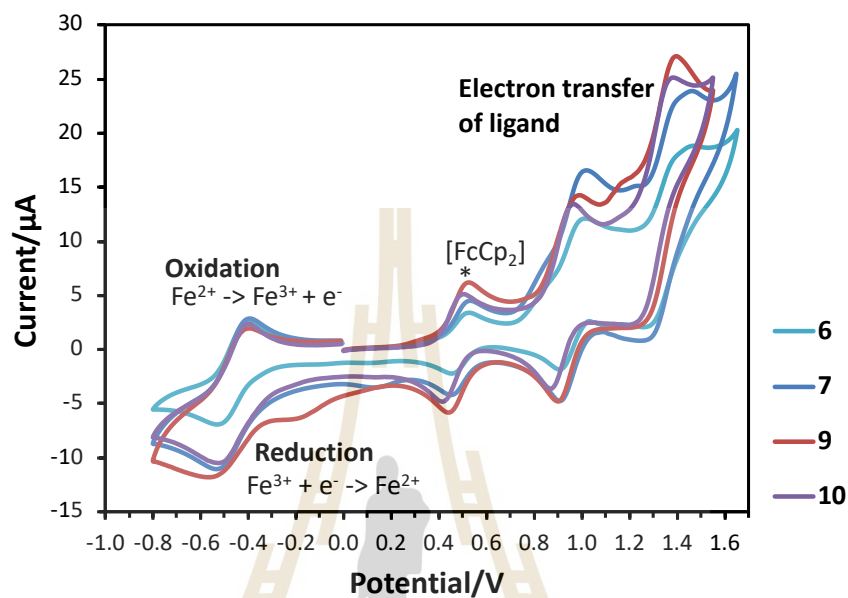


Figure 4.25 Cyclic voltammograms of $[\text{Fe}(\text{salPren-5-OMe})_2]\text{A}$ in CH_2Cl_2 solution at a scan rate of 100 mVs^{-1} .

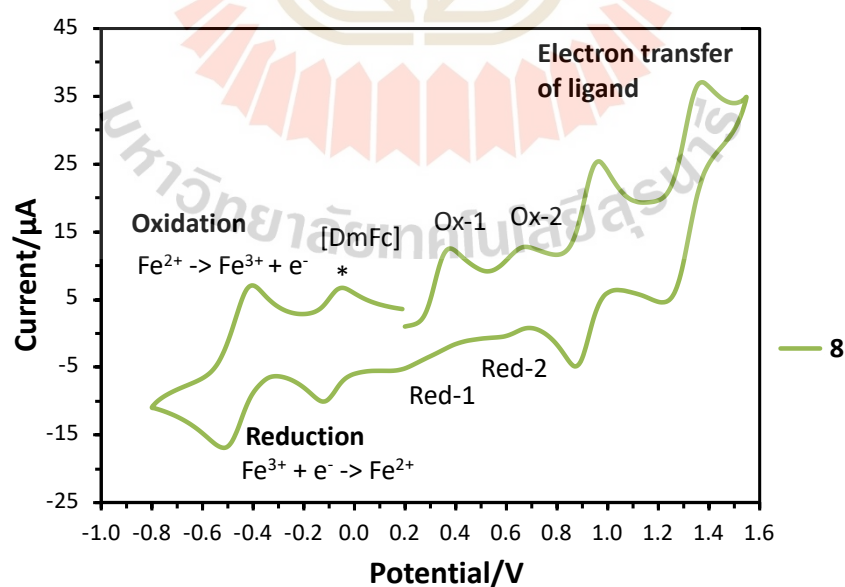


Figure 4.26 Cyclic voltammograms of $[\text{Fe}(\text{salPren-5-OMe})_2]\text{I}$ in CH_2Cl_2 solution at a scan rate of 100 mVs^{-1} .

Table 4.11 Electrochemical data of $[\text{Fe}(\text{salPren-5-OMe})_2]\text{A}$ in CH_2Cl_2 solution at 298 K.

Complex ^a	$E^{\circ'}$ [V] ($\text{Fe}^{2+/3+}$)	$E^{\circ'}$ [V] (ligand-p1)	$E^{\circ'}$ [V] (ligand-p2)
6	-0.47 ^b	0.95 ^c	1.38 ^c
7	-0.46	0.95	1.37
8	-0.46	0.92	1.30
9	-0.49	0.94	1.34
10	-0.46	0.91	1.32

^a All measurements were conducted at 298 K in dried and degassed CH_2Cl_2 0.1 M $[\text{NBu}_4][\text{PF}_6]$ solution; scan rate 100 mVs^{-1} .

^b This corresponds to the peak potential.

^c The first reduction peak potential is used to determine $E^{\circ'}$.

The comparison between $[\text{Fe}(\text{salPren-5-OMe})_2]\text{A}$, **6–10** and $[\text{Fe}(\text{salBzen-5-OMe})_2]\text{A}$, **1–5** complexes highlights the impact of ligand structure and counteranions on electrochemical behavior. The salBzen series exhibits greater variation in redox potentials depending on the counteranion, likely because the benzyl groups create a more well defined binding pocket that strengthens anion-dependent redox shifts. In contrast, the salPren series shows more consistent redox potentials across different anions, suggesting that its more flexible ligand structure allows greater anion mobility, reducing direct stabilization of the $\text{Fe}(\text{III})$ center. These findings emphasize the crucial role of ligand rigidity and counteranion interactions in modulating the redox properties and electron transfer dynamics of $\text{Fe}(\text{III})$ Schiff base complexes.

4.7 References

- Al-Azzani, M. A., Al-Mjeni, F., Mitsuhashi, R., Mikuriya, M., Al-Omari, I. A., Robertson, C. C., Bill, E., and Shongwe, M. S. (2020). Unusual Magneto-Structural Features of the Halo-Substituted Materials $[\text{Fe}^{\text{III}}(5\text{-X-salMeen})_2]\text{Y}$: a Cooperative $[\text{HS-HS}] \leftrightarrow [\text{HS-LS}]$ Spin Transition. *Chemistry – A European Journal*, 26(21), 4766–4779. doi: <https://doi.org/10.1002/chem.201904744>
- Bertrand, J. A., Breece, J. L., and Eller, P. G. (1974). Structure studies of iron(III) salicylaldimine complexes. Five-coordinate monomeric and dimeric complexes. *Inorganic Chemistry*, 13(1), 125–131. doi: 10.1021/ic50131a024
- Boonprab, T., Harding, P., Murray, K. S., Phonsri, W., Telfer, S. G., Alkaş, A., Ketkaew, R., Tantirungrotechai, Y., Jameson, G. N. L., and Harding, D. J. (2018). Solvatomorphism and anion effects in predominantly low spin iron(III) Schiff base complexes. *Dalton Trans.*, 47(35), 12449–12458. doi: 10.1039/C8DT02016G
- Boonprab, T., Lee, S. J., Telfer, S. G., Murray, K. S., Phonsri, W., Chastanet, G., Collet, E., Trzop, E., Jameson, G. N. L., Harding, P., and Harding, D. J. (2019). The First Observation of Hidden Hysteresis in an Iron(III) Spin-Crossover Complex. *Angewandte Chemie International Edition*, 58(34), 11811–11815. doi: <https://doi.org/10.1002/anie.201907619>
- Boonprab, T., Thammasangwan, W., Chastanet, G., Gonidec, M., Harding, P., and Harding, D. J. (2024). Halide Anion Effects and Magnetostructural Relationships in Iron(III) Spin Crossover Complexes. *Crystal Growth & Design*, 24, 8145–8152. doi: 10.1021/acs.cgd.4c01068
- Cardoso, B. de P., Vicente, A. I., Ward, J. B. J., Sebastião, P. J., Chávez, F. V., Barroso, S., Carvalho, A., Keely, S. J., Martinho, P. N., and Calhorda, M. J. (2015). Fe(III) salEen derived Schiff base complexes as potential contrast agents. *Inorganica Chimica Acta*, 432, 258–266. doi: <https://doi.org/10.1016/j.ica.2015.04.026>
- Dey, B., Mondal, A., and Konar, S. (2020). Effect of Ligand Field Strength on the Spin Crossover Behaviour in 5-X-SalEen (X=Me, Br and OMe) Based Fe(III) Complexes. *Chemistry – An Asian Journal*, 15(11), 1709–1721. doi: <https://doi.org/10.1002/asia.202000156>

- Díaz-Torres, R., Phonsri, W., Murray, K. S., Liu, L., Ahmed, M., Neville, S. M., Harding, P., and Harding, D. J. (2020). Spin Crossover in Iron(III) Quinolylsalicylaldiminates: The Curious Case of $[\text{Fe}(\text{qsal-F})_2](\text{Anion})$. *Inorganic Chemistry*, 59(18), 13784–13791. doi: 10.1021/acs.inorgchem.0c02201
- Habarakada, U., Boonprab, T., Harding, P., S. Murray, K., Phonsri, W., M. Neville, S., Ahmed, M., and J. Harding, D. (2022). Solvent Effects on the Structural and Magnetic Properties of FeIII Spin-Crossover Complexes. *Crystal Growth & Design*, 22(8), 4895–4905. doi: 10.1021/acs.cgd.2c00390
- Harding, D. J., Sertphon, D., Harding, P., Murray, K. S., Moubaraki, B., Cashion, J. D., and Adams, H. (2013). FeIII Quinolylsalicylalimine Complexes: A Rare Mixed-Spin-State Complex and Abrupt Spin Crossover. *Chemistry – A European Journal*, 19(3), 1082–1090. doi: <https://doi.org/10.1002/chem.201202053>
- Hariharan, M. (2022). Virtual Issue on Halogen Bonding. *Crystal Growth & Design*, 22(4), 2046–2049. doi: 10.1021/acs.cgd.2c00157
- Hayami, S., Gu, Z., Shiro, M., Einaga, Y., Fujishima, A., and Sato, O. (2000). First Observation of Light-Induced Excited Spin State Trapping for an Iron(III) Complex. *Journal of the American Chemical Society*, 122(29), 7126–7127. doi: 10.1021/ja001406e
- Kang, B., Tang, H., Zhao, Z., and Song, S. (2020). Hofmeister Series: Insights of Ion Specificity from Amphiphilic Assembly and Interface Property. *ACS Omega*, 5(12), 6229–6239. doi: 10.1021/acsomega.0c00237
- Ketkaew, R., Tantirungrotechai, Y., Harding, P., Chastanet, G., Guionneau, P., Marchivie, M., and Harding, D. J. (2021). OctaDist: a tool for calculating distortion parameters in spin crossover and coordination complexes. *Dalton Transactions*, 50(3), 1086–1096. doi: 10.1039/D0DT03988H
- Ma, J., Liu, M., He, Y., and Zhang, J. (2021). Iodine Redox Chemistry in Rechargeable Batteries. *Angewandte Chemie International Edition*, 60. doi: 10.1002/anie.202009871
- Mantina, M., Chamberlin, A. C., Valero, R., Cramer, C. J., and Truhlar, D. G. (2009). Consistent van der Waals Radii for the Whole Main Group. *The Journal of Physical Chemistry A*, 113(19), 5806–5812. doi: 10.1021/jp8111556

- Marques, R. T., Ferreira, L. P., Gomes, C. S. B., Lopes, C. S. D., Bernardes, C. E. S., Sarangi, N. K., Keyes, T. E., and Martinho, P. N. (2023). Reversible Single-Crystal-to-Single-Crystal Transformations in a salEen Fe(III) Spin Crossover Sponge. *Crystal Growth & Design*, 23(5), 3222–3229. doi: 10.1021/acs.cgd.2c01405
- Martinho, P. N., Vicente, A. I., Realista, S., Saraiva, M. S., Melato, A. I., Brandão, P., Ferreira, L. P., and De Deus Carvalho, M. (2014). Solution and solid state properties of Fe(III) complexes bearing N-ethyl-N-(2-aminoethyl)salicylaldiminate ligands. *Journal of Organometallic Chemistry*, 760, 48–54.
doi: <https://doi.org/10.1016/j.jorganchem.2013.12.028>
- McCusker, J. K., Rheingold, A. L., and Hendrickson, D. N. (1996). Variable-Temperature Studies of Laser-Initiated $^5T_2 \rightarrow ^1A_1$ Intersystem Crossing in Spin-Crossover Complexes: Empirical Correlations between Activation Parameters and Ligand Structure in a Series of Polypyridyl Ferrous Complexes. *Inorganic Chemistry*, 35(7), 2100–2112. doi: 10.1021/ic9507880
- Pauling, L. (1927). THE SIZES OF IONS AND THE STRUCTURE OF IONIC CRYSTALS. *Journal of the American Chemical Society*, 49(3), 765–790. doi: 10.1021/ja01402a019
- Petty, R. H., Dose, E. V., Tweedle, M. F., and Wilson, L. J. (1978). Bis(N-methylethylene diaminesalicylaldiminato)iron(III) complexes. Magnetic, Moessbauer, and intersystem crossing rate studies in the solid and solution states for a new ($S = 1/2$) .dblarw. ($S = 5/2$) spin-equilibrium case. *Inorganic Chemistry*, 17(4), 1064–1071. doi: 10.1021/ic50182a053
- Shongwe, M. S., Al-Zaabi, U. A., Al-Mjeni, F., Eribal, C. S., Sinn, E., Al-Omari, I. A., Hamdeh, H. H., Matoga, D., Adams, H., Morris, M. J., Rheingold, A. L., Bill, E., and Sellmyer, D. J. (2012). Accessibility and Selective Stabilization of the Principal Spin States of Iron by Pyridyl versus Phenolic Ketimines: Modulation of the $^6A_1 \leftrightarrow ^2T_2$ Ground-State Transformation of the $[FeN_4O_2]^+$ Chromophore. *Inorganic Chemistry*, 51(15), 8241–8253. doi: 10.1021/ic300732r
- Tweedle, M. F., and Wilson, L. J. (1976). Variable spin iron(III) chelates with hexadentate ligands derived from triethylenetetramine and various salicylaldehydes. Synthesis, characterization, and solution state studies of a new 2T .dblarw. 6A

spin equilibrium system. *Journal of the American Chemical Society*, 98(16), 4824–4834. doi: 10.1021/ja00432a023

Vicente, A. I., Joseph, A., Ferreira, L. P., de Deus Carvalho, M., Rodrigues, V. H. N., Duttine, M., Diogo, H. P., da Piedade, M. E., Calhorda, M. J., and Martinho, P. N. (2016). Dynamic spin interchange in a tridentate Fe(III) Schiff-base compound. *Chemical Science*, 7(7), 4251–4258. doi: 10.1039/C5SC04577K



CHAPTER V

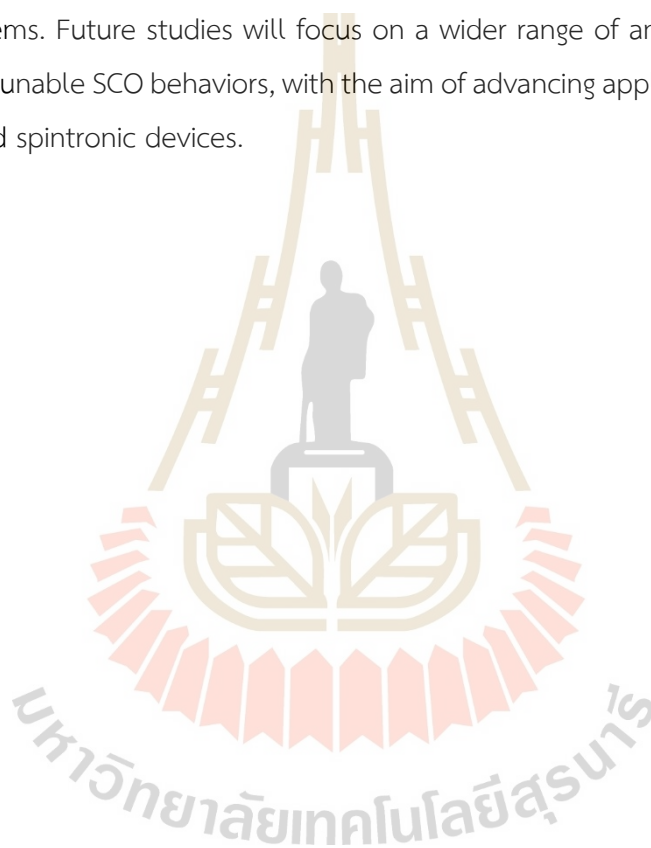
CONCLUSIONS

This thesis presents a comprehensive study of the $[\text{Fe}(\text{salBzen-5-OMe})_2]\text{A}$ where $\text{A} = \text{Cl}^-$ **1**, Br^- **2**, I^- **3**, NO_3^- **4**, and ClO_4^- **5** and $[\text{Fe}(\text{salPren-5-OMe})_2]\text{A}$ where $\text{A} = \text{Cl}^-$ **6**, Br^- **7**, I^- **8**, NO_3^- **9**, and ClO_4^- **10** complexes, focusing on the effects of the counterion (A) and the substituent group on a tridentate ligand platform (R). These complexes were successfully synthesized, and their magnetic properties thoroughly explored.

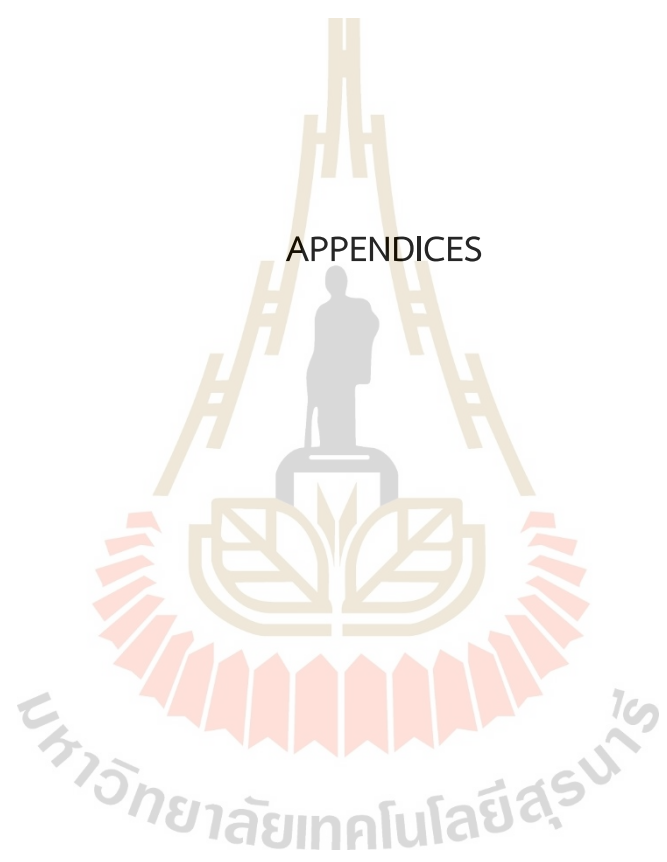
The UV-Vis spectra show two LMCT bands corresponding to the LS and HS states, supported by theoretical studies on related complexes. The crystal structures determined by X-Ray crystallography indicate that they crystallize in monoclinic $\text{P2}_1/\text{n}$ or $\text{P2}_1/\text{c}$ (**1**, **2**, **4** and **5**) or tetragonal P4_32_12 (**3**) phases. The X-ray crystal structures at room temperature reveal HS Fe(III) centers in **1**, **2** and **5**, and LS Fe(III) centers in **3** and **4**. Notably, complex **1** maintained its HS state across a wide temperature range, displaying a rare symmetry-breaking behavior unusual in Fe(III) systems. A 3D molecular network in these structures is stabilized by a variety of intermolecular interactions, including $\text{C-H}\cdots\pi$, $\text{C-H}\cdots\text{O}$, $\text{N-H}\cdots\text{O}$, $\text{C-H}\cdots\text{anion}$ and $\text{N-H}\cdots\text{anion}$. SQUID magnetometry revealed diverse SCO behaviors among the salBzen series. Complexes **1** and **2** remained in the HS state down to 10 K, while complex **5** underwent an abrupt, but incomplete SCO with a small hysteresis of 6 K, corresponding to 20% Fe switching. Complexes **3** and **4** displayed gradual SCO above 350 K, emphasizing the role of larger anions in stabilizing the LS state. For the salPren series, despite unsuccessful recrystallization attempts, magnetic studies demonstrated gradual and incomplete SCO behavior with temperature. These findings underline the critical influence of counterions and ligand substituents on spin-state stabilization in these Fe(III) complexes. The electrochemical studies of **1–5** and **6–10** highlight the impact of ligand structure and counteranions on redox behavior. The salBzen complexes show greater variation in redox potential due to stronger anion interactions within a rigid binding pocket, while the salPren complexes exhibit more consistent potentials, suggesting

increased anion mobility. Ligand oxidation potentials remain largely unaffected by the anion, though the salPren series display slightly higher oxidation potentials due to their stronger electron-donating nature. The narrower peak separations observed in salPren complexes indicate faster electron transfer compared to salBzen. These results demonstrate that ligand flexibility, anion size and hydrogen bonding capability all significantly influence the redox properties of Fe(III) Schiff base complexes.

This work contributes to the understanding of structure-function relationships in SCO systems. Future studies will focus on a wider range of anions to access more abrupt and tunable SCO behaviors, with the aim of advancing applications in molecular switches and spintronic devices.



APPENDICES



APPENDIX A

SUPPORTING INFORMATION

A.1 Mass spectrometry analysis data for $[\text{Fe}(\text{salRen-5-OMe})_2]\text{A}$ complexes

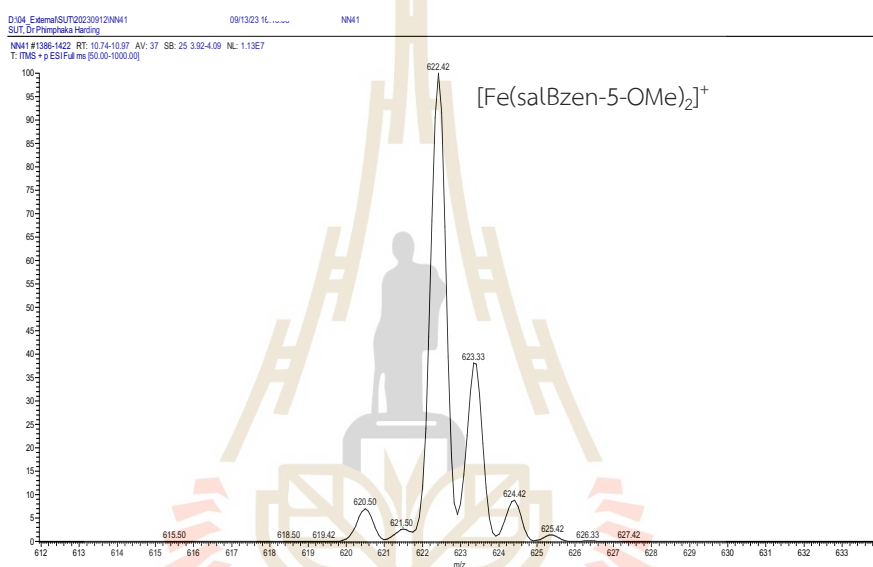


Figure S1. Mass spectra (LC-MS, positive) of 1.

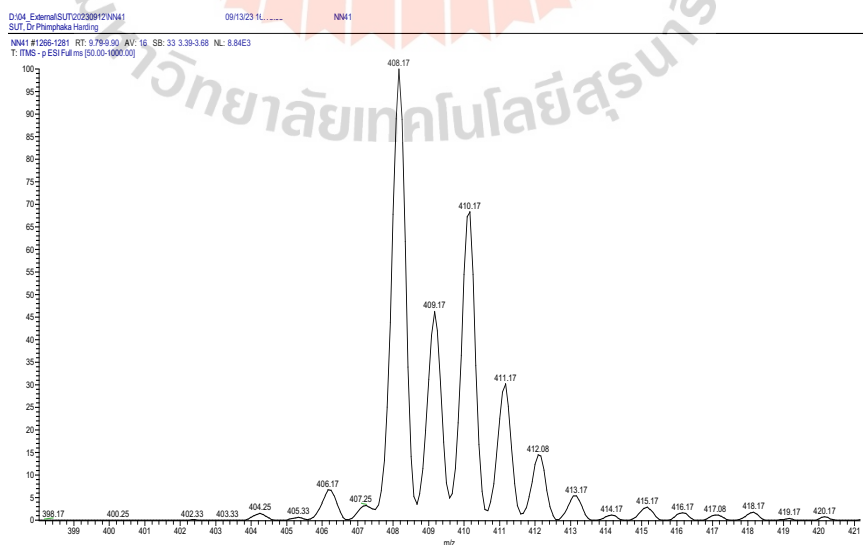


Figure S2. Mass spectra (LC-MS, negative) of 1.

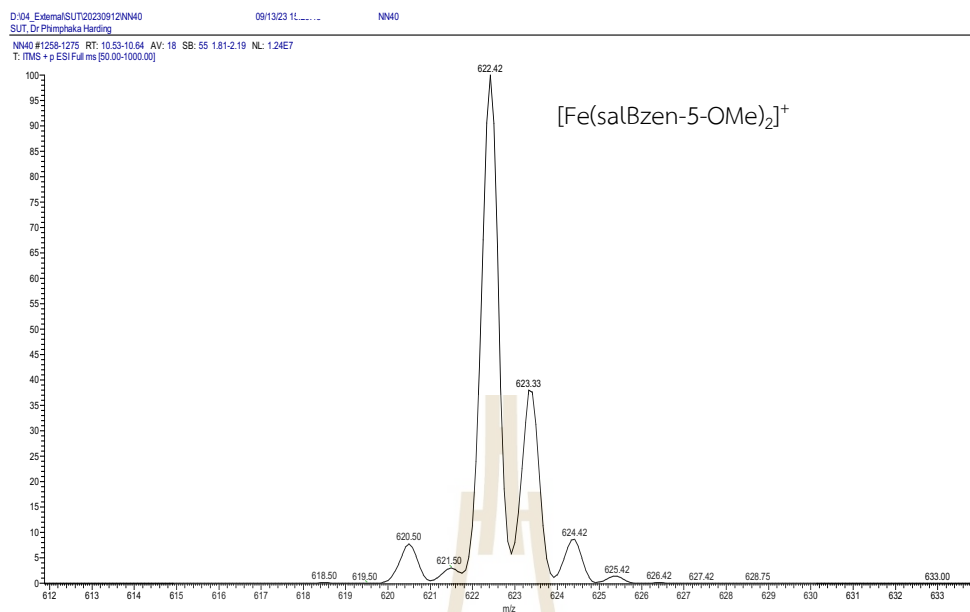


Figure S3. Mass spectra (LC-MS, positive) of 2.

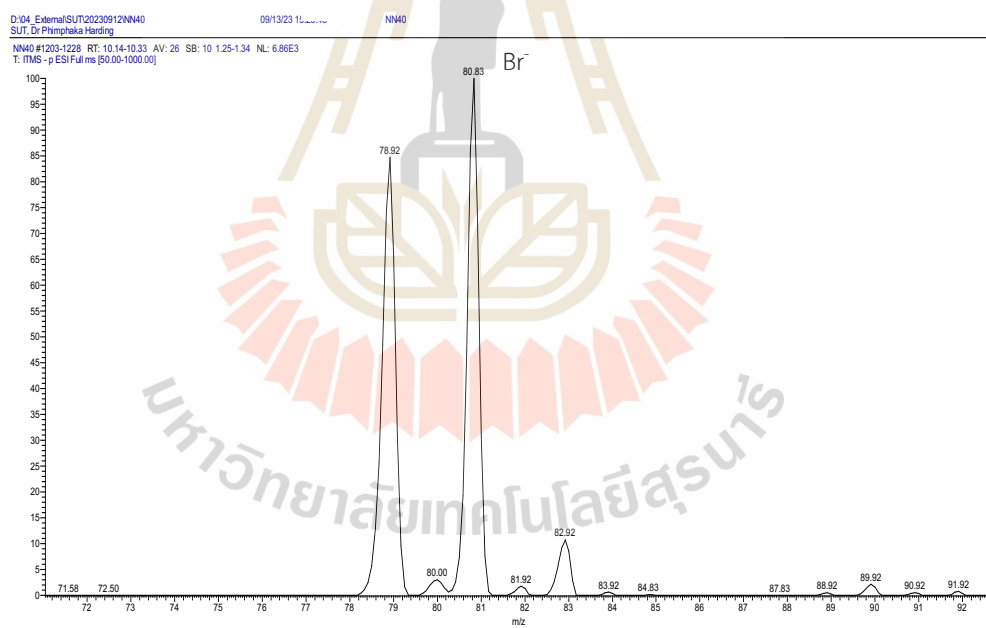


Figure S4. Mass spectra (LC-MS, negative) of 2.

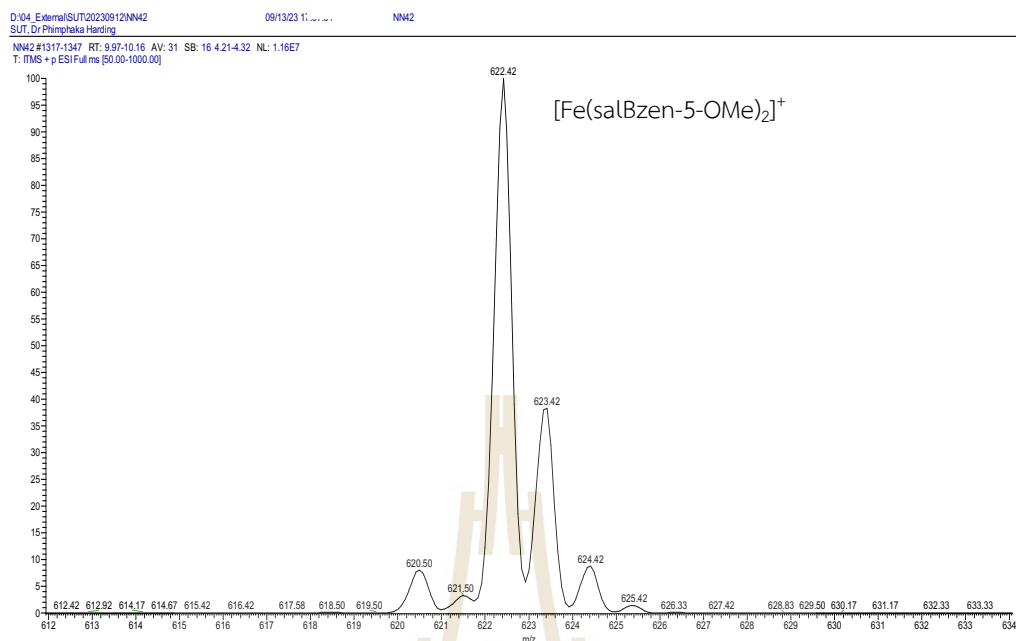


Figure S5. Mass spectra (LC-MS, positive) of 3.

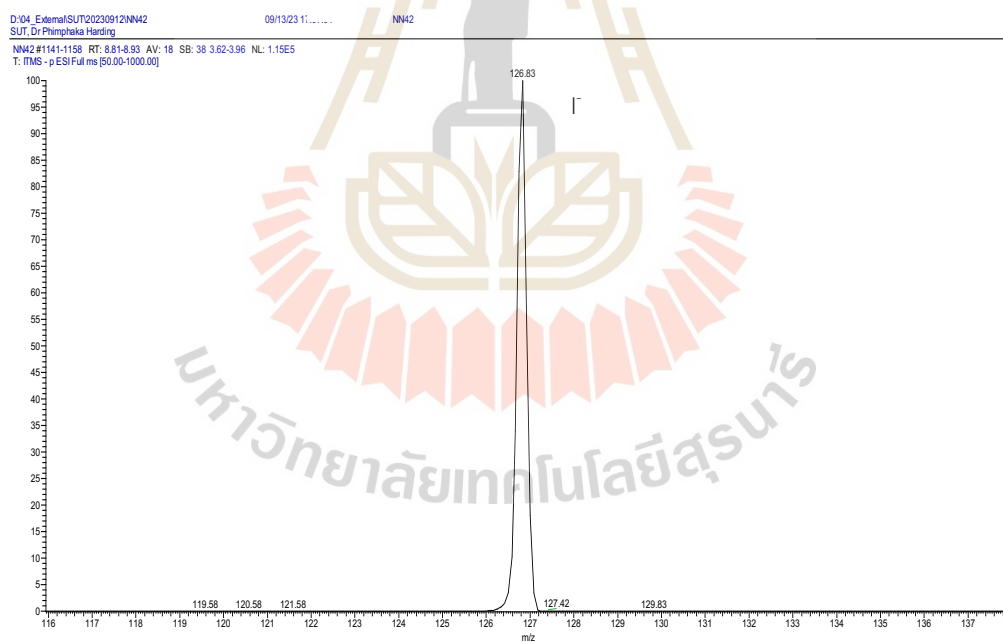


Figure S6. Mass spectra (LC-MS, negative) of 3.

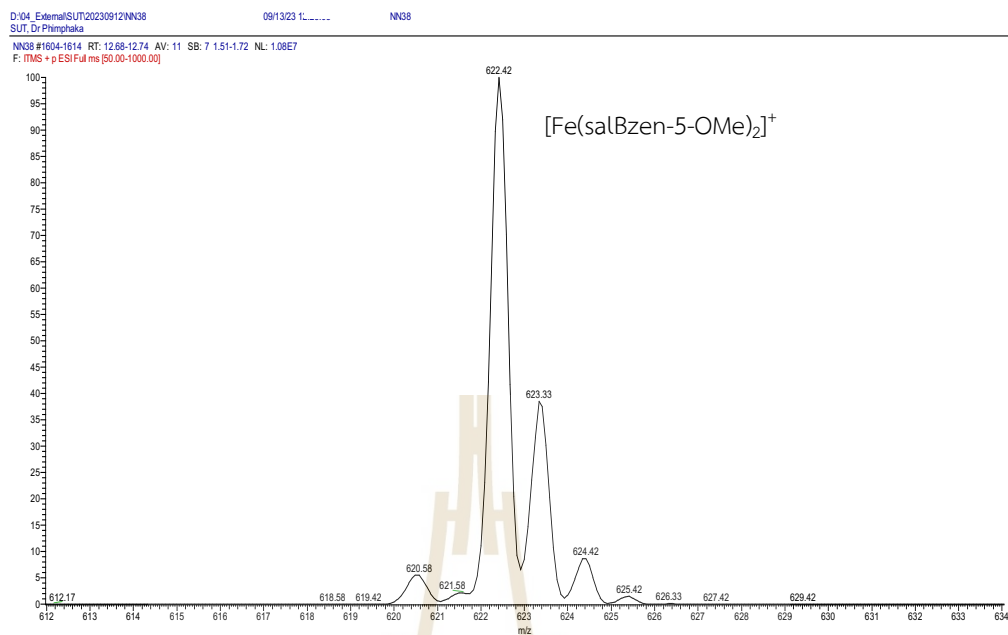


Figure S7. Mass spectra (LC-MS, positive) of 4.

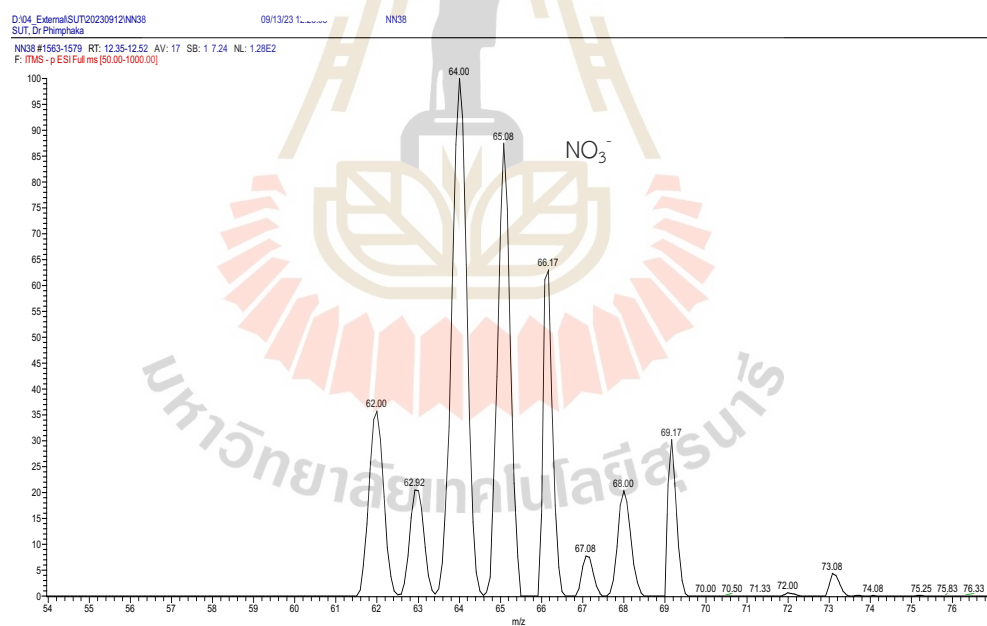


Figure S8. Mass spectra (LC-MS, negative) of 4.

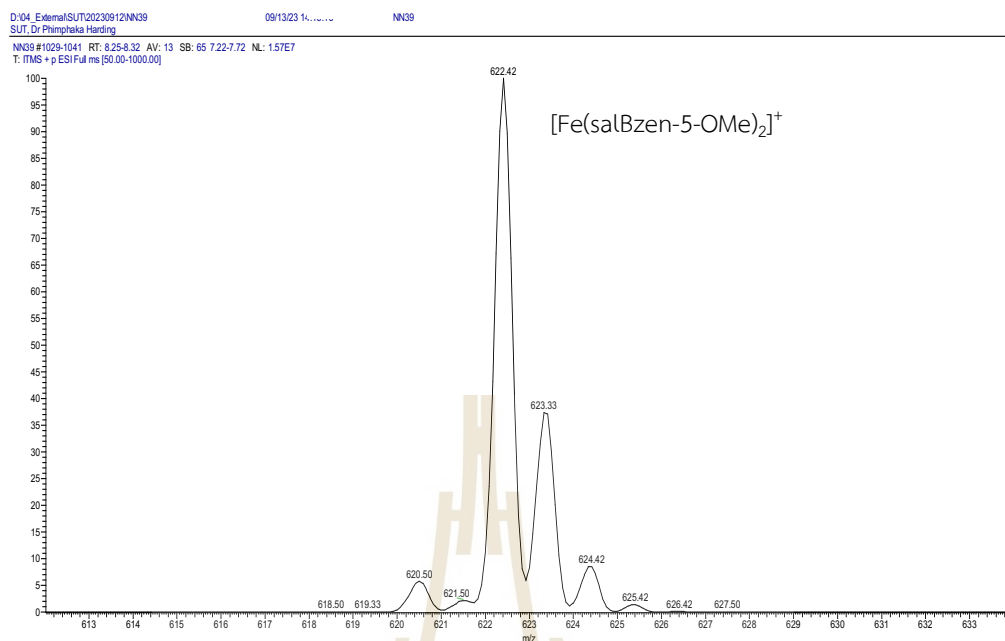


Figure S9. Mass spectra (LC-MS, positive) of 5.

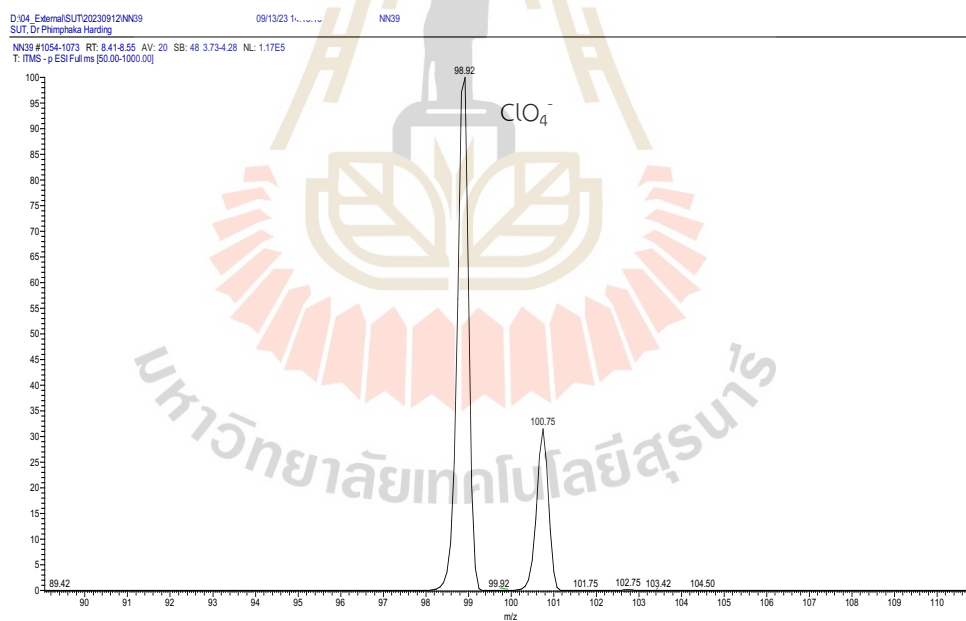
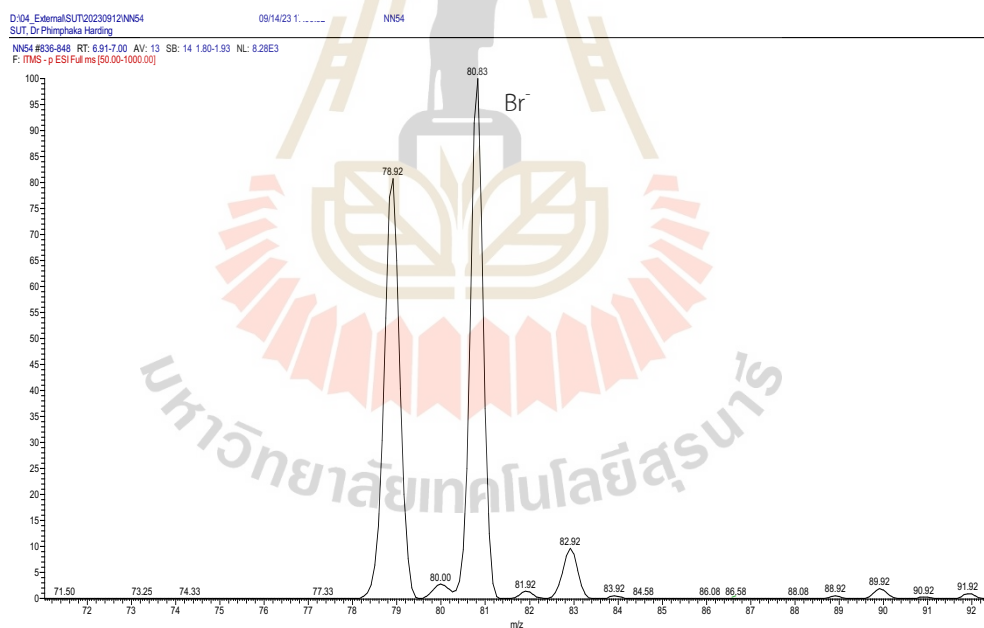
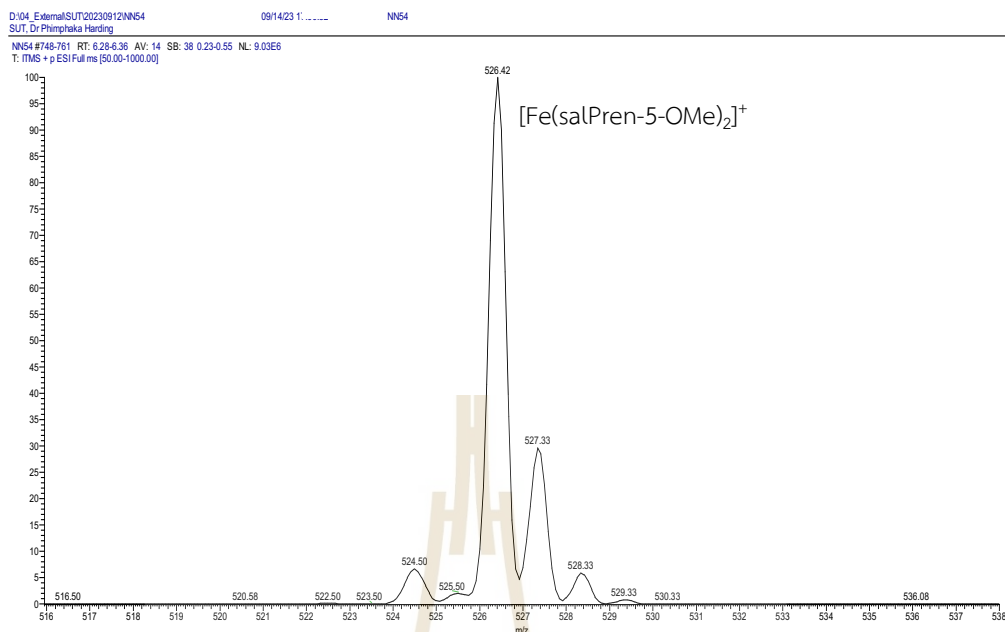


Figure S10. Mass spectra (LC-MS, negative) of 5.



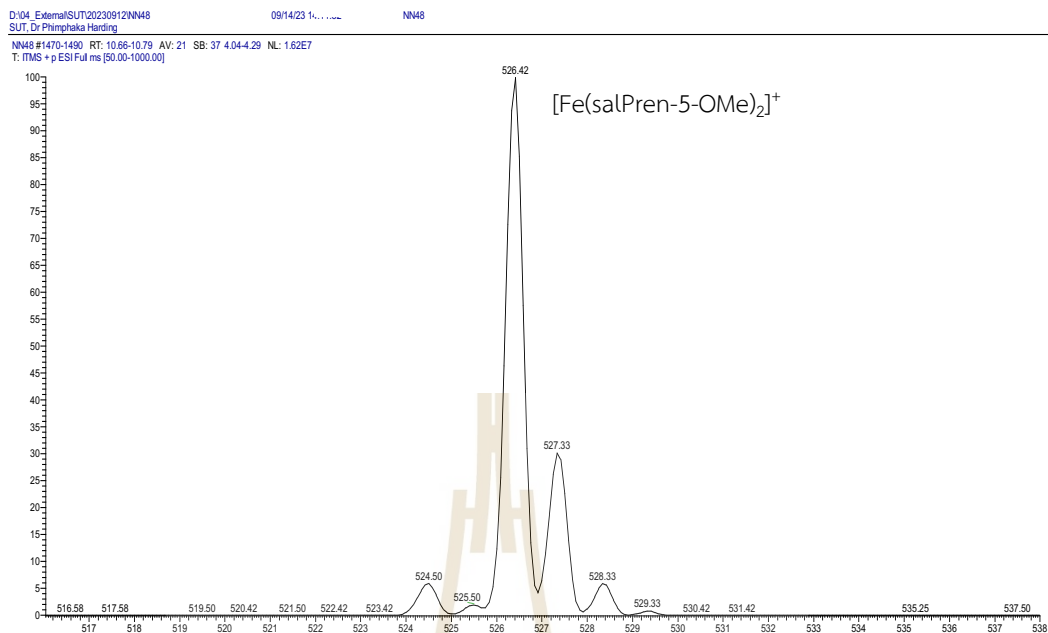


Figure S13. Mass spectra (LC-MS, positive) of 8.

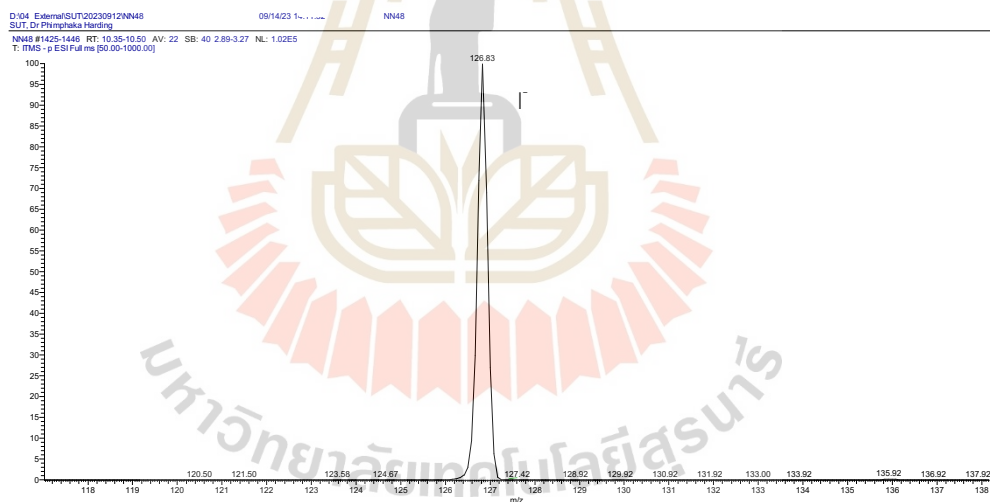


Figure S14. Mass spectra (LC-MS, negative) of 8.

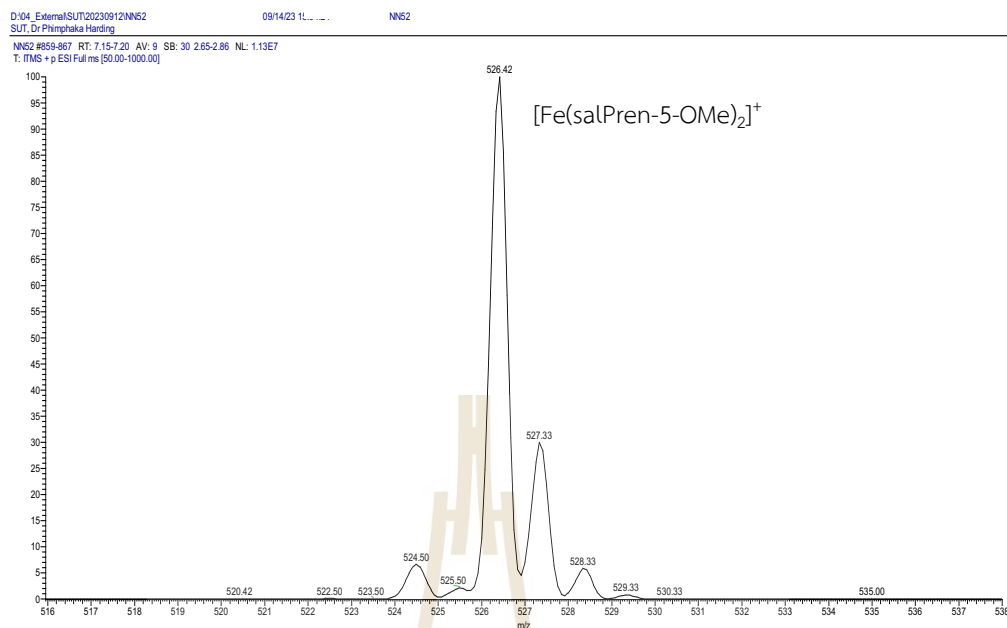


Figure S15. Mass spectra (LC-MS, positive) of 9.

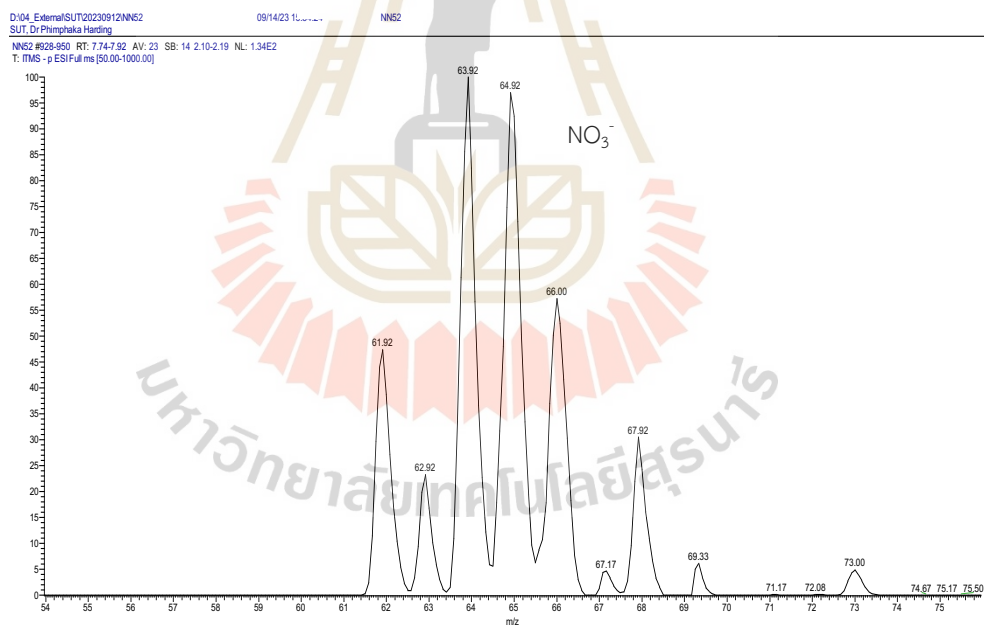
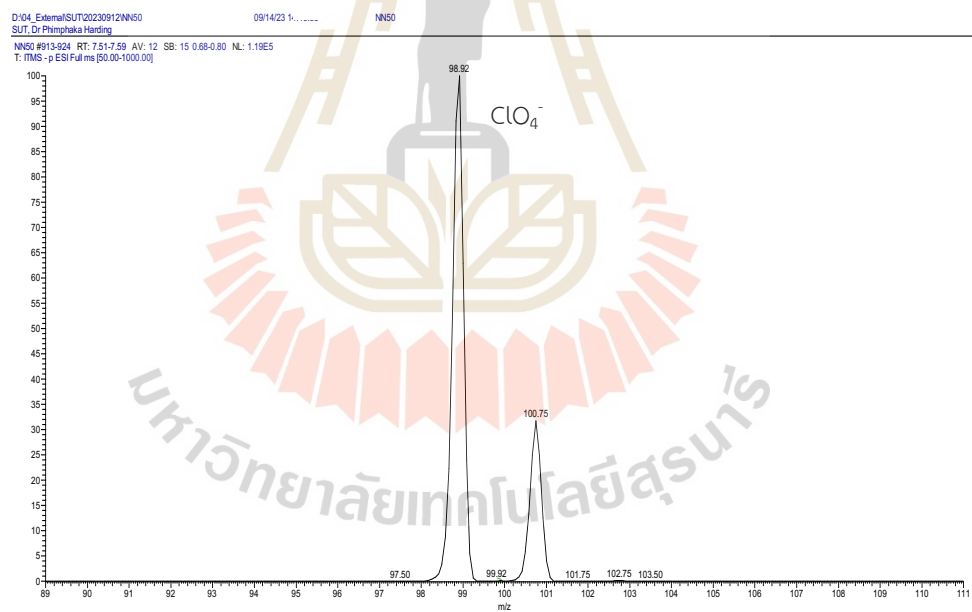
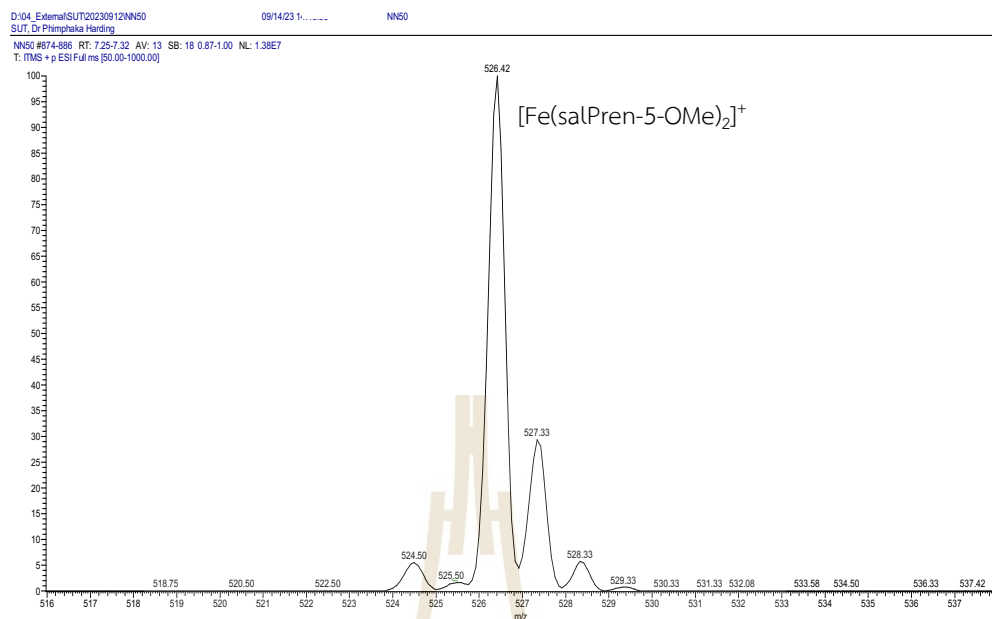


Figure S16. Mass spectra (LC-MS, negative) of 9.



A.2 PXRD pattern data for $[\text{Fe}(\text{salRen-5-OMe})_2]\text{A}$ complexes

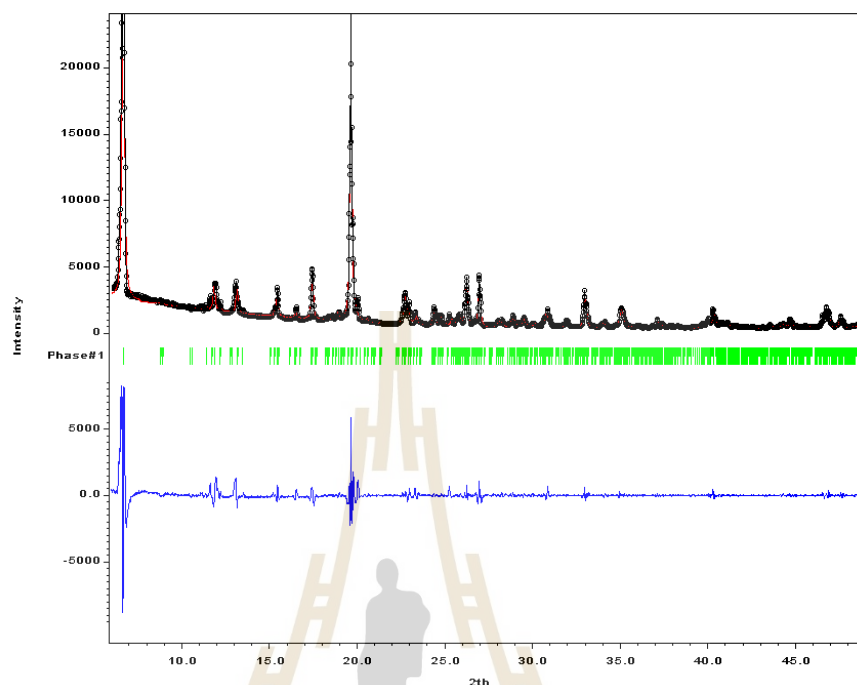


Figure S19. PXRD patterns of 1.

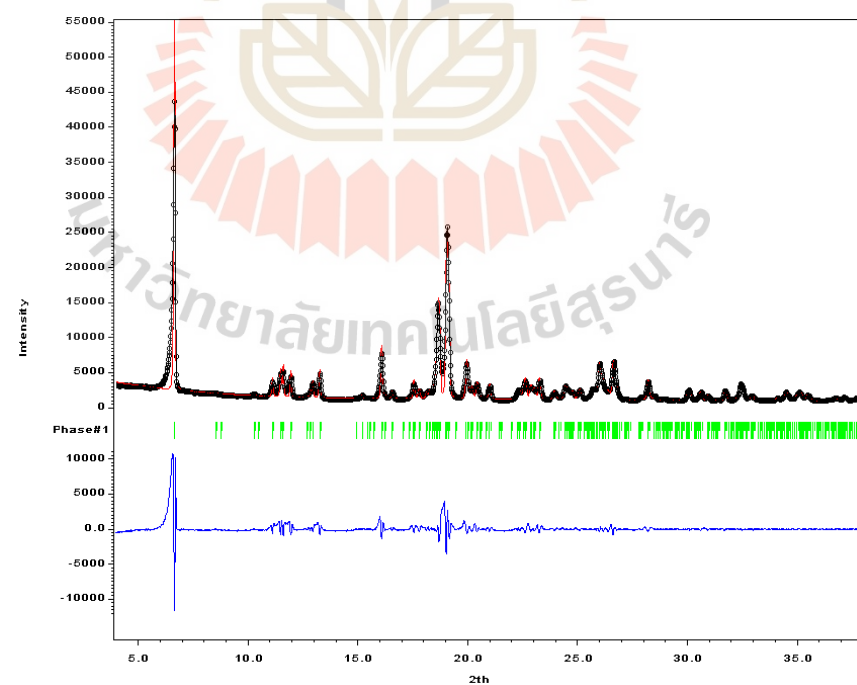


Figure S20. PXRD patterns of 2.

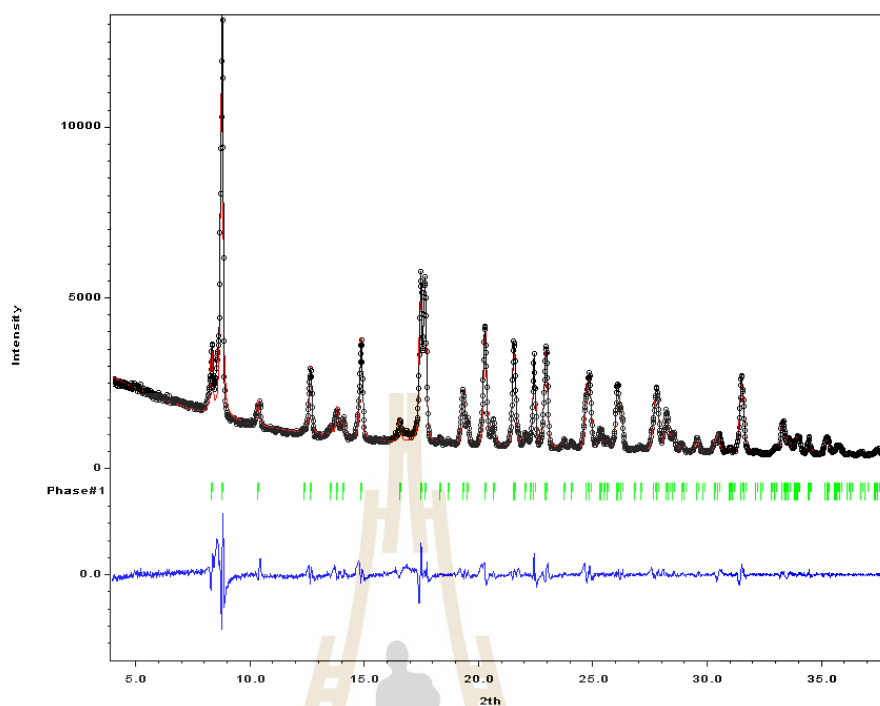


Figure S21. PXRD patterns of 3.

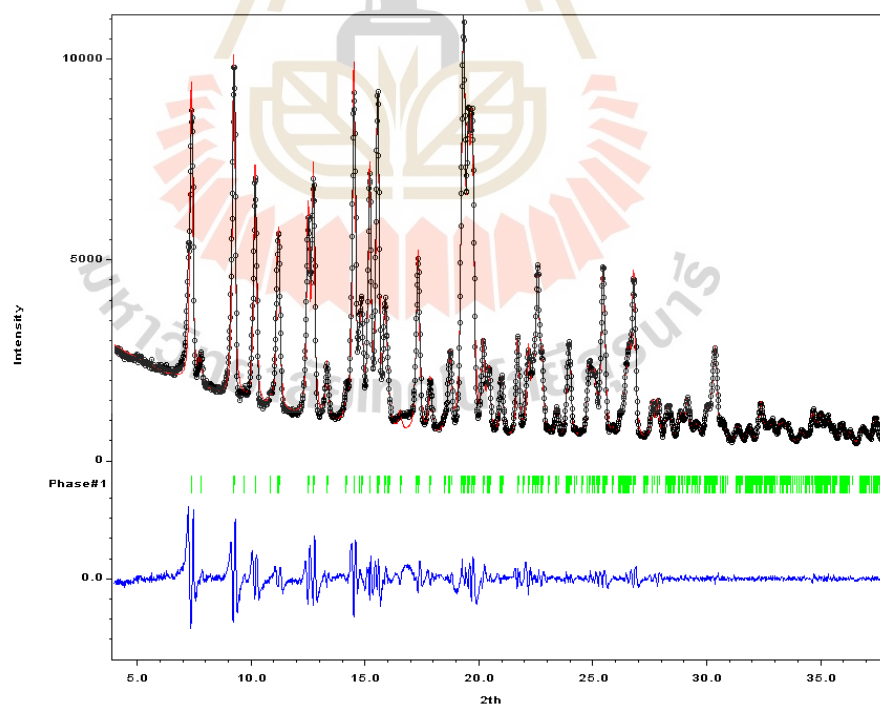


Figure S22. PXRD patterns of 4.

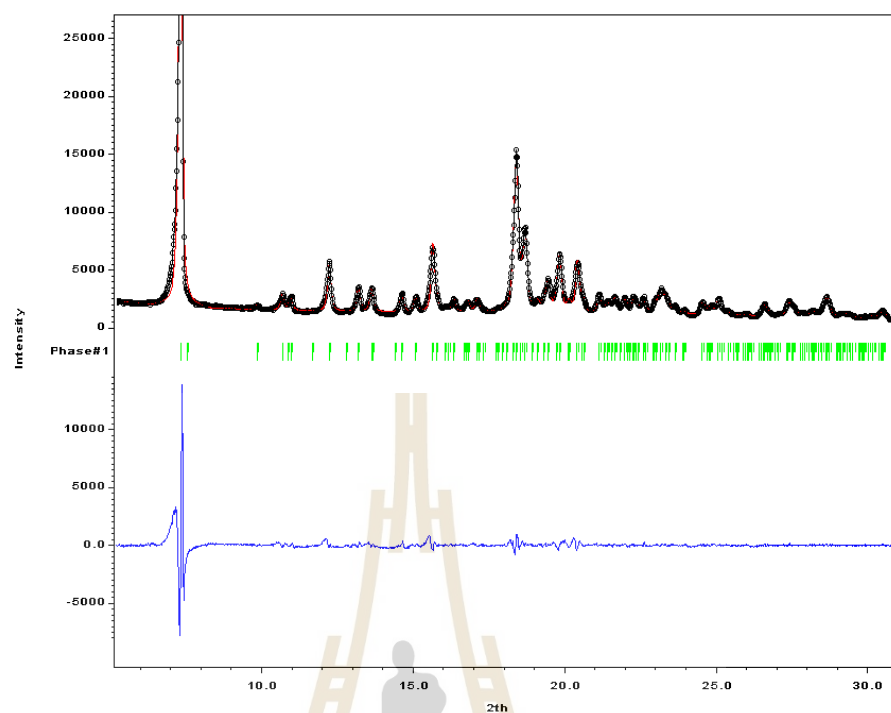


Figure S23. PXRD patterns of 5.

*Experimental PXRD diffractograms (black) and the corresponding simulated patterns (red) for each complex.

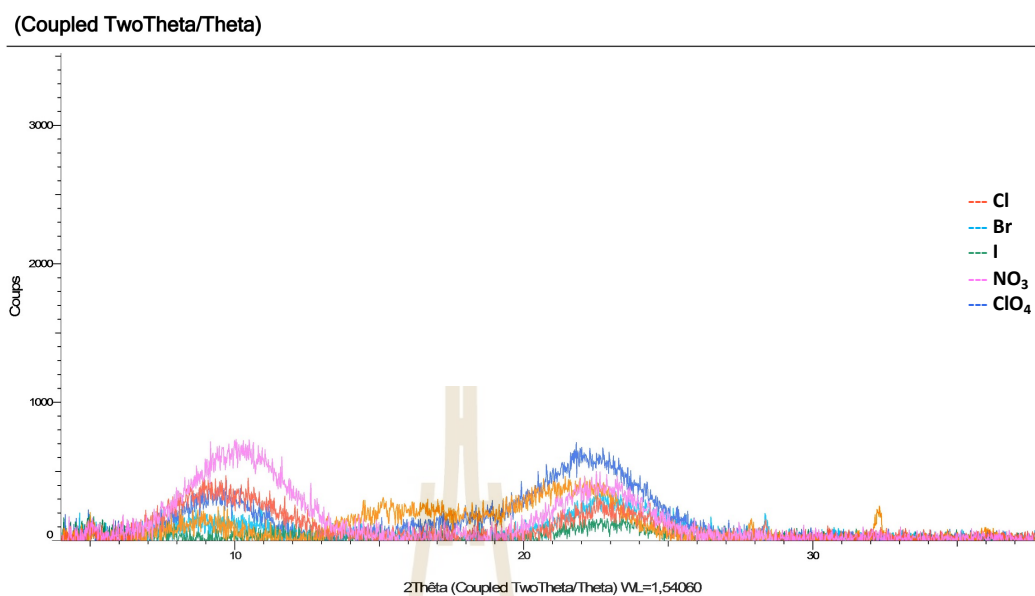


Figure S24. PXRD patterns of 6-10

*Experimental PXRD diffractograms of 6-10, on which all bulk measurements were done, are amorphous.

มหาวิทยาลัยเทคโนโลยีสุรนารี

A.3 Hirshfeld surface data analysis for $[\text{Fe}(\text{salBzen-5-OMe})_2]\text{A}$ complexes

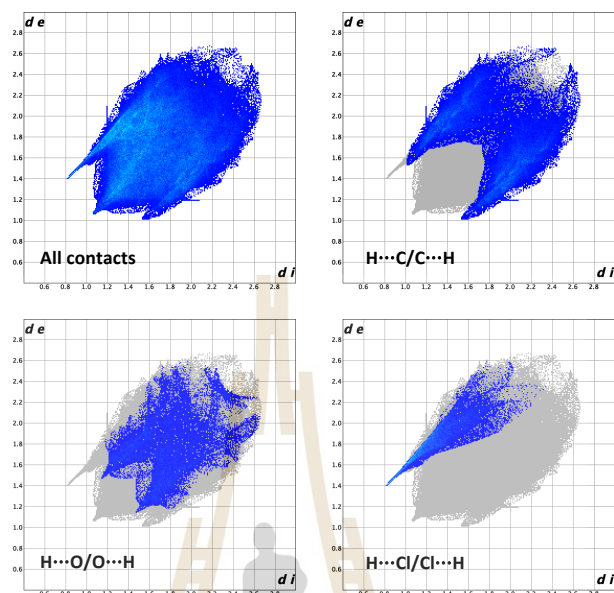


Figure S25. 2D fingerprint plots of all contacts: $\text{H}\cdots\text{C}$, $\text{H}\cdots\text{O}$ and $\text{H}\cdots\text{Cl}$ for **1** at 150 K.

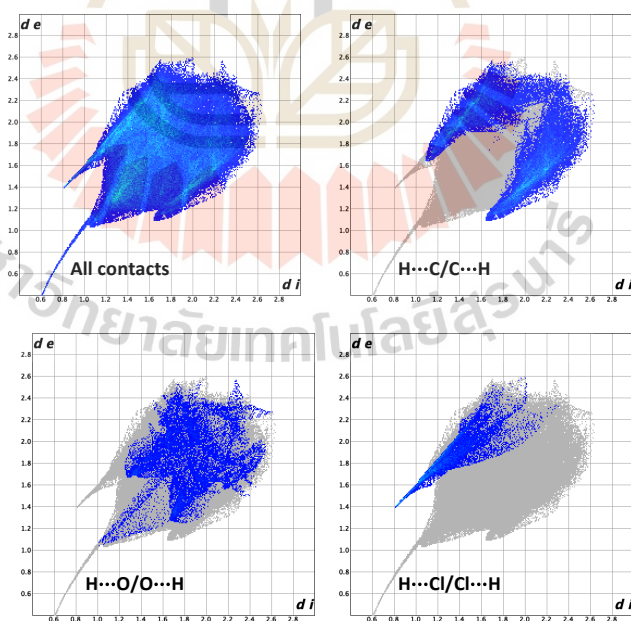


Figure S26. 2D fingerprint plots of all contacts: $\text{H}\cdots\text{C}$, $\text{H}\cdots\text{O}$ and $\text{H}\cdots\text{Cl}$ for **1** at 295 K.

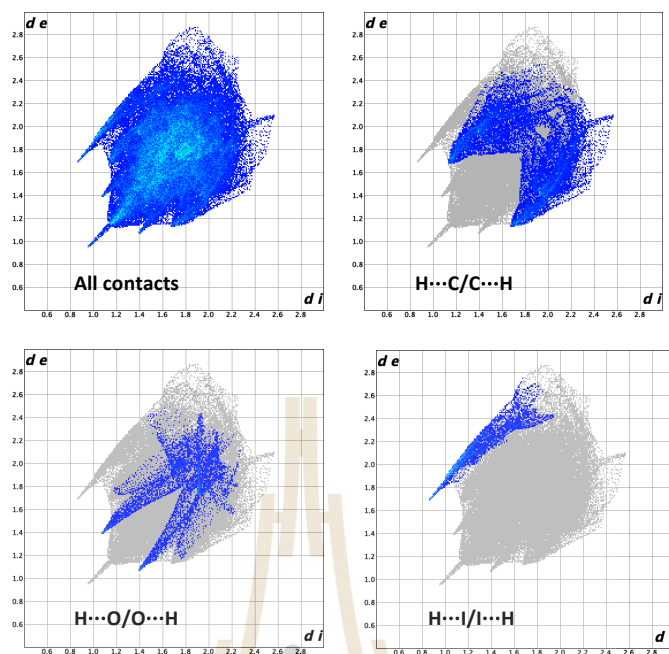


Figure S27. 2D fingerprint plots of all contacts: $H\cdots C$, $H\cdots O$ and $H\cdots I$ for **3** at 150 K.

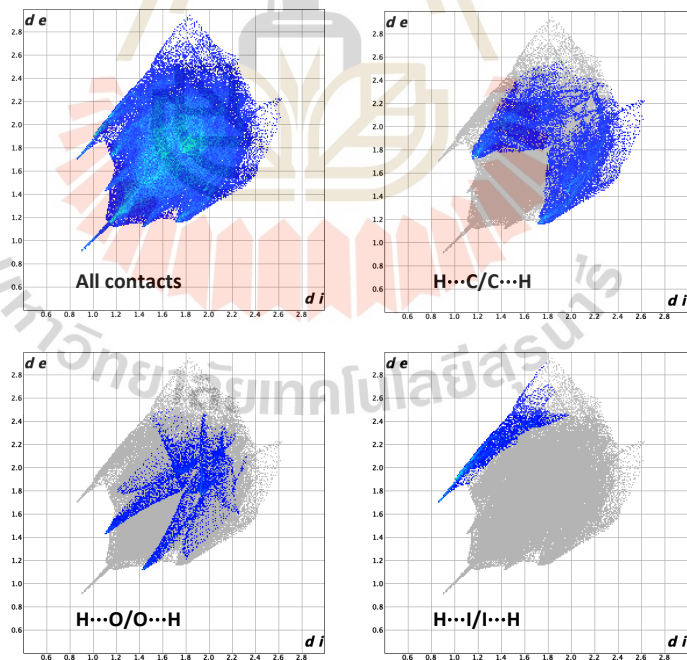


Figure S28. 2D fingerprint plots of all contacts: $H\cdots C$, $H\cdots O$ and $H\cdots I$ for **3** at 295 K.

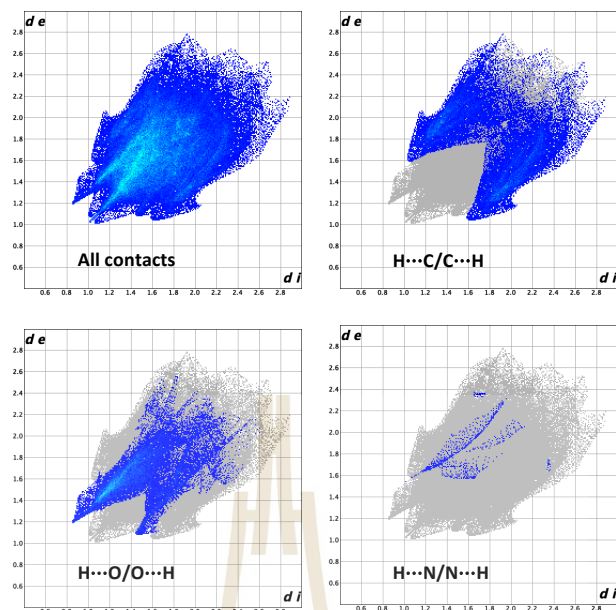


Figure S29. 2D fingerprint plots of all contacts: H...C, H...O and H...N for **4** at 150 K.

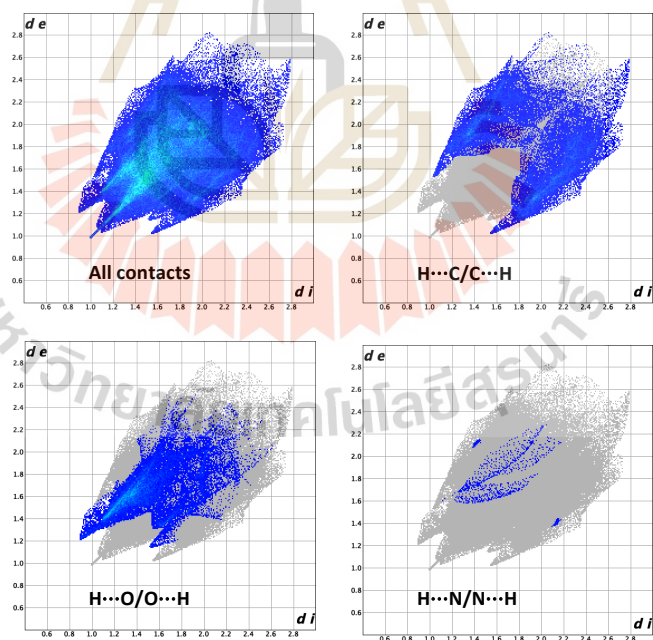


Figure S30. 2D fingerprint plots of all contacts: H...C, H...O and H...N for **4** at 295 K.

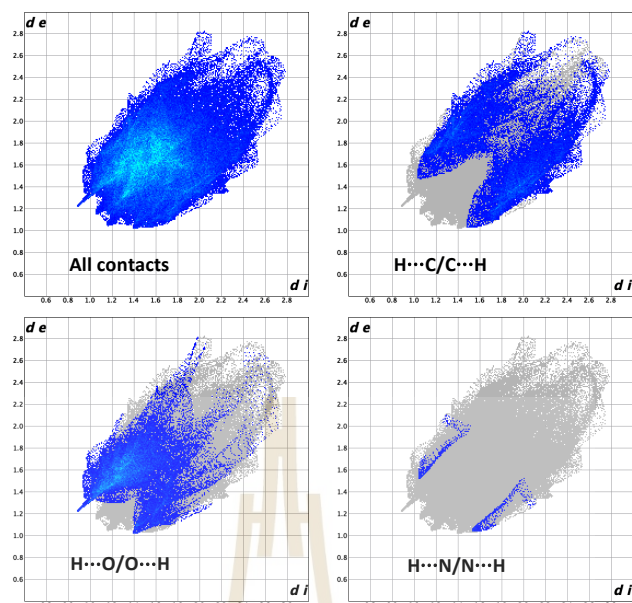


Figure S31. 2D fingerprint plots of all contacts: H...C, H...O and H...N for **5** at 30 K.

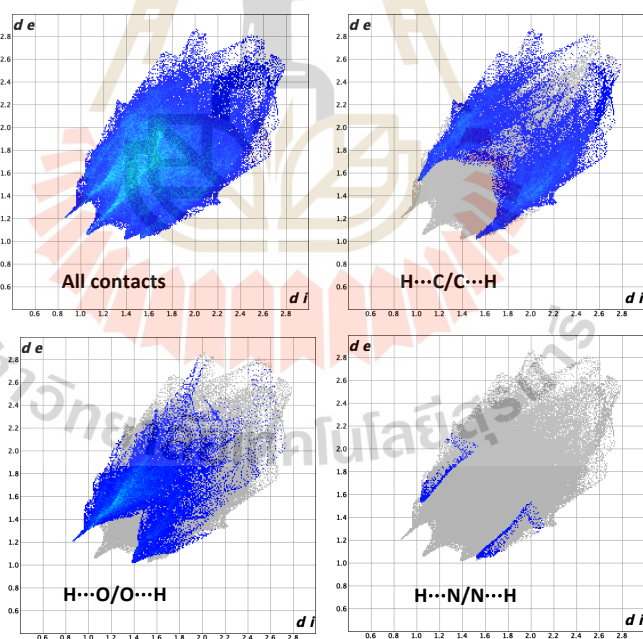


Figure S32. 2D fingerprint plots of all contacts: H...C, H...O and H...N for **5** at 100 K.

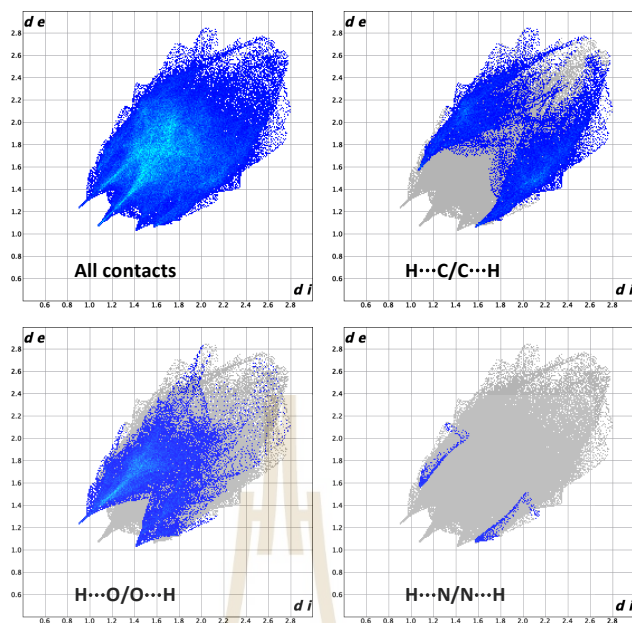


Figure S33. 2D fingerprint plots of all contacts: H...C, H...O and H...N for **5** at 295 K.



APPENDIX B

PUBLICATION AND PRESENTATIONS

B.1 List of publications

Natputree, N., Duverger-Nédellec, Songkerdthong, J., E., Chastanet, G., Harding, P., and Harding, D. J. (2025). Decoupling of symmetry breaking and spin crossover in iron(III) complexes bearing an N-benzylethylenediamine ligand. *Crystal Growth & Design*. 25, 1528-7483. doi: 10.1021/acs.cgd.5c00493

B.2 List of presentations

Natputree, N., Duverger-Nédellec, E., Chastanet, G., Harding, P., and Harding, D. (2024). Magnetic and Structural Studies $[\text{Fe}(\text{salBzen-5-OMe})]_2\text{Y}$ Complexes. **8th Bordeaux Olivier Kahn Discussions: Magnetism & Light**. 14-16 May 2024, Institute of Condensed Matter Chemistry of Bordeaux (ICMCB), Bordeaux, France. (Poster presentation)

Natputree, N., Duverger-Nédellec, E., Chastanet, G., Harding, P., and Harding, D. (2024). Magnetic and Structural Studies $[\text{Fe}(\text{salBzen-5-OMe})]_2\text{A}$ Complexes. **The Royal Australian Chemical Institute (RACI) Inorganic Division Meeting IC'24**. 8-12 December 2024, The Parramatta City Campus of Western Sydney University (WSU), New South Wales, Australia. (Oral presentation)

Natputree, N., Duverger-Nédellec, E., Chastanet, G., Harding, P., and Harding, D. (2025). Magnetic and Structural Studies $[\text{Fe}(\text{salBzen-5-OMe})]_2\text{A}$ Complexes. **The Pure and Applied Chemistry International Conference 2025**. 13-15 February 2025, Khao Yai Convention Center (KYCC) Greenery Resort Khao Yai, Nakhon Ratchasima, Thailand. (Oral presentation)

CURRICULUM VITAE

NADIA NATPUTREE

AWARDS

- **2018-present:** Full financial support through a Development and Promotion of Science and Technology Talents Project (DPST) scholarship to study for my bachelors and master's in chemistry.
- Best oral presentation at the 48th International Congress on Science, Technology and Technology-based Innovation (STT48): Inorganic session.

PROFESSIONAL RESEARCH EXPERIENCE

Molecular Magnetic Materials (M³) LAB, Master Research Project

Master of Science (Chemistry), Suranaree University of Technology, 2022-2024

Supervisor: Associate Professor Dr. David J. Harding

Associate Professor Dr. Phimpaka Harding

- Investigating the structural and magnetic properties of iron(III) spin crossover complexes.
- Proficient in the synthesis and magnetic studies in solution of iron(III) spin crossover complexes.
- Proficient and enhanced skills in recrystallization techniques.
- Proficient in using and analyzing data from a SQUID magnetometer.
- Proficient in using and analysing data from SCXRD diffractometer.
- Proficient in using and analyzing data from PXRD diffractometers and the Jana 2020 program.